

Dissertation presented to the Instituto Tecnológico de Aeronáutica, in partial fulfillment of the requirements for the degree of Master of Science in the Graduate Program of Physics, Field of Nuclear Physics.

Luiz Gustavo Mendonça Tenório

TWO-BODY CORRELATIONS IN VAN DER WAALS HETEROSTRUCTURES

Dissertation approved in its final version by signatories below:

Documento assinado digitalmente
 **TOBIAS FREDERICO**
Data: 15/08/2023 14:51:31-0300
Verifique em <https://validar.iti.gov.br>

Prof. Tobias Frederico

Advisor

Documento assinado digitalmente
 **TELDO ANDERSON DA SILVA PEREIRA**
Data: 15/08/2023 14:42:08-0300
Verifique em <https://validar.iti.gov.br>

Prof. Teldo Anderson da Silva Pereira

Co-advisor

Profa. Emília Villani

Pro-Rector of Graduate Courses

Campo Montenegro
São José dos Campos, SP - Brazil
2023

Cataloging-in Publication Data
Documentation and Information Division

Mendonça Tenório, Luiz Gustavo

Two-Body Correlations in Van der Waals Heterostructures / Luiz Gustavo Mendonça Tenório.
São José dos Campos, 2023.
92f.

Dissertation of Master of Science – Course of Physics. Area of Nuclear Physics – Instituto Tecnológico de Aeronáutica, 2023. Advisor: Prof. Tobias Frederico. Co-advisor: Prof. Teldo Anderson da Silva Pereira.

1. Problema de poucos corpos. 2. Heteroestruturas de van der Waals. 3. Estruturas bidimensionais. 4. Física de partículas. 5. Baixa temperatura. 6. Física nuclear. 7. Física. I. Instituto Tecnológico de Aeronáutica. II. Title.

BIBLIOGRAPHIC REFERENCE

MENDONÇA TENÓRIO, Luiz Gustavo. **Two-Body Correlations in Van der Waals Heterostructures**. 2023. 92f. Dissertation of Master of Science – Instituto Tecnológico de Aeronáutica, São José dos Campos.

CESSION OF RIGHTS

AUTHOR'S NAME: Luiz Gustavo Mendonça Tenório

PUBLICATION TITLE: Two-Body Correlations in Van der Waals Heterostructures.

PUBLICATION KIND/YEAR: Dissertation / 2023

It is granted to Instituto Tecnológico de Aeronáutica permission to reproduce copies of this dissertation and to only loan or to sell copies for academic and scientific purposes. The author reserves other publication rights and no part of this dissertation can be reproduced without the authorization of the author.

Luiz Gustavo Mendonça Tenório
Zona Rural, Morrinho, Chácara Cuitelinho
78180-000 – Santo Antônio do Leverger–MT

TWO-BODY CORRELATIONS IN VAN DER WAALS HETEROSTRUCTURES

Luiz Gustavo Mendonça Tenório

Thesis Committee Composition:

Profa.	Lara Kühl Teles	President	-	ITA
Prof.	Tobias Frederico	Advisor	-	ITA
Prof.	Teldo Anderson da Silva Pereira	Co-advisor	-	UFMT
Prof.	André Jorge Carvalho Chaves	Internal Member	-	ITA
Dr.	Robson Ferreira	External Member	-	(CNRS/FRANÇA)

I dedicate this work to the memory of
my grandparents, Olíria and Geraldo.

Acknowledgments

First, I would like to thank my family, who supported me throughout the development of this work. In second, I thank my fiancée, Maria Julia, for the unending love and support which shaped these last few years into a pure state of joy and happiness. I Also, would like to acknowledge the support and help of my advisor, Prof. Tobias Frederico, which was a well of knowledge and towering scientific mind, my co-advisor and also friend, Prof. Teldo, our group of few-body systems in two-dimensions, composed of Prof. André, Prof. Diego, Prof. Hadizadeh, Kamyar and Fazaneh, for the ever presence of our monday meetings where I consistently learn a ton of physics. In particular, Prof. André for the opportunity, the constant support in each endeavor and encouraging words.

In closing, I thank all my friends, in particular, the Coup Group from UFMT, composed by Higor, Wendel, Victor Gustavo, Victor Manuel, Ximba, Piupiu and Douradinho, and also my partners in crime from ITA's PG-FIS, Gusthavo (which also helped me a lot with the DFT calculations), Victor, Denys and Isabella.

*"If I have seen farther than others,
it is because I stood on the shoulders of giants."*

— SIR ISAAC NEWTON

Resumo

O paradigma central da teoria de muitos-corpos é que as simetrias e interações do sistema levam ao surgimento de comportamento únicos. Do outro lado do espectro da física teórica, temos a física de poucos-corpos onde o número de partículas interagentes é pequeno e a universalidade se encontra na independência de maiores detalhes das interações do sistema. Tais caminhos, aparentemente distantes, se cruzam no contexto de gases ultrafrios e, mais recentemente, no contexto da matéria condensada. Neste contexto, a formação de estruturas compostas por elétrons e buracos gera sistemas propícios para o uso de técnicas da física de poucos corpos, ainda mais com o surgimento de materiais bidimensionais e no estudo de como as propriedades físicas desses materiais são maleáveis por modificações no ambiente dielétrico e geométrico. Neste trabalho vamos estudar a física de uma dessas estruturas compostas, o éxciton, no contexto de hetero e homoestruturas de Van der Waals bidimensionais. Ainda, vamos discutir sobre o surgimento de isolantes excitônicos devido ao alinhamento de bandas e éxcitons intercamadas fortemente ligados em materiais bidimensionais. Finalmente, vamos discutir a física do éxciton no fósforo negro, que possui uma relação de dispersão anisotrópica.

Abstract

A central paradigm of the many-body theory is that the underlying symmetries alongside the interactions that governs the many-particle system gives rise to emerging unique behavior. On the other side of the physical theory coverage, we have the few-body physics, where the number of interacting particles is low and universality lies in the independence of the very details regarding interactions. These two seemingly distant paths have already crossed in the context of ultracold gases and, more recently, also in condensed matter theory. In the case of condensed matter, the formation of composite structures by electrons and holes yields an interesting background to apply few-body techniques, even more so with the discovery of two dimensional materials and how their physical properties are tunable by environmental and geometric modifications. In this work we aim to study the physics of one composite structure, the exciton, in the context of 2D Van der Waals hetero and homostructures. Also, we will discuss about the rise of the excitonic insulators due to band alignment and strongly bound interlayer excitons in bilayer materials. Finally, we will discuss the excitonic physics of the Black Phosphorous, which has an anisotropic dispersion relation.

List of Figures

FIGURE 1.1 – (Color Online) Geometry and band structure of MoSe ₂ . In (a) and (b) the top and side views of the molecular geometry is presented. In (c) we show the band structure of MoSe ₂ . The band structure was calculated using density functional theory (HOHENBERG; KOHN, 1964; KOHN; SHAM, 1965).	20
FIGURE 1.2 – (Color Online) Geometry and band structure of a black phosphorous monolayer. In (a), (b) and (c) the molecular geometry of the system is presented. In (d) we present the band structure of the monolayer black phosphorous. The band structure was calculated using density functional theory (HOHENBERG; KOHN, 1964; KOHN; SHAM, 1965).	21
FIGURE 1.3 – (Color Online) Physical picture of the exciton formation. In (a) we show the ladder diagram responsible for the exciton pair. In (b) we present a schematic view of the exciton pair in a two-band system. The red and blue balls represents the electron and hole, respectively and the connecting shade is the electron-hole bound state, the exciton.	23
FIGURE 1.4 – (Color online) Schematic diagram of the electrostatic problem.	24

- FIGURE 1.5 – (Color online) (a) Comparison between different carrier-carrier potentials in momentum space: RK (solid blue curve), Coulomb (dashed green curve with rhombus symbols), intralayer (dashed orange curve with circular symbols), and interlayer (dashed red curve) interactions. The interlayer [Eq. (1.21)] and the intralayer [Eq. (1.22)] potentials were calculated considering $r_1 = r_2 = r = 44.68 \text{ \AA}$ and $d = 7.15 \text{ \AA}$. When q is of the order of $1/r$, the Coulomb potential deviates from the other three and a negligible difference between the intralayer and the RK potentials is observed. The interlayer potential shows a strong screening that is due to the term proportional to e^{-qd} of $G_j(q)$ in Eq. (1.19) when $q \approx 1/d$. (b) The relative difference between the intralayer and the RK potentials, which can be as high as 15% the shorter the spacer width d 27
- FIGURE 2.1 – (Color online) Illustration of band structure around the K point and SOC induced band splitting. We see a crossing between spin bands for the WSe_2 and no crossing for MoSe_2 30
- FIGURE 3.1 – (Color online) Graphical convergence table for the Chebyhev-Chawla-Kumar method using the Rytova-Keldysh potential (1.24). 49
- FIGURE 3.2 – (Color online) Comparison between the Gauss-Legendre quadrature method (with 1000 radial mesh points and 61 angular mesh points) and the Chebyshev method ($N = M = 600$ and $N_\theta = 320$) for different states of the MoS_2 exciton using the RK potential. $\psi_i(p)$ is the i -th excited state for the S -wave. 52
- FIGURE 4.1 – (Color online) (a) Schematic illustration of the double layered TMDs, separated by a spacer of dielectric constant ϵ_2 ($-d \leq z \leq 0$) and width d , immersed in two materials of dielectric constants ϵ_1 ($z > 0$) and ϵ_3 ($z < -d$). This structure sustains both intralayer and interlayer excitons. (b) Band alignment as measured from the vacuum between the four TMDs considered in this work. The bandgap energies and their alignments were obtained from DFT calculations in Ref. (ZHANG *et al.*, 2016). 58

- FIGURE 4.2 – (Color online) Schematic illustration of the lowest conduction (CB) and valence (VB) bands of monolayer TMDs in the vicinity of the K (red curves) and K' (blue curves) points, emphasizing the band splitting due to SOC and spin flipping for each band in the opposite valley due to the inversion symmetry. The up (red) and down (blue) arrows stand for spin-up and spin-down states. SOC_{CB} (SOC_{VB}) corresponds to the energetic split of the conduction (valence) band. 59
- FIGURE 4.3 – (Color online) $K-K$ transition energies of both spins for MoS_2 at the $\text{MoS}_2/\text{MoSe}_2$ heterostructure with respect to the changes (a) in the interlayer separation d in a suspended sample with $\epsilon_1 = \epsilon_2 = \epsilon_3 = 1$, and (b) in the spacer dielectric constant ϵ_2 with a fixed interlayer distance $d = 7.15 \text{ \AA}$ and external dielectric constants $\epsilon_1 = \epsilon_3 = 1$. Cyan and red curves correspond to up ($\Delta_{\uparrow,\tau}^{\text{MoS}_2}$) and down ($\Delta_{\downarrow,\tau}^{\text{MoS}_2}$) spin results, respectively. The solid lines in (a) represent a monolayer limit ($d \rightarrow \infty$) of the MoS_2 61
- FIGURE 4.4 – (Color online) Binding energies (E_B) of the intralayer A excitons, referred to as an electron-hole pair lying in the MoS_2 layer, by taking different layer compounds in the TMD heterostructure formation. Red solid, green dashed, and blue dotted curves correspond to $\text{MoS}_2 - \text{MoSe}_2$, $\text{MoS}_2 - \text{WSe}_2$, and $\text{MoS}_2 - \text{WS}_2$ double-layers, respectively. Panels (a) and (b) show the dependence of E_B on the separation distance of the layers d , by assuming $\epsilon_1 = \epsilon_2 = \epsilon_m = 1$, and on the dielectric constant ϵ_m , by assuming a fixed interlayer distance of $d = 41 \text{ \AA}$ and dielectric constants of the substrate and superstrate as $\epsilon_1 = \epsilon_2 = 1$, respectively. An enlargement as an inset in panel (b) emphasizes the small energetic difference between the binding energies for the $\text{MoS}_2 - \text{MoSe}_2$ heterojunction and the other two, $\text{MoS}_2 - \text{WSe}_2$ and $\text{MoS}_2 - \text{WS}_2$, double-layers. 62

- FIGURE 4.5 – (Color online) Binding energies (E_B) of the interlayer excitons in the MoSe₂ layer by taking different layer compounds in the TMD heterostructure formation. Red solid and cyan dashed curves correspond to MoSe₂ – WS₂ and WS₂ – MoSe₂, respectively, with the interlayer exciton being formed by the electron (hole) of the first (second) referred compound. Panels (a) and (b) show the dependence of E_B on the separation distance of the layers d , by assuming $\epsilon_1 = \epsilon_2 = \epsilon_m = 1$, and on the dielectric constant ϵ_m , by assuming a fixed interlayer distance of $d = 41 \text{ \AA}$ and dielectric constants of the substrate and superstrate as $\epsilon_1 = \epsilon_2 = 1$, respectively. An enlargement as an inset in panel (b) emphasizes the energetic difference between the binding energies for the MoSe₂ – WS₂ and WS₂ – MoSe₂ double-layers. 63
- FIGURE 4.6 – (Color online) Exciton energy dependency on (a) the layer separation and (b) the dielectric media ϵ_m for the MoS₂-MoSe₂ heterostructure. IX_{*i*} denotes the *i*-th interlayer exciton, such that IX₁ (IX₂) is formed by the electron from the lowest conduction band of the first (second) material and the hole from the highest valence band of the second (first) material with result represented by the solid red (dashed cyan) curve. Solid blue and yellow curves correspond to the intralayer excitons for MoSe₂ and MoS₂ cases, respectively. (a) All dielectric constants are held fixed with the value of 1, and (b) the layer separation is fixed to $d = 41 \text{ \AA}$. The shaded gray region corresponds to the continuum. An enlargement around small layer separation is shown as an inset of panel (a). 65
- FIGURE 4.7 – (Color online) Exciton energy dependency on (a) the layer separation and (b) the dielectric media ϵ_m for the MoSe₂-WSe₂ heterostructure. IX_{*i*} denotes the *i*-th interlayer exciton, such that IX₁ (IX₂) is formed by the electron from the lowest conduction band of the first (second) material and the hole from the highest valence band of the second (first) material with result represented by the solid red (dashed cyan) curve. Solid blue and yellow curves correspond to the intralayer excitons for WSe₂ and MoSe₂ cases, respectively. (a) All dielectric constants are held fixed with the value of 1, and (b) the layer separation is fixed to $d = 41 \text{ \AA}$. The shaded gray region corresponds to the continuum. 66

- FIGURE 4.8 – (Color online) (a,b) Intralayer and (c,d) interlayer exciton wave function for the MoS₂-MoSe₂ heterostructure as a function of (a,c) the layer separation and (b,d) the dielectric constant. The dielectric constants are held fixed at 1 for panels (a) and (c), whereas the value for the interlayer distance is fixed of $d = 41 \text{ \AA}$ in panels (b) and (d). 67
- FIGURE 4.9 – (Color online) Band alignment of MoS₂-WTe₂ bilayer. Here, the interlayer quasiparticle bandgap is the difference of the conduction band energy of MoS₂ and the valence band energy of WTe₂, $E_g = 0.49\text{eV}$. The values were taken from (ZHANG *et al.*, 2016). 68
- FIGURE 4.10 –(Color online) Band gap evolution with respect to the dielectric media and layer separation. 69
- FIGURE 4.11 –(Color Online) The exciton energy for each interlayer separation and dielectric media. The blue region is where the binding energy is greater than the band gap while the red region is where the binding energy is smaller than the band gap. The solid black line is the phase boundary, where the binding energy and bandgap are equal. In each panel, we set a particular dielectric substrate, a) $\epsilon_1 = 1$, b) $\epsilon_1 = 2$, c) $\epsilon_1 = 3$ and d) $\epsilon_1 = 4$ 70
- FIGURE 5.1 – (Color Online) Binding energy of the intralayer and interlayer exciton for different dielectric media (ϵ_m in ϵ_0 units) and separation distance (d in \AA units) in the black phosphorous homo-bilayer. In the right panels, we have the substrate and upper dielectric media with $\epsilon_m = 1$ and the in the left panels the interlayer distance is fixed at $d = 10\text{\AA}$. The parameters are given in Table 5.1. 78
- FIGURE 5.2 – (Color Online) Probability density of the ground state of the exciton for both intralayer and interlayer potential. In this case, the parameters are $d = 10 \text{ \AA}$, $\epsilon_1 = \epsilon_m = \epsilon_3 = 1$. The mass and screening parameters are given in table 5.1. The ratio of the directional radii, R_x/R_y , is practically constant independent of the system configuration, as one can see in table 5.3. 79

List of Tables

TABLE 3.1 –	The convergence of exciton ground state binding energy as a function of the number of radial momenta mesh points N_p , obtained with RK potential for the MoS ₂ from the Gauss-Legendre quadrature method. The number of angular mesh points is 61. The exciton binding energy of -753.1 meV for $N_p \rightarrow \infty$ is obtained with a quadratic extrapolation, while the Chebyshev Method yields a binding energy of -753.0 meV for $N = M = 600$ and $N_\theta = 320$, where N is the number of mesh points for the u variable, M is the number of terms in the finite decomposition and N_θ is the number of mesh points for the angular quadrature which stems from the partial-wave decomposition.	52
TABLE 4.1 –	Effective masses, screening factor r_0 , and the bandgap(ZHANG <i>et al.</i> , 2016) of each material. The masses are obtained from Ref. (KORMÁNYOS <i>et al.</i> , 2015) and the screening factors are obtained via a fitting procedure. The screening factors in the fifth column are from ref. (PEDERSEN, 2016), while the experimentally obtained binding energies for each row are, respectively (KLOTS <i>et al.</i> , 2014; XIE <i>et al.</i> , 2021; HARATS <i>et al.</i> , 2020; ASLAN <i>et al.</i> , 2021)	60
TABLE 4.2 –	<i>Ab initio</i> bandgaps (ZHANG <i>et al.</i> , 2016), Fermi velocity (KORMÁNYOS <i>et al.</i> , 2015) and calculated bare bandgaps using Eq. (4.3) and the fit r_0 's given in Table 4.1 for the four investigated TMDs and different combinations of spin and valley indexes.	61
TABLE 4.3 –	Effective masses, screening factor r_0 , and the band gap of each material. The masses are from (KORMÁNYOS <i>et al.</i> , 2015) and Δ_K from (ZHANG <i>et al.</i> , 2016). The screening factors, r_0 , for WTe ₂ are obtained from Eq. (4.2).	69

TABLE 5.1 –	Table of parameters used in this Chapter for the black phosphorous from Ref. (RODIN <i>et al.</i> , 2014). m_0 is the free electron mass. Notice the large value of m_y^h , which the it is reference claimed to be due to the flatness of the band in which the effective mass was calculated. .	77
TABLE 5.2 –	Converge check. Results for the exciton binding energy in a single layer of black phosphorous (parameters from Table 5.1) as a function of the number of mesh points, N , for both angular and radial variables. The grid is non-uniform, having $N/2$ for $[-1, -0.9]$, $N/4$ for $[-0.9, -0.8]$ and $N/4$ for $[-0.8, 1]$	77
TABLE 5.3 –	Direction Bohr radius, given in Eqs. (5.34). Here we consider an interlayer distance of $d = 10\text{\AA}$, and dielectric media composed of $\epsilon_1 = \epsilon_m = \epsilon_3 = 1$. The interlayer, and intralayer potentials are given in Eqs. (1.21) (1.22)	80

Contents

1	INTRODUCTION	18
1.1	2D Materials	18
1.1.1	Transition Metal Dichalcogenides	19
1.1.2	Black Phosphorous	20
1.2	The Exciton	21
1.2.1	Phenomenological Formulation of the Exciton	22
1.2.2	Electron-Hole Interaction	24
1.3	Objective and remarks	28
2	SEMICONDUCTOR BLOCH EQUATIONS	29
2.1	The Formulation of the Hamiltonian	29
2.2	Equations of Motion	34
2.3	Truncation of the Equations of Motion	37
2.4	Interpretation of the Dynamics	39
2.5	The Wannier Equation	41
3	NUMERICAL ANALYSIS OF THE WANNIER EQUATION	43
3.1	Partial-Wave Decomposition Approach	44
3.1.1	Chebyshev-Chawla-Kumar Method	45
3.1.2	Quadrature Solution	50
3.1.3	Comparison	51
3.2	2D Gauss-Legendre Quadrature	53
3.3	Variational Methods	53
3.3.1	Generating Coordinate Method	54

3.4	Final Remarks	55
4	TUNABLE PROPERTIES OF EXCITONS IN DOUBLE MONOLAYER SEMICONDUCTOR HETEROSTRUCTURES	57
4.1	Bandgap Engineering	58
4.2	Results	60
4.2.1	Excitonic-Based Insulating Phase in Bilayer MoS ₂ -WTe ₂	67
4.3	Conclusions	70
5	EXCITONS IN BLACK PHOSPHOROUS	72
5.1	The Hamiltonian	72
5.2	Wannier Equation	75
5.3	Binding Energy and Wave-Functions	77
5.4	Conclusion	80
6	CONCLUSION AND PERSPECTIVES	81
6.1	A Short Summary	81
6.2	Future Perspectives	82
	BIBLIOGRAPHY	83
	APPENDIX A – THREE-BODY HAMILTONIAN FOR THE PHOSPHORENE	91

1 Introduction

The interaction between light and matter constitutes a fundamental aspect of physics, encompassing a wide range of technological advancements such as LEDs, lasers, and various other devices. Light also plays a crucial role in the realm of life sciences. Notably, the process of photosynthesis, which is responsible for vegetation producing oxygen and sustaining the cycle of life on Earth, arises from the intricate interplay between light and matter. The classical depiction of light based on Maxwell's equations has served as a source of inspiration for generations of physicists and engineers. Meanwhile, the quantum formulation of light continues to drive significant scientific progress in areas like laser physics, cold atoms, and numerous other branches of physics.

In the domain of condensed matter physics, the interaction between light and matter assumes considerable significance and serves as a fundamental tool in many experimental methodologies (MOLAS *et al.*, 2021; WHITTOCK *et al.*, 2022). With regard to multi-band systems, wherein the electron gas exhibits a hierarchical coupling, correlated structures comprising electrons and holes emerge within semiconducting materials (KIRA; KOCH, 2006). These correlations manifest in various forms, including excitons (electron-hole pairs), trions (electron-electron-hole or electron-hole-hole triplets), and other composite particles. While previous investigations have explored these correlations, the advent of two-dimensional (2D) semiconducting materials has unveiled the formation of excitons possessing significantly larger binding energies than conventional semiconductors (BERKELBACH *et al.*, 2013; ZHANG *et al.*, 2014; HE *et al.*, 2014; YE *et al.*, 2014; UGEDA *et al.*, 2014; CHAVES *et al.*, 2021).

1.1 2D Materials

The proliferation of research on 2D materials represents one of the most dynamic fields within condensed matter physics. This trajectory commenced with the mechanical exfoliation of graphene (GEIM; NOVOSELOV, 2007; NOVOSELOV *et al.*, 2004), subsequently followed by the discovery of other layered materials (GEIM; GRIGORIEVA, 2013). During the initial stages of this research area, the scientific community primarily focused

on graphene until experimental studies involving monolayer MoS₂ uncovered its unique electronic and optical properties (UGEDA *et al.*, 2014; LI *et al.*, 2014). These investigations highlighted the existence of tightly bound excitons and opened up avenues for optoelectronic applications. The formation of such excitons hinges upon the interplay between reduced dimensionality and dielectric screening, which yields a strong Coulomb interaction (CHAVES *et al.*, 2017; TENÓRIO *et al.*, 2023; QUINTELA *et al.*, 2022). The layered nature of this class of materials facilitates the manipulation of their physical properties through energy level renormalization induced by environmental changes, consequently affecting the Coulomb interaction (KYLÄNPÄÄ; KOMSA, 2015; LAMOUNTAIN *et al.*, 2018). This characteristic enables bandgap engineering (CHAVES *et al.*, 2020) and tunability of excitonic spectra (TENÓRIO *et al.*, 2023).

By stacking different 2D materials, an additional degree of freedom emerges, leading to the creation of van der Waals heterostructures (GEIM; GRIGORIEVA, 2013). Through careful selection of materials, dielectric environments, and layer separations that result in favorable band alignments, these heterostructures offer intriguing opportunities for tailoring excitonic spectra. Given the limitless number of possible material combinations, dielectric environments, and layer arrangements, there is a strong motivation to systematically develop methods for computing the spectra of binding energies, understanding the behavior of basic wave functions, and characterizing the gap renormalization induced by varying environmental conditions. Consequently, undertaking a comprehensive investigation into these aspects of excitonic physics holds paramount importance.

1.1.1 Transition Metal Dichalcogenides

Initially discovered through exfoliation techniques in 2010 (GEIM; GRIGORIEVA, 2013; MAK *et al.*, 2010), transition metal dichalcogenides (TMDCs) swiftly garnered significant attention due to their promising optical and electronic properties (MATSUDA, 2015; WANG *et al.*, 2017; MAK; SHAN, 2016). Figure 1.1, panels (a) and (b), illustrates the class of TMDCs under consideration, which exhibit a trigonal prismatic structural phase. In the lateral view, the A-B-A stacking pattern is evident, comprising two planes of chalcogens and one atomic plane of a transition metal.

Panel (c) of the same figure displays the band structure of MoSe₂, highlighting the presence of a direct band gap at the K point. This particular region serves as the focal point for analyzing the excitonic properties of TMDCs. Notably, the influence of spin-orbit coupling on the band structure is prominently observed, a topic that will be explored further in Chapter 4. From the perspective of few-body theory, this class of 2D materials has garnered significant attention due to the remarkably large binding energies exhibited by even four-particle complexes (MAK *et al.*, 2013; BERKELBACH *et al.*, 2013; YOU *et al.*,

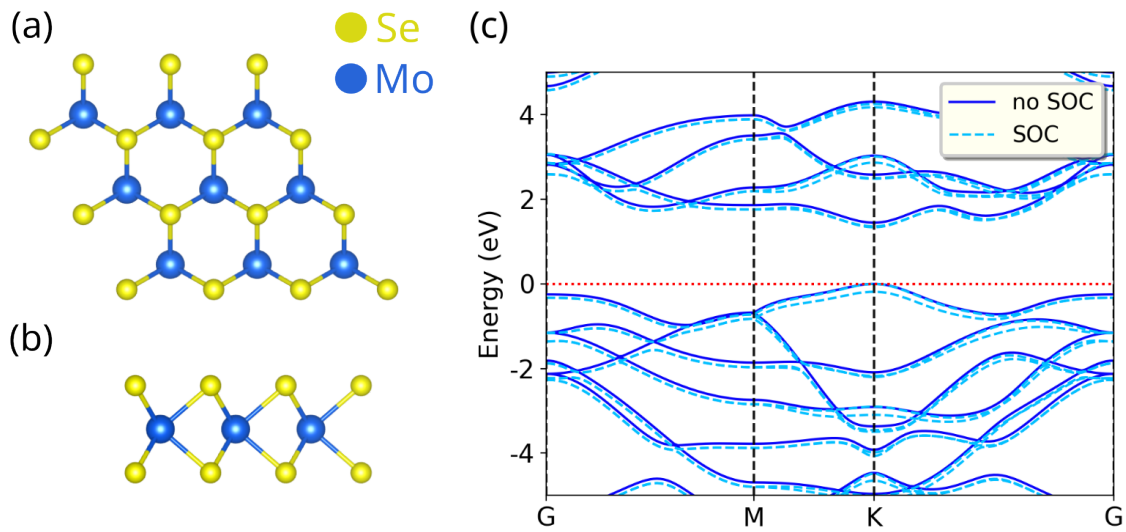


FIGURE 1.1 – (Color Online) Geometry and band structure of MoSe_2 . In (a) and (b) the top and side views of the molecular geometry is presented. In (c) we show the band structure of MoSe_2 . The band structure was calculated using density functional theory (HOHENBERG; KOHN, 1964; KOHN; SHAM, 1965).

2015). These pronounced binding energies in TMDCs have sparked considerable interest and intrigue within the scientific community.

1.1.2 Black Phosphorous

The monolayer black phosphorus material represents one of the more stable allotropes of phosphorus (see Fig. 1.2), exhibiting highly anisotropic properties that arise from its distinctive puckered structure (AKHTAR *et al.*, 2017; MOLAS *et al.*, 2021). The unique arrangement of atoms in black phosphorus gives rise to its remarkable electronic behavior and optical characteristics.

Of particular interest is the phenomenon of band gap engineering that can be achieved through the stacking of multiple layers of black phosphorus. By altering the number of layers and the arrangement in a stack, it becomes possible to modulate the band gap of the material. In the case of black phosphorus, the stacking of layers can effectively tune the band gap from the range of approximately 1.5 eV to a significantly reduced range of around 0.3 eV (CHAVES *et al.*, 2017). This tunability of the band gap holds great promise for various technological applications, enabling tailored electronic and optical properties in black phosphorus-based devices. Figure 1.2 provides insightful information regarding the band structure and geometric characteristics of the material under investigation. Examining panels (a), (b) and (c), it becomes evident that the crystalline structure of the material exhibits two distinct planar directions, commonly referred to as zig-zag and armchair orientations in the scientific literature (CHAVES *et al.*, 2017). This structural anisotropy plays a crucial role in influencing the light absorption properties of the material. Specifically,

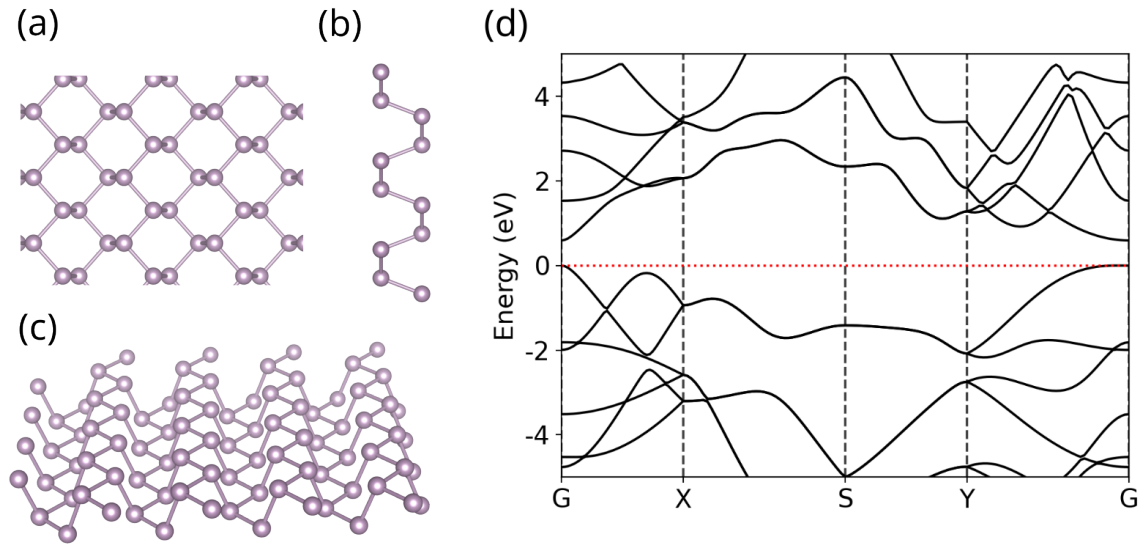


FIGURE 1.2 – (Color Online) Geometry and band structure of a black phosphorous monolayer. In (a), (b) and (c) the molecular geometry of the system is presented. In (d) we present the band structure of the monolayer black phosphorous. The band structure was calculated using density functional theory (HOHENBERG; KOHN, 1964; KOHN; SHAM, 1965).

the symmetries of the wave functions associated with the valence and conduction bands are affected by this anisotropy, leading to unique absorption characteristics (MOLAS *et al.*, 2021).

Panel (d) of Fig. 1.2 highlights another key feature of the system: it possesses a direct band gap. This attribute makes the material particularly conducive to the generation and study of excitons, which are bound electron-hole pairs. The presence of a direct band gap facilitates the formation and stability of excitonic states in the material, due to momentum conservation of direct transitions.

However, it is important to note that the anisotropy of the material poses challenges when performing calculations and simulations. The lack of isotropy, arising from the anisotropic nature of the material, introduces coupling between different angular momentum channels. This coupling complicates the computational procedures and necessitates careful consideration and handling of the anisotropy in theoretical calculations. Efforts must be made to appropriately account for the anisotropic effects and incorporate them into the calculations to obtain accurate and reliable results.

1.2 The Exciton

The interaction between light and the aforementioned materials gives rise to a multitude of processes that possess distinct properties, which in turn enable various technological applications (KIM, 2023; DHANABALAN *et al.*, 2017). When describing the optical

properties of solids, there are several frameworks one can adopt. While valid results can be obtained in the single-particle approximation through perturbation theory applied to a single-particle Hamiltonian with an effective potential coupled to a vector potential (RÖSSLER, 2009), a more comprehensive understanding of excited states is achieved through a many-body treatment. Electronic interactions in solids give rise to a hierarchical dependence between carriers, resulting in phenomena governed by two-particle excitons, three-particle trions (KOKSAL *et al.*, 2021; CHOI *et al.*, 2018), and even more complex structures involving six and eight particles (TUAN *et al.*, 2022). This intricate interplay of particles presents an intriguing context for studying few-body physics and applying effective field theory methods (see e.g. (KIRA; KOCH, 2006; SHANKAR, 1997)).

At the core of condensed matter physics lies the concept of emergent phenomena, popularized by Anderson (ANDERSON, 1972). It emphasizes that interacting systems in the thermodynamic limit exhibit a set of phenomena that cannot be solely derived by examining the individual components of the system in isolation. A notable example of this is the behavior of electrons in semiconductors, where they can be treated as quasiparticles with effective masses that are fractions of the electron mass (RÖSSLER, 2009). This approximation successfully captures important properties near high symmetry points in the Brillouin zone (YU; CARDONA, 2010).

Now the exciton and the interaction that leads to its formation is discussed in phenomenological terms. The underlying concepts that give rise to particular properties in materials, which stem from the interactions among multiple particles are presented next. The discussion is based on a set of references encompassing books and reviews by Combescot (COMBESCOT; SHIAU, 2015; COMBESCOT *et al.*, 2008), as well a seminal work by Kira *et al.* (KIRA; KOCH, 2006).

1.2.1 Phenomenological Formulation of the Exciton

Consider a periodic lattice. As is known by the Bloch's theorem (BLOCH, 1929), the periodicity of the system gives rise to energy bands. For a semiconducting material in the ground state, such bands may have either a complete filling or emptiness of electronic states. To formulate a simpler picture, consider a system composed of two different energy bands. Now, if one takes an electron from the band of the lowest energy, which is completely filled, and toss it up to the other band, of higher energy, one has what is called an excitation. Since the lower band, after tossing the electron to the higher band, has $N - 1$ particles, it can be effectively described as a particle with positive charge and mass, which is denoted as a "hole". Assign to the electron in the upper energy band and the hole in the lower energy band plane waves. By doing so, by virtue of the particle being charged, Coulomb processes start to become relevant, leading to a bound state of

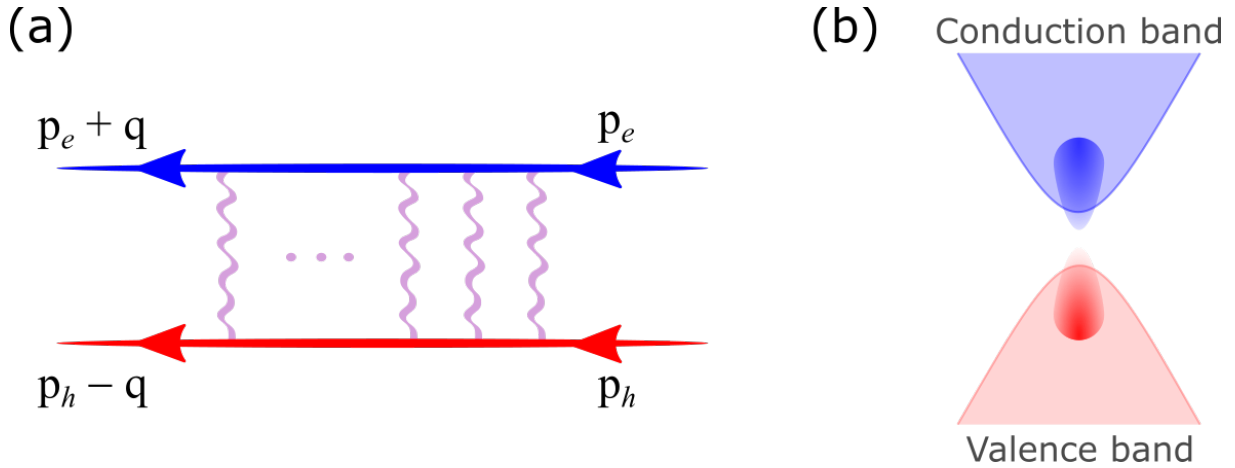


FIGURE 1.3 – (Color Online) Physical picture of the exciton formation. In (a) we show the ladder diagram responsible for the exciton pair. In (b) we present a schematic view of the exciton pair in a two-band system. The red and blue balls represents the electron and hole, respectively and the connecting shade is the electron-hole bound state, the exciton.

pair of particles.

The bound-state formed by these Coulomb processes of the electron and hole excitation is called the Exciton. Since each carrier should stay in its band, the dominant Coulomb processes responsible for the formation of excitons and localization in the center-of-mass frame are intraband Coulomb processes.

In a more precise fashion, let \mathbf{p}_e be the momentum of the excited electron in the higher band (ie. conduction band) and \mathbf{p}_h be the momentum of the hole in the lower band (ie. valence band). The physical picture of the electron-hole pair interacting with the Coulomb force is encapsulated in Fig. 1.3. The interaction between this pair is represented by a ladder diagram and the sum of all ladder diagrams leads to a correlated state, that can be bound or not (see panel (a) of Fig. 1.3). The bound-state resulting from this sum of ladder diagrams, for this kind of system with the Coulomb intraband processes is the Wannier Exciton. The two-band point of view is shown in panel (b) of Fig. 1.3. Although one can formulate a bound state equation from these considerations and the fact that the exciton is a hydrogen-like system, the excitonic spectra arises naturally in the interacting electron gas as a consequence of the hierarchical characteristics of the many-particle dynamics. In order to probe its effects and derive equations that governs the time-evolution of the polarization operator, an external electromagnetic field is introduced, yielding a set of coupled integro-differential equations which will describe optical properties through the linear response theory. Within appropriate approximations, this set of coupled equations also allows the study of excitonic properties through its homogeneous equation, which is also called Wannier equation. This equation will be the main subject of study for the large part of this work.

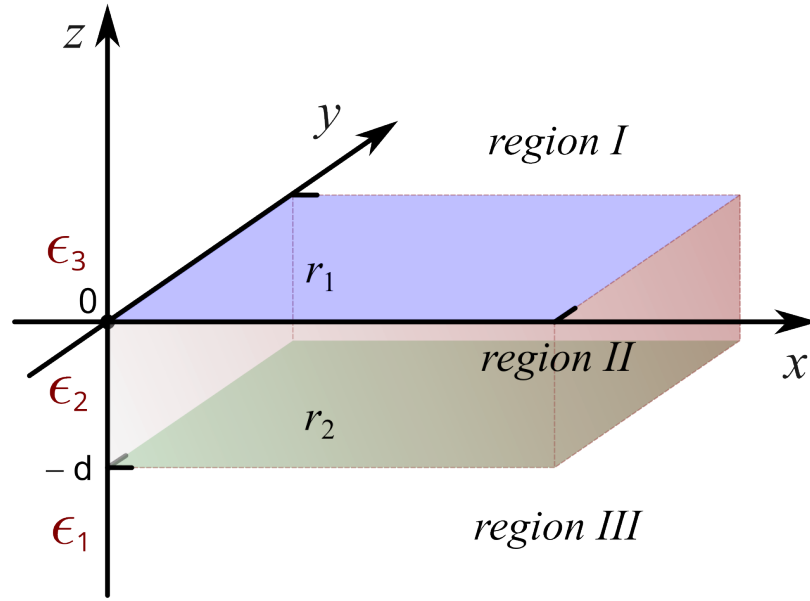


FIGURE 1.4 – (Color online) Schematic diagram of the electrostatic problem.

1.2.2 Electron-Hole Interaction

The exciton is formed by the screened Coulomb interaction between the carriers. Here, the derivation of the effective interaction considering two planar layers with particular polarization coefficients immersed in a dielectric media is presented in detail.

In order to derive the interaction potential for the chosen heterostructures, the Poisson equation has to be solved considering three dielectric regions separated by two layers located at $z = 0$ and $z = -d$, which separates the space into three regions (see Fig. 1.4 for the electrostatic picture). Each layer has a polarization coefficient denoted by r_1 and r_2 , respectively. Each region has a dielectric media with a dielectric constants ϵ_i in units of ϵ_0 . The Poisson equation is assembled by considering a charge Q_1 at $z = 0$. The presence of a charge at the uppermost layer will induce a charge density $\rho_{ind}(\vec{r})$ due to polarization. Therefore, the equation which one must solve is

$$-\nabla^2 \phi(\vec{r}) = \frac{1}{\epsilon_0} \rho(\vec{r}), \quad (1.1)$$

where ϵ_0 is the vacuum dielectric constant and the charge density $\rho(\vec{r})$ is,

$$-\nabla^2 \phi(\vec{r}) = \frac{1}{\epsilon_0} (Q_1 \delta(\vec{r}) + \rho_{ind}(\vec{r})). \quad (1.2)$$

The induced charge density term is,

$$\rho_{ind} = \sigma_1 \delta(z = 0) + \sigma_2 \delta(z + d) - \vec{\nabla} \cdot \vec{P}, \quad (1.3)$$

where \vec{P} is the medium polarization. Note that the induced charge densities, σ_1 and σ_2 , depend on the position in the respective layer, which is not explicitly depicted for the simplicity of our notation. By considering that the medium polarization is linear, the last term is rewritten as

$$\vec{\nabla} \cdot \vec{P} = \epsilon_0 \chi_i \vec{\nabla} \cdot \vec{E} = -\epsilon_0 \chi_i \nabla^2 \phi(\vec{r}), \quad (1.4)$$

where χ_i is the susceptibility of region i . Thus, we obtain the following partial differential equation,

$$-\nabla^2 \phi(\vec{r}) = \frac{1}{\epsilon_0} (Q_1 \delta(\vec{r}) + \sigma_1 \delta(z) + \sigma_2 \delta(z+d) + \epsilon_0 \chi_i \nabla^2 \phi(\vec{r})). \quad (1.5)$$

Next, apply a planar Fourier transform considering the (x, y) plane and rearrange the equation, leading to, for $z > 0$ (which encompasses region I , see Fig. 1.4),

$$(1 + \chi_1) \left(q^2 - \frac{\partial^2}{\partial z^2} \right) \Phi(\vec{q}, z) = 0, \quad (1.6)$$

where \vec{q} denotes the planar Fourier components. A possible solution for Eq. (1.6) is

$$\Phi(\vec{q}, z) = Ae^{-qz} + A'e^{qz}, \quad (1.7)$$

and by noting that in the limit of large z the potential should go to zero (due to the electrostatic physical boundary conditions), the solution is rewritten as,

$$\Phi(\vec{q}, z) = Ae^{-qz}, \quad z > 0. \quad (1.8)$$

Using a similar procedure for regions II and III , one obtains, respectively

$$\Phi(\vec{q}, z) = B \sinh(qz) + C \cosh(qz), \quad -d < z < 0, \quad (1.9)$$

$$\Phi(\vec{q}, z) = De^{qz}, \quad -d < z. \quad (1.10)$$

The physical potential should be continuous and to implement that, first, rearrange Eq. (1.5) and integrate it around each of the layers, and then, by continuity, a system of equations is obtained. Rearranging Eq. (1.5), yields

$$-(1 + \chi_i) \nabla^2 \phi(\vec{r}) = \frac{1}{\epsilon_0} (Q_1 \delta(\vec{r}) + \sigma_1 \delta(z) + \sigma_2 \delta(z+d)), \quad (1.11)$$

integrating around $z = 0$, after the planar Fourier transform in the (x, y) plane, in the

limit of $\delta \rightarrow 0_+$, one finds:

$$\int_{-\delta}^{+\delta} dz \epsilon_i \left(q^2 - \frac{\partial^2}{\partial z^2} \right) \Phi(\vec{q}, z) = -\epsilon_1 \frac{\partial \Phi(\vec{q}, z)}{\partial z} \Big|_{z=\delta} + \epsilon_2 \frac{\partial \Phi(\vec{q}, z)}{\partial z} \Big|_{z=-\delta} = \frac{Q_1}{\epsilon_0} + \frac{\Sigma_1}{\epsilon_0}, \quad (1.12)$$

where $\epsilon_i = 1 + \chi_i$ and Σ_1 depends on the planar Fourier component \vec{q} . Next, by evaluating the derivatives and taking the limit $\delta \rightarrow 0_+$, one obtains:

$$\epsilon_1 q A + \epsilon_2 q B = \frac{Q_1}{\epsilon_0} + \frac{\Sigma_1}{\epsilon_0}. \quad (1.13)$$

The planar Fourier transform of σ_1 is obtained using the in-plane polarization

$$\sigma_1 = -\vec{\nabla} \cdot \vec{P} \Big|_{z=0} = -r_1 \epsilon_0 \nabla^2 \phi(\vec{r}) \Big|_{z=0}, \quad (1.14)$$

which leads to:

$$\Sigma_1 = -r_1 \epsilon_0 q^2 \Phi(\vec{q}, z=0) = -r_1 \epsilon_0 q^2 A. \quad (1.15)$$

We use Eq. (1.13) to write one of the equations to obtain the coefficients A, B, C and D . By following the same reasoning above, but this time around $z = -d$, using expressions (1.9), (1.10), (1.11), and also by taking the limit as $\delta \rightarrow 0_+$ and noting that $A = C$, the aforementioned system of equations is obtained,

$$\begin{aligned} (\epsilon_1 q + r_1 q^2) A + \epsilon_2 B q &= \frac{Q_1}{\epsilon_0}, \\ -B \sinh(qd) + A \cosh(qd) &= D e^{-qd} \\ \epsilon_2 (B \cosh(qd) - A \sinh(qd)) &= (\epsilon_3 + r_2 q) D e^{-qd}, \end{aligned} \quad (1.16)$$

and using the third equation of (1.16),

$$D e^{-qd} = \epsilon_2 \frac{B \cosh(qd) - A \sinh(qd)}{\epsilon_3 + r_2 q}, \quad (1.17)$$

which in turn implies that only A and B are relevant. The solution of the system for A and B results in,

$$\begin{aligned} A &= \frac{-Q_1}{q \epsilon_0 (\epsilon_1 + r_1 q + \epsilon_2 G_2(q))}, \\ B &= G_2(q) \frac{Q_1}{q \epsilon_0 (\epsilon_1 + r_1 q + \epsilon_2 G_2(q))}, \end{aligned} \quad (1.18)$$

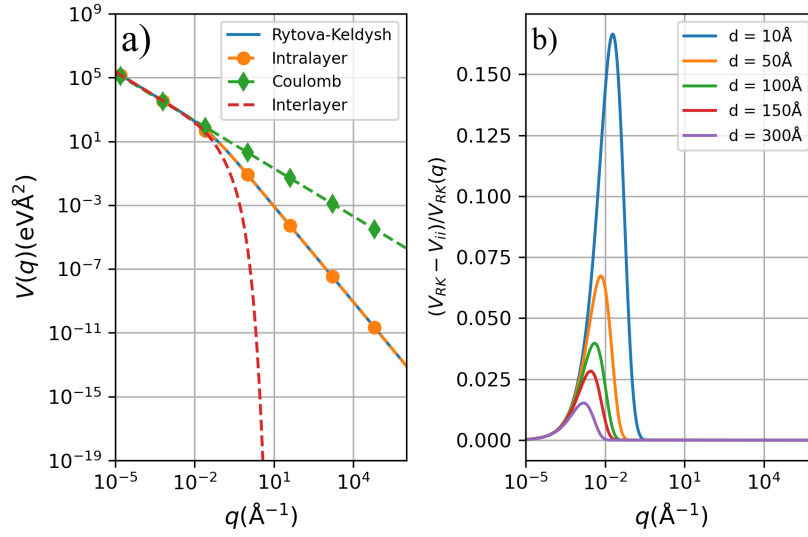


FIGURE 1.5 – (Color online) (a) Comparison between different carrier-carrier potentials in momentum space: RK (solid blue curve), Coulomb (dashed green curve with rhombus symbols), intralayer (dashed orange curve with circular symbols), and interlayer (dashed red curve) interactions. The interlayer [Eq. (1.21)] and the intralayer [Eq. (1.22)] potentials were calculated considering $r_1 = r_2 = r = 44.68 \text{ \AA}$ and $d = 7.15 \text{ \AA}$. When q is of the order of $1/r$, the Coulomb potential deviates from the other three and a negligible difference between the intralayer and the RK potentials is observed. The interlayer potential shows a strong screening that is due to the term proportional to e^{-qd} of $G_j(q)$ in Eq. (1.19) when $q \approx 1/d$. (b) The relative difference between the intralayer and the RK potentials, which can be as high as 15% the shorter the spacer width d

where

$$G_j(q) = \frac{\cosh(qd)(\epsilon_3 + r_j q) + \epsilon_2 \sinh(qd)}{\epsilon_2 \cosh(qd) + \sinh(qd)(\epsilon_3 + r_j q)}. \quad (1.19)$$

The potential in momentum space is then given by

$$\Phi(\vec{q}, z) = \begin{cases} Ae^{q(z+d)}(\cosh(qz) + G_2(q) \sinh(qz)) & \text{region III,} \\ A(\cosh(qz) - G_2(q) \sinh(qz)) & \text{region II,} \\ Ae^{-qz} & \text{region I,} \end{cases} \quad (1.20)$$

and, the relevant interactions are the intralayer and interlayer ones, which are explicitly written using equations (1.18), (1.19) and (1.20). By relabeling indices one writes that,

$$V_{ii}(q) = \frac{-e^2}{q\epsilon_0 [\epsilon_1 + r_i q + \epsilon_2 G_j(q)]}, \quad (1.21)$$

$$V_{i,j \neq i}(q) = \frac{e^2 [\cosh(qd) - G_j(q) \sinh(qd)]}{q\epsilon_0 [\epsilon_1 + r_i q + \epsilon_2 G_j(q)]}. \quad (1.22)$$

$V_{ii}(q)$ is the intralayer potential and $V_{i,j \neq i}(q)$ is the interlayer potential. The $G_j(q)$ has

the property that,

$$\lim_{d \rightarrow \infty} G_j(q) = \lim_{d \rightarrow \infty} \frac{e^{qd}(\epsilon_3 + r_j q) + \epsilon_2 e^{qd}}{\epsilon_2 e^{qd} + e^{qd}(\epsilon_3 + r_j q)} = 1, \quad (1.23)$$

using this result in Eq. (1.21),

$$V_{RK}(q) = \frac{-e^2}{q\epsilon_0(\epsilon_1 + \epsilon_2)(1 + \bar{r}_1 q)}, \quad (1.24)$$

where $\bar{r}_1 = r_1/(\epsilon_1 + \epsilon_2)$. Eq. (1.24) is the Rytova-Keldysh (RK)(RYTOVA, 1965; Keldysh, 1979) potential in momentum space, which is compared to the derived potential and the Coulomb potential in Fig. 1.5.

1.3 Objective and remarks

One of the primary goals of this research is to develop computationally efficient and reliable methods for describing the two-body system composed of an electron and a hole, which form an exciton. To achieve this goal, the necessary theoretical framework in which the exciton arises within a many-body context and influences important optical properties is established. Within this framework, one will encounter a key component known as the Wannier equation, which plays a central role in this dissertation. Once the formalism is developed and the Wannier equation is obtained, the solution methods are discussed in detail in Chapter 3.

One method worth highlighting involves the expansion of the wave function and the kernel of the Wannier equation as an infinite, truncated to a finite, series of Chebyshev polynomials. This approach allows to analytically circumvent the infrared divergence that typically arises in the context of Coulomb interactions. By constructing a properly tailored solution scheme, the Wannier equation is solved for a wide range of scenarios involving two-dimensional semiconducting heterostructures. This will enable to conduct a systematic investigation of the excitonic spectra and its influence on the band gap of the system through variations in the environment. A particular attention is drawn to the case of the MoS₂-WTe₂ heterostructure, where the potential emergence of an excitonic-driven insulating state is discussed at the end of Chapter 4.

Finally, the exciton in the context of monolayer and bilayer black phosphorous, a material that exhibits spatial anisotropy, leading to the breakdown of rotational symmetry and giving rise to a complex problem involving coupled integral equations is analyzed. The unique properties which arise from the charge carrier direction-dependent masses and its impacts in the wave function of the exciton are discussed in Chapter 5.

2 Semiconductor Bloch Equations

The quantum revolution that began in the early 20th century was driven by the profound understanding of the interaction between light and matter, as elucidated by Planck's theory (PLANCK; MASIUS, 1914). In the current era, we are witnessing another quantum revolution propelled by advancements in quantum computing and the relentless pursuit of miniaturizing technology, a trend that is particularly evident in the realm of 2D materials (NOVOSELOV *et al.*, 2016). Here we will present the derivation for the equations which are necessary to calculate the bandgap renormalization due to the change in the layer separation and dielectric media. For completeness we will also derive the equations which are used to obtain the optical response, known as the Semiconductor Bloch Equations (KIRA; KOCH, 2006).

To accurately describe the optical properties of 2D materials and highlight the role of few-body correlations, it is crucial to develop a robust set of theoretical tools to investigate the interaction between light and matter. In this work, we will adopt a formalism based on an electron gas interacting through a Coulomb-type coupling, specifically, a screened electrostatic interaction in a dielectric medium (RYTOVA, 1967; Keldysh, 1979).

Additionally, we will incorporate a term in the formalism to account for the influence of an external electromagnetic pulse, which we will model as a field-dipole coupling. While the concepts and techniques we will employ bear similarity to those found in standard textbooks such as (HAUG; KOCH, 2004; KIRA; KOCH, 2011), we will focus primarily on the unique properties exhibited by transition metal dichalcogenides (TMDCs), thus closely following the developments presented in (CHAVES *et al.*, 2017).

2.1 The Formulation of the Hamiltonian

The first ingredient in the Hamiltonian is a term that, for low energy excitation, captures the necessary physics with respect to the symmetries of the TMDC's electronic band structure (MATTHEISS, 1973) and the strong spin-orbit coupling (SOC) of this class of materials, in a two-band, free carrier approximation. The Hamiltonian in $\mathbf{k} \cdot \mathbf{p}$ approximation, first introduced in (XIAO *et al.*, 2012) and refined in (KORMÁNYOS *et al.*, 2013;

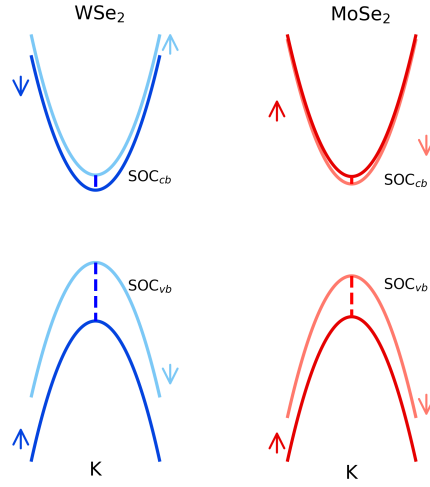


FIGURE 2.1 – (Color online) Illustration of band structure around the K point and SOC induced band splitting. We see a crossing between spin bands for the WSe_2 and no crossing for MoSe_2 .

KORMÁNYOS *et al.*, 2015; KORMÁNYOS *et al.*, 2014), has the form,

$$\hat{\mathcal{H}}_{0,i}^{s,\tau} = \hbar v_{F,i} \hat{\boldsymbol{\sigma}} \cdot \hat{\mathbf{p}}_i + \Delta_{s,\tau}^0 \sigma_z = \begin{pmatrix} \Delta_{s,\tau}^0 & \hbar v_{F,i} (\tau p_x - i p_y) \\ \hbar v_{F,i} (\tau p_x + i p_y) & -\Delta_{s,\tau}^0 \end{pmatrix}, \quad (2.1)$$

where i is the layer index, s, τ ($\tau = \pm 1$) are the spin and valley index, respectively. $\Delta_{s,\tau}^0$ is the mass term for the Dirac equation, which is the bare "bandgap", $\hat{\mathbf{p}} = (\tau p_x, p_y, 0)$, σ are the Pauli matrices, and \hat{I} is the identity matrix. This free system can be exactly diagonalized, with eigenvalues,

$$E_{\mathbf{p}}^{s\tau} = \pm \sqrt{(\hbar v_{F,i})^2 \mathbf{p} \cdot \mathbf{p} + (\Delta_{s,\tau}^0)^2} \quad (2.2)$$

By introducing a index λ that has value -1 for the valence band and $+1$ for the conduction band, the free carrier Hamiltonian in second quantization is

$$\hat{\mathcal{H}}_{0,i}^{s,\tau} = \sum_{\mathbf{p}, \lambda} \lambda E_{\mathbf{p}}^{s,\tau} \hat{a}_{\mathbf{p}, \lambda, s, \tau}^\dagger(t) \hat{a}_{\mathbf{p}, \lambda, s, \tau}(t), \quad (2.3)$$

where $a_{\lambda, \mathbf{p}}^\dagger$ ($a_{\lambda, \mathbf{p}}$) are creation (annihilation) operators. The free carrier Hamiltonian captures the basic properties of the band structure and the SOC induced band splitting, as it is illustrated in Fig. 2.1.

The next ingredient is the two-body interaction between the carriers, mediated by a

central potential $V(|\mathbf{r}_2 - \mathbf{r}_1|)$, which reads in second quantization as,

$$\mathcal{H}_{ee} = -\frac{e}{2} \int d\mathbf{r}_1 \int d\mathbf{r}_2 \hat{\psi}^\dagger(\mathbf{r}_1, t) \hat{\psi}^\dagger(\mathbf{r}_2, t) V(|\mathbf{r}_2 - \mathbf{r}_1|) \hat{\psi}(\mathbf{r}_2, t) \hat{\psi}(\mathbf{r}_1, t). \quad (2.4)$$

The field operator $\hat{\psi}$ can be expanded using the solutions of Eq. (2.1),

$$\hat{\psi}(\mathbf{r}, t) = \frac{1}{\sqrt{A}} \sum_{\mathbf{p}\lambda s\tau} \phi_{\mathbf{p}\lambda}^{s\tau} \hat{a}_{\mathbf{p}\lambda s\tau}(t) e^{i\mathbf{p}\cdot\mathbf{r}}, \quad (2.5)$$

where A is the area by which we quantize the plane wave momentum and $\hat{a}_{\mathbf{p},\lambda,s,\tau}$ is the fermionic annihilation operator that obeys anti-commutation relations,

$$\{\hat{a}_{\mathbf{p},\lambda,s,\tau}, \hat{a}_{\mathbf{p}',\lambda',s',\tau'}^\dagger\} = \delta_{\mathbf{p},\mathbf{p}'} \delta_{\lambda,\lambda'} \delta_{s,s'} \delta_{\tau,\tau'}. \quad (2.6)$$

The spinor $\phi_{\mathbf{p}\lambda}^{s\tau}$, solution to (2.1) is,

$$\phi_{\mathbf{p}\lambda}^{s\tau} = \sqrt{\frac{E_{\mathbf{p}}^{s\tau} + \lambda \Delta_{s\tau}^0}{2E_{\mathbf{p}}^{s\tau}}} \begin{pmatrix} 1 \\ \frac{\tau p_x - i p_y}{\lambda E_{\mathbf{p}}^{s\tau} - \Delta_{s\tau}^0} \end{pmatrix} \quad (2.7)$$

The electron-electron interaction is written using (2.7),

$$\hat{\mathcal{H}}_{ee} = \frac{-e}{2A^2} \sum_{s\tau} \sum_{\{\mathbf{p}_i, \lambda_i\}} \int d\mathbf{r}_1 d\mathbf{r}_2 (\phi_{\mathbf{p}_1 \lambda_1}^{s\tau})^\dagger \hat{a}_{\mathbf{p}_1 \lambda_1 s\tau}^\dagger(t) e^{-i\mathbf{p}_1 \cdot \mathbf{r}_1} (\phi_{\mathbf{p}_2 \lambda_2}^{s\tau})^\dagger \hat{a}_{\mathbf{p}_2 \lambda_2 s\tau}^\dagger(t) e^{-i\mathbf{p}_2 \cdot \mathbf{r}_2} \\ V(|\mathbf{r}_2 - \mathbf{r}_1|) \phi_{\mathbf{p}_3 \lambda_3}^{s\tau} \hat{a}_{\mathbf{p}_3 \lambda_3 s\tau}(t) e^{i\mathbf{p}_3 \cdot \mathbf{r}_2} \phi_{\mathbf{p}_4 \lambda_4}^{s\tau} \hat{a}_{\mathbf{p}_4 \lambda_4 s\tau}(t) e^{i\mathbf{p}_4 \cdot \mathbf{r}_1}, \quad (2.8)$$

where $\{\dots\}$ under the sum is indicating a sum over all indexes inside the curly brackets. One can decompose the two-body interaction in terms of its Fourier expansion for the exchanged momentum \mathbf{q} ,

$$\hat{\mathcal{H}}_{ee} = \frac{-e}{2A^3} \sum_{s\tau, \mathbf{q} \neq 0} \sum_{\{\mathbf{p}_i, \lambda_i\}} V(\mathbf{q}) \int d\mathbf{r}_1 (\phi_{\mathbf{p}_1 \lambda_1}^{s\tau})^\dagger (\phi_{\mathbf{p}_4 \lambda_4}^{s\tau}) e^{i(\mathbf{p}_4 - \mathbf{p}_1 - \mathbf{q}) \cdot \mathbf{r}_1} \\ \times \int d\mathbf{r}_2 (\phi_{\mathbf{p}_2 \lambda_2}^{s\tau})^\dagger (\phi_{\mathbf{p}_3 \lambda_3}^{s\tau}) e^{i(\mathbf{p}_3 - \mathbf{p}_2 + \mathbf{q}) \cdot \mathbf{r}_2} \hat{a}_{\mathbf{p}_1 \lambda_1 s\tau}^\dagger(t) \hat{a}_{\mathbf{p}_2 \lambda_2 s\tau}^\dagger(t) \hat{a}_{\mathbf{p}_3 \lambda_3 s\tau}(t) \hat{a}_{\mathbf{p}_4 \lambda_4 s\tau}(t), \quad (2.9)$$

and by integrating the spatial coordinates, one finds that:

$$\hat{\mathcal{H}}_{ee} = \frac{-e}{2A} \sum_{\{\mathbf{p}_i, \lambda_i\}} \sum_{\mathbf{q} \neq 0, s, \tau} V(\mathbf{q}) (\phi_{\mathbf{p}_1 \lambda_1}^{s\tau})^\dagger (\phi_{\mathbf{p}_4 \lambda_4}^{s\tau}) \delta_{\mathbf{p}_1, \mathbf{p}_4 - \mathbf{q}} \delta_{\mathbf{p}_2, \mathbf{p}_3 + \mathbf{q}} \times \\ \times (\phi_{\mathbf{p}_2 \lambda_2}^{s\tau})^\dagger (\phi_{\mathbf{p}_3 \lambda_3}^{s\tau}) \hat{a}_{\mathbf{p}_1 \lambda_1 s\tau}^\dagger(t) \hat{a}_{\mathbf{p}_2 \lambda_2 s\tau}^\dagger(t) \hat{a}_{\mathbf{p}_3 \lambda_3 s\tau}(t) \hat{a}_{\mathbf{p}_4 \lambda_4 s\tau}(t), \quad (2.10)$$

finally, for simplicity, we relabel the indices and get:

$$\hat{\mathcal{H}}_{ee} = \frac{-e}{2A} \sum_{s,\tau,\{\lambda_i\}} \sum_{\mathbf{p},\mathbf{p}',\mathbf{q}\neq 0} V(q) \mathcal{F}_{\{\lambda_i\}}(\mathbf{p}, \mathbf{p}', \mathbf{q}) \hat{a}_{\mathbf{p}-\mathbf{q},\lambda_1 s\tau}^\dagger(t) \hat{a}_{\mathbf{p}'+\mathbf{q},\lambda_2 s\tau}^\dagger(t) \hat{a}_{\mathbf{p}',\lambda_3 s\tau}(t) \hat{a}_{\mathbf{p},\lambda_4 s\tau}(t), \quad (2.11)$$

where,

$$\mathcal{F}_{\lambda_1\lambda_4\lambda_2\lambda_3}(\mathbf{p}, \mathbf{p}', \mathbf{q}) = (\phi_{\mathbf{p}+\mathbf{q},\lambda_1}^{s\tau})^\dagger (\phi_{\mathbf{p}\lambda_4}^{s\tau}) (\phi_{\mathbf{p}'-\mathbf{q},\lambda_2}^{s\tau})^\dagger (\phi_{\mathbf{p}'\lambda_3}^{s\tau}). \quad (2.12)$$

Now, in order to probe the optical properties of this interacting electron gas, one must incorporate a term that encapsulates the coupling of dipole moments formed due to the polarization of the electron gas to an external light pulse, that is, a term of the form,

$$\mathcal{H}_I = -e\mathcal{E}(t)\hat{x}. \quad (2.13)$$

Here we consider a time-dependent electric field polarized in the \hat{x} direction. Now, introduce the polarization operator $\mathbf{P}(t)$,

$$\mathbf{P}(t) = \int d\mathbf{r}_1 \hat{\psi}^\dagger(\mathbf{r}_1, t) (-e\mathbf{r}_1) \hat{\psi}(\mathbf{r}_1, t). \quad (2.14)$$

One can recast the polarization operator using the spinor solutions (2.7) of the free carrier Hamiltonian,

$$\mathbf{P}(t) = \frac{1}{A} \sum_{\{\mathbf{p}\lambda s\tau\}} \int d\mathbf{r}_1 (\phi_{\mathbf{p}\lambda}^{s\tau})^\dagger e^{-i\mathbf{p}'\cdot\mathbf{r}_1} (-e\mathbf{r}_1) e^{i\mathbf{p}\cdot\mathbf{r}_1} \phi_{\mathbf{p}'\lambda'}^{s'\tau'} \hat{a}_{\mathbf{p}\lambda s\tau}^\dagger(t) \hat{a}_{\mathbf{p}'\lambda' s'\tau'}(t). \quad (2.15)$$

Consider in particular the spatial integral,

$$\int d\mathbf{r}_1 (\phi_{\mathbf{p}\lambda}^{s\tau})^\dagger e^{-i\mathbf{p}'\cdot\mathbf{r}_1} (-e\mathbf{r}_1) e^{i\mathbf{p}\cdot\mathbf{r}_1} \phi_{\mathbf{p}'\lambda'}^{s'\tau'} = \langle \mathbf{p}, \lambda, \tau, s | \mathbf{r}_1 | \mathbf{p}', \lambda', \tau', s' \rangle, \quad (2.16)$$

notice that, by using the fact that this state yields the eigenvalues (2.2),

$$\langle \mathbf{p}, \lambda, \tau, s | \mathbf{r}_1 | \mathbf{p}', \lambda', \tau', s' \rangle = \langle \mathbf{p}, \lambda, \tau, s | \mathbf{r}_1 | \mathbf{p}', \lambda', \tau', s' \rangle \frac{\lambda E_{\mathbf{p}}^{s,\tau} - \lambda' E_{\mathbf{p}'}^{s',\tau'}}{\lambda E_{\mathbf{p}}^{s,\tau} - \lambda' E_{\mathbf{p}'}^{s',\tau'}} \quad (2.17)$$

by rearranging the eigenvalues of the numerator in terms of left-and-right applied $\hat{\mathcal{H}}_{0,i}$, it is obtained

$$\langle \mathbf{p}, \lambda, \tau, s | \mathbf{r}_1 | \mathbf{p}', \lambda', \tau', s' \rangle = \frac{\langle \mathbf{p}, \lambda, \tau, s | \left(\mathbf{r}_1 \hat{\mathcal{H}}_{0,i} - \hat{\mathcal{H}}_{0,i} \mathbf{r}_1 \right) | \mathbf{p}', \lambda', \tau', s' \rangle}{\lambda E_{\mathbf{p}}^{s,\tau} - \lambda' E_{\mathbf{p}'}^{s',\tau'}}, \quad (2.18)$$

therefore,

$$\langle \mathbf{p}, \lambda, \tau, s | \mathbf{r}_1 | \mathbf{p}', \lambda', \tau', s' \rangle = \frac{\langle \mathbf{p}, \lambda, \tau, s | [\mathbf{r}_1, \hat{\mathcal{H}}_{0,i}] | \mathbf{p}', \lambda', \tau', s' \rangle}{\lambda E_{\mathbf{p}}^{s,\tau} - \lambda' E_{\mathbf{p}'}^{s',\tau'}}. \quad (2.19)$$

Since the external field is polarized in the \hat{x} direction and the system electrically neutral, the central object is the interband transitions ($\lambda \neq \lambda'$),

$$\langle \mathbf{p}, \lambda, \tau, s | \hat{x} | \mathbf{p}', -\lambda, \tau', s' \rangle = \frac{\langle \mathbf{p}, \lambda, \tau, s | [\hat{x}, \hat{\mathcal{H}}_{0,i}] | \mathbf{p}', \lambda', \tau', s' \rangle}{\lambda E_{\mathbf{p}}^{s,\tau} - \lambda' E_{\mathbf{p}'}^{s',\tau'}}. \quad (2.20)$$

The calculation of the commutator is direct and the final expression for the polarization operator is,

$$\langle \mathbf{p}, \lambda, \tau, s | \hat{x} | \mathbf{p}', -\lambda, \tau', s' \rangle = \delta_{\mathbf{p},\mathbf{p}'} \delta_{\tau,\tau'} \delta_{s,s'} \frac{i\tau \hbar v_{f,i} \langle \mathbf{p}, \lambda, \tau, s | \sigma_1 | \mathbf{p}, -\lambda, \tau, s \rangle}{2\lambda E_{\mathbf{p}}^{s,\tau}} \quad (2.21)$$

$$= \delta_{\mathbf{p},\mathbf{p}'} \delta_{\tau,\tau'} \delta_{s,s'} \frac{i\nu_{\mathbf{p},\lambda}^{s,\tau}}{2\lambda E_{\mathbf{p}}^{s,\tau}}, \quad (2.22)$$

where, $\nu_{\mathbf{p},\lambda}^{s,\tau} = \tau \hbar v_{f,i} \langle \mathbf{p}, \lambda, \tau, s | \sigma_1 | \mathbf{p}, -\lambda, \tau, s \rangle$ is the matrix element considering a interband transition. Combining Eqs. (2.21) and (2.15), we can write that:

$$\hat{P}(t) = -e \sum_{\mathbf{p}^{s\tau}, \lambda} \frac{i\nu_{\mathbf{p},\lambda}^{s,\tau}}{2\lambda E_{\mathbf{p}}^{s,\tau}} \hat{a}_{\mathbf{p}\lambda s\tau}^\dagger(t) \hat{a}_{\mathbf{p}-\lambda s\tau}(t), \quad (2.23)$$

where it is convenient to introduce the following density matrix operator,

$$\hat{\rho}_{\mathbf{p},\lambda,\lambda'}^{s\tau}(t) = \hat{a}_{\mathbf{p}\lambda s\tau}^\dagger(t) \hat{a}_{\mathbf{p}\lambda' s\tau}(t). \quad (2.24)$$

Using the preceding discussion, the external field term is,

$$\hat{P}(t) = -e \sum_{\mathbf{p}^{s\tau}, \lambda} \frac{i\nu_{\mathbf{p},\lambda}^{s,\tau}}{2\lambda E_{\mathbf{p}}^{s,\tau}} \hat{\rho}_{\mathbf{p},\lambda,-\lambda}^{s\tau}(t), \quad (2.25)$$

$$\hat{\mathcal{H}}_I = -e\mathcal{E}(t) \sum_{\mathbf{p}^{s\tau}, \lambda} \frac{i\nu_{\mathbf{p},\lambda}^{s,\tau}}{2\lambda E_{\mathbf{p}}^{s,\tau}} \hat{\rho}_{\mathbf{p},\lambda,-\lambda}^{s\tau}(t). \quad (2.26)$$

The full Hamiltonian including the electron-electron interaction and the coupling to

the external electric field is:

$$\begin{aligned} \hat{\mathcal{H}} = & \sum_{\mathbf{p}, \lambda} \lambda E_{\lambda, \mathbf{p}} \hat{a}_{\lambda, \mathbf{p}}^\dagger(t) \hat{a}_{\lambda, \mathbf{p}}(t) - \frac{e}{2A} \sum_{\mathbf{p}, \mathbf{p}', \mathbf{q} \neq 0} \sum_{s, \tau, \{\lambda_i\}} V(q) \mathcal{F}_{\{\lambda_i\}}(\mathbf{p}, \mathbf{p}', \mathbf{q}) \\ & \times \hat{a}_{\mathbf{p}-\mathbf{q}, \lambda_1 s \tau}^\dagger(t) \hat{a}_{\mathbf{p}'+\mathbf{q}, \lambda_2 s \tau}^\dagger(t) \hat{a}_{\mathbf{p}' \lambda_3 s \tau}(t) \hat{a}_{\mathbf{p} \lambda_4 s \tau}(t) - e \mathcal{E}(t) \sum_{\mathbf{p} s \tau, \lambda} \frac{i \mathcal{W}_{\mathbf{p}, \lambda}^{s, \tau}}{2 \lambda E_{\mathbf{p}}^{s, \tau}} \hat{\rho}_{\mathbf{p}, \lambda, -\lambda}^{s \tau}(t) \end{aligned} \quad (2.27)$$

The Hamiltonian given in (2.27) describes a interacting electron gas which has two energy bands given by the λ index, that is interpret as the valence ($-$) and conduction($+$) bands. The interaction term creates a hierarchical dependence between particles and the external field is a way to study the response of the system to this field in the form of the polarization operator. The time evolution of the polarization operator give us the optical response of the system.

2.2 Equations of Motion

As it is explicit in Eq. (2.23), the time evolution of the polarization operator is directly associated to the time evolution of the density matrix, which is the central theme of this section.

The Heisenberg equation of motion is

$$-i\hbar \frac{d}{dt} \langle \hat{\rho}_{\mathbf{p}, \lambda, \lambda'}^{s \tau}(t) \rangle = \langle [\hat{\mathcal{H}}_{0, i}, \hat{\rho}_{\mathbf{p}, \lambda, \lambda'}^{s \tau}(t)] \rangle + \langle [\hat{\mathcal{H}}_{ee}, \hat{\rho}_{\mathbf{p}, \lambda, \lambda'}^{s \tau}(t)] \rangle + \langle [\hat{\mathcal{H}}_I, \hat{\rho}_{\mathbf{p}, \lambda, \lambda'}^{s \tau}(t)] \rangle. \quad (2.28)$$

One needs to calculate a series of commutators in Eq. (2.28), which couple the transition probabilities to quadratic and quartic operator products of creation and annihilation operators. In this section, the calculations of the commutators are detailed in what follows.

First, we compute free Hamiltonian contribution:

$$\begin{aligned} [\hat{\mathcal{H}}_{0, i}, \hat{\rho}_{\mathbf{p}', \lambda', \lambda''}^{s \tau}(t)] &= \sum_{\mathbf{p}, \lambda, s, \tau} \lambda E_{\mathbf{p}}^{s, \tau} \left[\hat{a}_{\mathbf{p}, \lambda, s, \tau}^\dagger \hat{a}_{\mathbf{p}, \lambda, s, \tau} \hat{a}_{\mathbf{p}', \lambda', s', \tau'}^\dagger \hat{a}_{\mathbf{p}' \lambda'' s' \tau'} - \hat{a}_{\mathbf{p}', \lambda', s', \tau'}^\dagger \hat{a}_{\mathbf{p}' \lambda'' s' \tau'} \hat{a}_{\mathbf{p}, \lambda, s, \tau}^\dagger \hat{a}_{\mathbf{p}, \lambda, s, \tau} \right] \\ &= \sum_{\mathbf{p}, \lambda, s, \tau} \lambda E_{\mathbf{p}}^{s, \tau} \left(\hat{a}_{\mathbf{p}, \lambda, s, \tau}^\dagger \hat{a}_{\mathbf{p}, \lambda, s, \tau} \hat{a}_{\mathbf{p}', \lambda', s', \tau'}^\dagger \hat{a}_{\mathbf{p}' \lambda'' s' \tau'} - \hat{a}_{\mathbf{p}', \lambda', s', \tau'}^\dagger \hat{a}_{\mathbf{p}' \lambda'' s' \tau'} \hat{a}_{\mathbf{p}, \lambda, s, \tau}^\dagger \hat{a}_{\mathbf{p}, \lambda, s, \tau} \right) \\ &= \sum_{\mathbf{p}, \lambda, s, \tau} \lambda E_{\mathbf{p}}^{s, \tau} \hat{a}_{\mathbf{p}, \lambda, s, \tau}^\dagger \left(\{ \hat{a}_{\mathbf{p}, \lambda, s, \tau}, \hat{a}_{\mathbf{p}', \lambda', s', \tau'}^\dagger \} - \hat{a}_{\mathbf{p}', \lambda', s', \tau'}^\dagger \hat{a}_{\mathbf{p}, \lambda, s, \tau} \right) \hat{a}_{\mathbf{p}' \lambda'' s' \tau'} - \\ &\quad - \sum_{\mathbf{p}, \lambda, s, \tau} \lambda E_{\mathbf{p}}^{s, \tau} \hat{a}_{\mathbf{p}', \lambda', s', \tau'}^\dagger \left(\{ \hat{a}_{\mathbf{p}', \lambda'', s', \tau'}, \hat{a}_{\mathbf{p}, \lambda, s, \tau}^\dagger \} - \hat{a}_{\mathbf{p}, \lambda, s, \tau}^\dagger \hat{a}_{\mathbf{p}', \lambda'', s', \tau'} \right) \hat{a}_{\mathbf{p} \lambda s \tau} \end{aligned} \quad (2.29)$$

by employing the anti-commutation relation (2.6),

$$\begin{aligned}
\left[\hat{\mathcal{H}}_{0,i}, \hat{\rho}_{\mathbf{p}',\lambda',\lambda''}^{s\tau}(t) \right] &= \sum_{\mathbf{p},\lambda,s,\tau} \lambda E_{\mathbf{p}}^{s,\tau} \hat{a}_{\mathbf{p},\lambda,s,\tau}^{\dagger} \left(\delta_{\mathbf{p},\mathbf{p}'} \delta_{\lambda,\lambda'} \delta_{s,s'} \delta_{\tau,\tau'} - \hat{a}_{\mathbf{p}',\lambda',s',\tau'}^{\dagger} \hat{a}_{\mathbf{p},\lambda,s,\tau} \right) \hat{a}_{\mathbf{p}'\lambda''s'\tau'} - \\
&\quad - \sum_{\mathbf{p},\lambda,s,\tau} \lambda E_{\mathbf{p}}^{s,\tau} \hat{a}_{\mathbf{p}',\lambda',s',\tau'}^{\dagger} \left(\delta_{\mathbf{p},\mathbf{p}'} \delta_{\lambda,\lambda''} \delta_{s,s'} \delta_{\tau,\tau'} - \hat{a}_{\mathbf{p},\lambda,s,\tau}^{\dagger} \hat{a}_{\mathbf{p}',\lambda'',s',\tau'} \right) \hat{a}_{\mathbf{p}\lambda s\tau} \\
&= \sum_{\mathbf{p},\lambda,s,\tau} \lambda E_{\mathbf{p}}^{s,\tau} \hat{a}_{\mathbf{p},\lambda,s,\tau}^{\dagger} \hat{a}_{\mathbf{p}'\lambda''s'\tau'} \delta_{\mathbf{p},\mathbf{p}'} \delta_{\lambda,\lambda'} \delta_{s,s'} \delta_{\tau,\tau'} - \sum_{\mathbf{p},\lambda,s,\tau} \lambda E_{\mathbf{p}}^{s,\tau} \hat{a}_{\mathbf{p}',\lambda',s',\tau'}^{\dagger} \hat{a}_{\mathbf{p}\lambda s\tau} \delta_{\mathbf{p},\mathbf{p}'} \delta_{\lambda,\lambda''} \delta_{s,s'} \delta_{\tau,\tau'} \\
&= \lambda' E_{\mathbf{p}}^{s,\tau} \hat{a}_{\mathbf{p},\lambda',s,\tau}^{\dagger} \hat{a}_{\mathbf{p}\lambda''s\tau} - \lambda'' E_{\mathbf{p}}^{s,\tau} \hat{a}_{\mathbf{p},\lambda',s,\tau}^{\dagger} \hat{a}_{\mathbf{p}\lambda''s\tau} = (\lambda' - \lambda'') E_{\mathbf{p}}^{s,\tau} \hat{a}_{\mathbf{p},\lambda',s,\tau}^{\dagger} \hat{a}_{\mathbf{p}\lambda''s\tau}, \quad (2.30)
\end{aligned}$$

where one can identify the last operator product as the density operator, which yields directly the argument of the first term of (2.28),

$$\left[\hat{\mathcal{H}}_{0,i}, \hat{\rho}_{\mathbf{p}',\lambda',\lambda''}^{s\tau}(t) \right] = (\lambda' - \lambda'') E_{\mathbf{p}}^{s,\tau} \hat{\rho}_{\mathbf{p},\lambda',\lambda''}^{s\tau}(t). \quad (2.31)$$

The contribution from electron-electron interaction commutator to Eq. (2.28) is explicitly written as:

$$\begin{aligned}
\left[\hat{\mathcal{H}}_{ee}, \hat{\rho}_{\mathbf{p}'',\lambda,\lambda'}^{s\tau}(t) \right] &= \frac{-e}{2A} \sum_{s,\tau,s',\tau',\{\lambda_i\}} \sum_{\mathbf{p},\mathbf{p}',\mathbf{q} \neq 0} V(q) \mathcal{F}_{\{\lambda_i\}}(\mathbf{p}, \mathbf{p}', \mathbf{q}) \\
&\quad \times \left[\hat{a}_{\mathbf{p}-\mathbf{q},\lambda_1s\tau}^{\dagger} \hat{a}_{\mathbf{p}'+\mathbf{q},\lambda_2s\tau}^{\dagger} \hat{a}_{\mathbf{p}'\lambda_3s\tau} \hat{a}_{\mathbf{p}\lambda_4s\tau}, \hat{a}_{\mathbf{p}''\lambda's'\tau'}^{\dagger} \hat{a}_{\mathbf{p}''\lambda''s'\tau'} \right]. \quad (2.32)
\end{aligned}$$

where the commutator is,

$$\begin{aligned}
\left[\hat{a}_{\mathbf{p}-\mathbf{q},\lambda_1s\tau}^{\dagger} \hat{a}_{\mathbf{p}'+\mathbf{q},\lambda_2s\tau}^{\dagger} \hat{a}_{\mathbf{p}'\lambda_3s\tau} \hat{a}_{\mathbf{p}\lambda_4s\tau}, \hat{a}_{\mathbf{p}''\lambda's'\tau'}^{\dagger} \hat{a}_{\mathbf{p}''\lambda''s'\tau'} \right] &= \hat{a}_{\mathbf{p}-\mathbf{q},\lambda_1s\tau}^{\dagger} \hat{a}_{\mathbf{p}'+\mathbf{q},\lambda_2s\tau}^{\dagger} \hat{a}_{\mathbf{p}'\lambda_3s\tau} \\
&\quad \times \hat{a}_{\mathbf{p}\lambda_4s\tau} \hat{a}_{\mathbf{p}''\lambda's'\tau'}^{\dagger} \hat{a}_{\mathbf{p}''\lambda''s'\tau'} - \hat{a}_{\mathbf{p}''\lambda's'\tau'}^{\dagger} \hat{a}_{\mathbf{p}''\lambda''s'\tau'} \hat{a}_{\mathbf{p}-\mathbf{q},\lambda_1s\tau}^{\dagger} \hat{a}_{\mathbf{p}'+\mathbf{q},\lambda_2s\tau}^{\dagger} \hat{a}_{\mathbf{p}'\lambda_3s\tau} \hat{a}_{\mathbf{p}\lambda_4s\tau}. \quad (2.33)
\end{aligned}$$

Further manipulation and introducing the normal ordering ($::$), we write:

$$\begin{aligned}
&: \hat{a}_{\mathbf{p}-\mathbf{q},\lambda_1s\tau}^{\dagger} \hat{a}_{\mathbf{p}'+\mathbf{q},\lambda_2s\tau}^{\dagger} \hat{a}_{\mathbf{p}'\lambda_3s\tau} \hat{a}_{\mathbf{p}\lambda_4s\tau} \hat{a}_{\mathbf{p}''\lambda's'\tau'}^{\dagger} \hat{a}_{\mathbf{p}''\lambda''s'\tau'} : \\
&=: \hat{a}_{\mathbf{p}-\mathbf{q},\lambda_1s\tau}^{\dagger} \hat{a}_{\mathbf{p}'+\mathbf{q},\lambda_2s\tau}^{\dagger} \hat{a}_{\mathbf{p}'\lambda_3s\tau} \left(\{ \hat{a}_{\mathbf{p}\lambda_4s\tau} \hat{a}_{\mathbf{p}''\lambda's'\tau'}^{\dagger} \} - \hat{a}_{\mathbf{p}''\lambda's'\tau'}^{\dagger} \hat{a}_{\mathbf{p}\lambda_4s\tau} \right) \hat{a}_{\mathbf{p}''\lambda''s'\tau'} : \\
&=: \hat{a}_{\mathbf{p}-\mathbf{q},\lambda_1s\tau}^{\dagger} \hat{a}_{\mathbf{p}'+\mathbf{q},\lambda_2s\tau}^{\dagger} \hat{a}_{\mathbf{p}'\lambda_3s\tau} \hat{a}_{\mathbf{p}''\lambda's'\tau'} \delta_{\mathbf{p},\mathbf{p}''} \delta_{\lambda_4,\lambda'} \delta_{s,s'} \delta_{\tau,\tau'} - \hat{a}_{\mathbf{p}-\mathbf{q},\lambda_1s\tau}^{\dagger} \hat{a}_{\mathbf{p}'+\mathbf{q},\lambda_2s\tau}^{\dagger} \\
&\quad \times \hat{a}_{\mathbf{p}'\lambda_3s\tau} \hat{a}_{\mathbf{p}''\lambda's'\tau'}^{\dagger} \hat{a}_{\mathbf{p}\lambda_4s\tau} \hat{a}_{\mathbf{p}''\lambda''s'\tau'} : \\
&=: -\hat{a}_{\mathbf{p}-\mathbf{q},\lambda_1s\tau}^{\dagger} \hat{a}_{\mathbf{p}'+\mathbf{q},\lambda_2s\tau}^{\dagger} \{ \hat{a}_{\mathbf{p}'\lambda_3s\tau} \hat{a}_{\mathbf{p}''\lambda's'\tau'}^{\dagger} \} \hat{a}_{\mathbf{p}\lambda_4s\tau} \hat{a}_{\mathbf{p}''\lambda''s'\tau'} \\
&\quad + \hat{a}_{\mathbf{p}-\mathbf{q},\lambda_1s\tau}^{\dagger} \hat{a}_{\mathbf{p}'+\mathbf{q},\lambda_2s\tau}^{\dagger} \hat{a}_{\mathbf{p}''\lambda's'\tau'}^{\dagger} \hat{a}_{\mathbf{p}'\lambda_3s\tau} \hat{a}_{\mathbf{p}\lambda_4s\tau} \hat{a}_{\mathbf{p}''\lambda''s'\tau'} : = \\
&= \hat{a}_{\mathbf{p}-\mathbf{q},\lambda_1s\tau}^{\dagger} \hat{a}_{\mathbf{p}'+\mathbf{q},\lambda_2s\tau}^{\dagger} \hat{a}_{\mathbf{p}'\lambda_3s\tau} \hat{a}_{\mathbf{p}''\lambda's'\tau'} \delta_{\mathbf{p},\mathbf{p}''} \delta_{\lambda_4,\lambda'} \delta_{s,s'} \delta_{\tau,\tau'} - \hat{a}_{\mathbf{p}-\mathbf{q},\lambda_1s\tau}^{\dagger} \hat{a}_{\mathbf{p}'+\mathbf{q},\lambda_2s\tau}^{\dagger} \\
&\quad \times \hat{a}_{\mathbf{p}\lambda_4s\tau} \hat{a}_{\mathbf{p}''\lambda's'\tau'} \delta_{\mathbf{p}',\mathbf{p}''} \delta_{\lambda_3,\lambda'} \delta_{s,s'} \delta_{\tau,\tau'} + \hat{a}_{\mathbf{p}-\mathbf{q},\lambda_1s\tau}^{\dagger} \hat{a}_{\mathbf{p}'+\mathbf{q},\lambda_2s\tau}^{\dagger} \hat{a}_{\mathbf{p}''\lambda's'\tau'}^{\dagger} \hat{a}_{\mathbf{p}'\lambda_3s\tau} \hat{a}_{\mathbf{p}\lambda_4s\tau} \hat{a}_{\mathbf{p}''\lambda''s'\tau'} . \quad (2.34)
\end{aligned}$$

Following the same steps as above for the second term of the commutator of Eq. (2.33) one finally arrives to:

$$\begin{aligned}
& [\hat{a}_{\mathbf{p}-\mathbf{q},\lambda_1 s\tau}^\dagger \hat{a}_{\mathbf{p}'+\mathbf{q},\lambda_2 s\tau}^\dagger \hat{a}_{\mathbf{p}'\lambda_3 s\tau} \hat{a}_{\mathbf{p}\lambda_4 s\tau}, \hat{a}_{\mathbf{p}''\lambda'\tau'}^\dagger \hat{a}_{\mathbf{p}''\lambda''\tau'}] = \\
& = \hat{a}_{\mathbf{p}-\mathbf{q},\lambda_1 s\tau}^\dagger \hat{a}_{\mathbf{p}'+\mathbf{q},\lambda_2 s\tau}^\dagger \hat{a}_{\mathbf{p}'\lambda_3 s\tau} \hat{a}_{\mathbf{p}''\lambda''\tau'} \delta_{\mathbf{p},\mathbf{p}''} \delta_{\lambda_4,\lambda'} \delta_{s,s'} \delta_{\tau,\tau'} - \hat{a}_{\mathbf{p}-\mathbf{q},\lambda_1 s\tau}^\dagger \hat{a}_{\mathbf{p}'+\mathbf{q},\lambda_2 s\tau}^\dagger \times \\
& \quad \times \hat{a}_{\mathbf{p}\lambda_4 s\tau} \hat{a}_{\mathbf{p}''\lambda''\tau'} \delta_{\mathbf{p}',\mathbf{p}''} \delta_{\lambda_3,\lambda'} \delta_{s,s'} \delta_{\tau,\tau'} - \hat{a}_{\mathbf{p}''\lambda'\tau'}^\dagger \hat{a}_{\mathbf{p}'+\mathbf{q},\lambda_2 s\tau}^\dagger \hat{a}_{\mathbf{p}'\lambda_3 s\tau} \hat{a}_{\mathbf{p}\lambda_4 s\tau} \times \\
& \quad \times \delta_{\mathbf{p}'',\mathbf{p}-\mathbf{q}} \delta_{\lambda'',\lambda_1} \delta_{s',s} \delta_{\tau',\tau} + \hat{a}_{\mathbf{p}''\lambda'\tau'}^\dagger \hat{a}_{\mathbf{p}-\mathbf{q},\lambda_1 s\tau}^\dagger \hat{a}_{\mathbf{p}'\lambda_3 s\tau} \hat{a}_{\mathbf{p}\lambda_4 s\tau} \delta_{\mathbf{p}'',\mathbf{p}'+\mathbf{q}} \delta_{\lambda'',\lambda_2} \delta_{s',s} \delta_{\tau',\tau}, \quad (2.35)
\end{aligned}$$

and then, the interaction term contribution is,

$$\begin{aligned}
& \left[\hat{\mathcal{H}}_{ee}, \hat{\rho}_{\mathbf{p}'',\lambda',\lambda''}^{s'\tau'}(t) \right] = \frac{-e}{2A} \sum_{s,s',\tau,\tau',\{\lambda_i\}} \sum_{\mathbf{p},\mathbf{p}',\mathbf{q} \neq 0} V(q) \mathcal{F}_{\{\lambda_i\}}(\mathbf{p}, \mathbf{p}', \mathbf{q}) \\
& \quad \times (\hat{a}_{\mathbf{p}-\mathbf{q},\lambda_1 s\tau}^\dagger \hat{a}_{\mathbf{p}'+\mathbf{q},\lambda_2 s\tau}^\dagger \hat{a}_{\mathbf{p}'\lambda_3 s\tau} \hat{a}_{\mathbf{p}''\lambda''\tau'} \delta_{\mathbf{p},\mathbf{p}''} \delta_{\lambda_4,\lambda'} \delta_{s,s'} \delta_{\tau,\tau'} - \hat{a}_{\mathbf{p}-\mathbf{q},\lambda_1 s\tau}^\dagger \hat{a}_{\mathbf{p}'+\mathbf{q},\lambda_2 s\tau}^\dagger \\
& \quad \times \hat{a}_{\mathbf{p}\lambda_4 s\tau} \hat{a}_{\mathbf{p}''\lambda''\tau'} \delta_{\mathbf{p}',\mathbf{p}''} \delta_{\lambda_3,\lambda'} \delta_{s,s'} \delta_{\tau,\tau'} - \hat{a}_{\mathbf{p}''\lambda'\tau'}^\dagger \hat{a}_{\mathbf{p}'+\mathbf{q},\lambda_2 s\tau}^\dagger \hat{a}_{\mathbf{p}'\lambda_3 s\tau} \hat{a}_{\mathbf{p}\lambda_4 s\tau} \\
& \quad \times \delta_{\mathbf{p}'',\mathbf{p}-\mathbf{q}} \delta_{\lambda'',\lambda_1} \delta_{s',s} \delta_{\tau',\tau} + \hat{a}_{\mathbf{p}''\lambda'\tau'}^\dagger \hat{a}_{\mathbf{p}-\mathbf{q},\lambda_1 s\tau}^\dagger \hat{a}_{\mathbf{p}'\lambda_3 s\tau} \hat{a}_{\mathbf{p}\lambda_4 s\tau} \delta_{\mathbf{p}'',\mathbf{p}'+\mathbf{q}} \delta_{\lambda'',\lambda_2} \delta_{s',s} \delta_{\tau',\tau}). \quad (2.36)
\end{aligned}$$

The last term is the contribution from the external electrical field coupling to the Heisenberg equation of motion of the density:

$$\left[\hat{\mathcal{H}}_I, \hat{\rho}_{\mathbf{p}',\lambda,\lambda'}^{s'\tau'} \right] = -e\mathcal{E}(t) \sum_{\mathbf{p}^{s\tau},\lambda_1} \frac{i\nu_{\mathbf{p},\lambda_1}^{s,\tau}}{2\lambda_1 E_{\mathbf{p}}^{s,\tau}} \left[\hat{\rho}_{\mathbf{p},\lambda_1,-\lambda_1}^{s\tau}, \hat{\rho}_{\mathbf{p}',\lambda,\lambda'}^{s'\tau'} \right], \quad (2.37)$$

this commutator is similar to the one elaborated for the free-particle Hamiltonian commutator, thus we write that:

$$\left[\hat{\rho}_{\mathbf{p},\lambda_1,-\lambda_1}^{s\tau}, \hat{\rho}_{\mathbf{p}',\lambda,\lambda'}^{s'\tau'} \right] = \hat{\rho}_{\mathbf{p},\lambda_1,\lambda'}^{s\tau} \delta_{-\lambda_1,\lambda} + \hat{\rho}_{\mathbf{p},\lambda',-\lambda_1}^{s\tau} \delta_{\lambda_1,\lambda'}, \quad (2.38)$$

giving the following expression:

$$\left[\hat{\mathcal{H}}_I, \hat{\rho}_{\mathbf{p},\lambda,\lambda'}^{s\tau} \right] = e\mathcal{E}(t) \left(\frac{i\nu_{\mathbf{p},-\lambda}^{s,\tau}}{2\lambda E_{\mathbf{p}}^{s,\tau}} \hat{\rho}_{\mathbf{p},-\lambda,\lambda'}^{s\tau} + \frac{i\nu_{\mathbf{p},\lambda'}^{s,\tau}}{2\lambda_1 E_{\mathbf{p}}^{s,\tau}} \hat{\rho}_{\mathbf{p},\lambda,-\lambda'}^{s\tau} \right). \quad (2.39)$$

Next, one has to calculate the expectation value of each term. Her note that there are two distinct equations, for $\lambda = \lambda'$ in the Heisenberg equation yields the time evolution of the intraband density, and for $\lambda \neq \lambda'$, the interband transitions.

Let us compute the expectation value of each term in detail, then we can access the physical interpretation of the contribution of each commutator to the transitions due to the coupling to the external field. First, the non-interacting term is given by:

$$\left\langle \left[\hat{\mathcal{H}}_{0,i}, \hat{\rho}_{\mathbf{p}',\lambda',\lambda''}^{s\tau} \right] \right\rangle = (\lambda' - \lambda'') E_{\mathbf{p}}^{s,\tau} \langle \hat{\rho}_{\mathbf{p},\lambda',\lambda''}^{s\tau} \rangle. \quad (2.40)$$

The expectation value of the above commutator for $\lambda' = \lambda''$ is 0, which is expected since for intraband transitions the commutator of the free carrier with the density operator should naturally commute. Now, for $\lambda' \neq \lambda''$, we have the interband transition, since $\lambda' = -\lambda'' \equiv \lambda$,

$$\langle [\hat{\mathcal{H}}_{0,i}, \hat{\rho}_{\mathbf{p}',\lambda,-\lambda}^{s\tau}] \rangle = 2\lambda E_{\mathbf{p}}^{s,\tau} \mathcal{P}_{\mathbf{p}\lambda}^{s\tau}, \quad (2.41)$$

where,

$$\mathcal{P}_{\mathbf{p}\lambda}^{s\tau} = \langle \hat{\rho}_{\mathbf{p},\lambda,-\lambda}^{s\tau} \rangle. \quad (2.42)$$

Now we move forward to the commutator carrying the interaction with the external field,

$$\langle [\hat{\mathcal{H}}_I, \hat{\rho}_{\mathbf{p},\lambda,\lambda'}^{s\tau}] \rangle = e\mathcal{E}(t) \left(\frac{i\nu_{\mathbf{p},-\lambda}^{s,\tau}}{2\lambda E_{\mathbf{p}}^{s,\tau}} \langle \hat{\rho}_{\mathbf{p},-\lambda,\lambda'}^{s\tau} \rangle + \frac{i\nu_{\mathbf{p},\lambda'}^{s,\tau}}{2\lambda' E_{\mathbf{p}}^{s,\tau}} \langle \hat{\rho}_{\mathbf{p},\lambda,-\lambda'}^{s\tau} \rangle \right), \quad (2.43)$$

once again, we consider two kinds of transitions, intraband for $\lambda = \lambda'$,

$$\langle [\hat{\mathcal{H}}_I, \hat{\rho}_{\mathbf{p},\lambda,\lambda}^{s\tau}] \rangle = e\mathcal{E}(t) \frac{\mathcal{I} [i\nu_{\mathbf{p},\lambda}^{s,\tau} \mathcal{P}_{\mathbf{p}\lambda}^{s\tau}(t)]}{\lambda E_{\mathbf{p}}^{s,\tau}}, \quad (2.44)$$

and for interband with $\lambda \neq \lambda'$, we have,

$$\langle [\hat{\mathcal{H}}_I, \hat{\rho}_{\mathbf{p},\lambda,-\lambda}^{s\tau}] \rangle = e\mathcal{E}(t) \left(\frac{i\nu_{\mathbf{p},-\lambda}^{s,\tau}}{2\lambda E_{\mathbf{p}}^{s,\tau}} \langle \hat{\rho}_{\mathbf{p},-\lambda,-\lambda}^{s\tau} \rangle - \frac{i\nu_{\mathbf{p},\lambda'}^{s,\tau}}{2\lambda' E_{\mathbf{p}}^{s,\tau}} \langle \hat{\rho}_{\mathbf{p},\lambda,\lambda}^{s\tau} \rangle \right), \quad (2.45)$$

which we can write as,

$$\langle [\hat{\mathcal{H}}_I, \hat{\rho}_{\mathbf{p},\lambda,-\lambda}^{s\tau}] \rangle = e\mathcal{E}(t) \frac{i\nu_{\mathbf{p},-\lambda}^{s,\tau}}{2\lambda E_{\mathbf{p}}^{s,\tau}} (\mathcal{N}_{\mathbf{p}-\lambda}^{s,\tau} - \mathcal{N}_{\mathbf{p}\lambda}^{s,\tau}), \quad (2.46)$$

where,

$$\mathcal{N}_{\mathbf{p}\lambda}^{s,\tau} = \langle \hat{\rho}_{\mathbf{p},\lambda,\lambda}^{s\tau} \rangle, \quad (2.47)$$

is the expectation value of the electronic density.

2.3 Truncation of the Equations of Motion

In order to treat the contribution from the electron-electron interaction to the equation of motion, one must be careful. It can be directly seen from Eq. (2.36) that the dynamics of the density operator, which is a two-particle operator, is coupled to four-particle operators. This is due to the underlying hierarchy that arises from the Coulomb

interaction. In general, a $(N+1)$ -body operator dynamics is coupled to a $(N+2)$ -body operator, which implies a necessity for a decoupling scheme. Here, we will consider the Cluster-Expansion approach in which one constructs a N -body quantity (which we will denote by $\langle N \rangle$) in terms of a factorization of its correlation, that is, the single-particle (singlet), the correlated pair (doublet), the three-particle cluster (triplet) up to the N particle cluster, leading to a recursive reconstruction of the hierarchical organization of interacting particles (HAUG; KOCH, 2004). Symbolically we can write,

$$\langle 2 \rangle = \langle 2 \rangle_S + \Delta \langle 2 \rangle \quad (2.48)$$

$$\langle 3 \rangle = \langle 3 \rangle_S + \langle 1 \rangle \Delta \langle 2 \rangle + \Delta \langle 3 \rangle \quad (2.49)$$

⋮

$$\langle N \rangle = \langle N \rangle_S + \langle N - 2 \rangle_S \Delta \langle 2 \rangle + \langle N - 4 \rangle_S \Delta \langle 2 \rangle \Delta \langle 2 \rangle \cdots + \Delta \langle N \rangle, \quad (2.50)$$

where the subscript S denotes singlets and the $\Delta \langle K \rangle$ is the K -particle correlation.

An example of the cluster factorization is the Hartree-Fock decomposition, obtained from

$$\langle \hat{a}_1^\dagger \hat{a}_2^\dagger \hat{a}_3 \hat{a}_4 \rangle = \langle \hat{a}_1^\dagger \hat{a}_4 \rangle \langle \hat{a}_2^\dagger \hat{a}_3 \rangle - \langle \hat{a}_1^\dagger \hat{a}_3 \rangle \langle \hat{a}_2^\dagger \hat{a}_4 \rangle + \Delta \langle \hat{a}_1^\dagger \hat{a}_2^\dagger \hat{a}_3 \hat{a}_4 \rangle, \quad (2.51)$$

when the higher correlations are disregarded, arriving to the Hartree-Fock mean-field approximation:

$$\langle \hat{a}_1^\dagger \hat{a}_2^\dagger \hat{a}_3 \hat{a}_4 \rangle \approx \langle \hat{a}_1^\dagger \hat{a}_4 \rangle \langle \hat{a}_2^\dagger \hat{a}_3 \rangle - \langle \hat{a}_1^\dagger \hat{a}_3 \rangle \langle \hat{a}_2^\dagger \hat{a}_4 \rangle. \quad (2.52)$$

In our case, this decomposition corresponds to evaluate the four-body expectation values as products of inter-band transition probabilities $\mathcal{P}_{\mathbf{p}\lambda}^{s,\tau}$ (for $\lambda \neq \lambda'$) and the electronic distribution $\mathcal{N}_{\mathbf{p}\lambda}^{s,\tau}$ (for $\lambda = \lambda'$). By momentum conservation, a generic two-body expectation value is written as,

$$\langle a_{\mathbf{k},\lambda,s,\tau}^\dagger a_{\mathbf{k}',\lambda',s,\tau} \rangle = \rho_{\mathbf{k},\lambda,\lambda'}^{s,\tau} \delta_{\mathbf{k},\mathbf{k}'}, \quad (2.53)$$

and if we apply the above mentioned decomposition to the expectation value of Eq. (2.36), invoke the parity symmetry in momentum space and relabel indices, we can write down the interaction term as,

$$\begin{aligned} \langle [\mathcal{H}_{ee}, \rho_{\mathbf{p}''}^{s',\tau'}] \rangle &= -\frac{e}{2A} \sum_{\lambda_1, \lambda_2, \lambda_3} \sum_{\mathbf{q} \neq 0} V(\mathbf{q}) \rho_{\mathbf{p}'' - \mathbf{q}, \lambda_2, \lambda_3}^{s\tau} \left(\mathcal{F}_{\lambda', \lambda_3, \lambda_1, \lambda_2}(\mathbf{p}'' - \mathbf{q}, \mathbf{p}'', \mathbf{q}) \rho_{\mathbf{p}'' \lambda_1, \lambda''}^{s,\tau} \right. \\ &\quad \left. - \mathcal{F}_{\lambda_2, \lambda_3 \lambda_1, \lambda''}(\mathbf{p}'', \mathbf{p}'' - \mathbf{q}, \mathbf{q}) \rho_{\mathbf{p}'' \lambda', \lambda_1}^{s\tau} \right). \quad (2.54) \end{aligned}$$

Finally, if we add to the above commutator for $\lambda' \neq \lambda''$ the commutators given in Eqs. (2.46) and (2.41), we get that:

$$\begin{aligned} -i\hbar \frac{\partial \mathcal{P}_{\mathbf{p},\lambda}^{s,\tau}}{\partial t} &= (2\lambda E_{\mathbf{p}}^{s,\tau} + \lambda \Sigma_{\mathbf{p},\lambda}^{s,\tau} + \mathcal{W}_{\mathbf{p},\lambda}^{s,\tau}) \mathcal{P}_{\mathbf{p},\lambda}^{s,\tau} \\ &+ \left(-e\mathcal{E}(t) \frac{i\nu_{\mathbf{p},-\lambda}^{s,\tau}}{2\lambda E_{\mathbf{p}}^{s,\tau}} + \mathcal{B}_{\mathbf{p},\lambda}^{s,\tau} + \mathcal{D}_{\mathbf{p},\lambda}^{s,\tau} \right) (\mathcal{N}_{\mathbf{p},\lambda}^{s,\tau} - \mathcal{N}_{\mathbf{p}-\lambda}^{s,\tau}) \end{aligned} \quad (2.55)$$

on the other hand, if we sum Eq. (2.54) for $\lambda = \lambda' = \lambda''$ and Eq. (2.44), we find that:

$$-\hbar \frac{\partial \mathcal{N}_{\mathbf{p},\lambda}^{s,\tau}}{\partial t} = 2\mathcal{I} \left[\left(-e\mathcal{E}(t) \frac{i\nu_{\mathbf{p},-\lambda}^{s,\tau}}{2\lambda E_{\mathbf{p}}^{s,\tau}} + \mathcal{B}_{\mathbf{p},\lambda}^{s,\tau} + \mathcal{D}_{\mathbf{p},\lambda}^{s,\tau} \right) \mathcal{P}_{\mathbf{p},\lambda}^{s,\tau} \right], \quad (2.56)$$

where the terms in the equations are given by:

$$2\lambda E_{\mathbf{p}}^{s,\tau} = 2\lambda \sqrt{(\hbar v_{f,i} p)^2 + (\Delta_{s,\tau}^0)^2}, \quad (2.57)$$

$$\Sigma_{\mathbf{p},\lambda}^{s,\tau} = \frac{\lambda e}{A} \sum_{\mathbf{q}} V(q) \left(\mathcal{N}_{(\mathbf{p}-\mathbf{q})\lambda}^{s,\tau} - \mathcal{N}_{(\mathbf{p}-\mathbf{q})-\lambda}^{s,\tau} \right) \left(F_{-\lambda\lambda\lambda-\lambda}^{s,\tau}(\mathbf{p}, \mathbf{p}-\mathbf{q}) - F_{\lambda\lambda\lambda\lambda}^{s,\tau}(\mathbf{p}, \mathbf{p}-\mathbf{q}) \right), \quad (2.58)$$

$$\mathcal{W}_{\mathbf{p},\lambda}^{s,\tau} = \frac{e}{A} \sum_{\mathbf{q},\lambda'} V(|\mathbf{p}-\mathbf{q}|) \mathcal{P}_{\mathbf{q},\lambda'}^{s,\tau} \left(F_{-\lambda-\lambda'\lambda'-\lambda}^{s,\tau}(\mathbf{p}, \mathbf{q}) - F_{\lambda-\lambda'\lambda'\lambda}^{s,\tau}(\mathbf{p}, \mathbf{q}) \right), \quad (2.59)$$

$$\Omega_{\mathbf{p},\lambda}^{s,\tau} = -e\mathcal{E}(t) \frac{i\nu_{\mathbf{p},-\lambda}^{s,\tau}}{2\lambda E_{\mathbf{p}}^{s,\tau}} + \mathcal{B}_{\mathbf{p},\lambda}^{s,\tau}, \quad (2.60)$$

$$\mathcal{B}_{\mathbf{p},\lambda}^{s,\tau} = \frac{e}{A} \sum_{\mathbf{q}} V(|\mathbf{p}-\mathbf{q}|) \left(\mathcal{P}_{\mathbf{q},\lambda}^{s,\tau} F_{-\lambda-\lambda\lambda\lambda}^{s,\tau}(\mathbf{p}, \mathbf{q}) + \mathcal{P}_{\mathbf{q},-\lambda}^{s,\tau} F_{-\lambda\lambda-\lambda\lambda}^{s,\tau}(\mathbf{p}, \mathbf{q}) \right) \quad (2.61)$$

$$\mathcal{D}_{\mathbf{p},\lambda}^{s,\tau} = \frac{e}{A} \sum_{\mathbf{q},\lambda'} V(q) \mathcal{N}_{\mathbf{p}-\mathbf{q},\lambda'}^{s,\tau} F_{-\lambda\lambda'\lambda'\lambda}^{s,\tau}(\mathbf{p}, \mathbf{p}-\mathbf{q}). \quad (2.62)$$

Although not explicitly written, all terms in Eqs. (2.55) and (2.56) are time-dependent. In the next section, we will give a description and discuss each term that provides the dynamical content of Eqs. (2.55) and (2.56) in physical terms.

2.4 Interpretation of the Dynamics

Having derived Eqs. (2.55) and (2.56), which are our main motivation to explore few-body correlations in condensed matter physics, let us discuss the physical significance of each term defining the dynamical content of the truncated equations of motion.

First, consider Eq. (2.55) for the inter-band transition probability $\mathcal{P}_{\mathbf{p},\lambda}^{s,\tau}$. In the right hand side of Eq. (2.55) there is a term that accompanies the transition probability (first line of Eq. (2.55)) and a other term that couples its evolution with the band occupation

density (second line of Eq. (2.55)). Let us focus on the term that accompanies the transition probability. $2\lambda E_{\mathbf{p}}^{s\tau}$, Eq. (2.57), is the transition energy of the two-band system and $\Sigma_{\mathbf{p},\lambda}^{s,\tau}$, Eq. (2.58), gives a correction to such transition energy by considering the effects of the media, which arises from the truncated hierarchy of interacting carriers, that is, a renormalization of the transition energy. The third term of Eq. (2.55), given by $\mathcal{W}_{\mathbf{p},\lambda}^{s,\tau}$, Eq. (2.59), breaks linearity by making the evolution of the transition probability proportional to a quadratic term containing the product of transition probabilities $\mathcal{P}_{\mathbf{q}\lambda'}^{s,\tau} \mathcal{P}_{\mathbf{p}\lambda}^{s\tau}$.

The second part of Eq. (2.55) tells us how the field mediates the coupling of the transition probabilities and the net band occupation density through the following quantities: $\Omega_{\mathbf{p},\lambda}^{s,\tau}$, Eq. (2.60), has a term that governs the time-evolution of the fluctuation of the population density due to the external light pulse, which is called the Rabi Frequency. If we make $V(q) \rightarrow 0$, we will have a common result from the two-level system which is that the fluctuation of the population density is proportional to the dipole operator (which in this case governs the velocity of the transitions, so it is common to call it the velocity operator) multiplied by the external field. When the interaction is turned on, the formation of electron-hole pairs induces a renormalization to the Rabi Frequency which is accounted by $\mathcal{B}_{\mathbf{p},\lambda}^{s,\tau}$, given by Eq. (2.61). Finally, $\mathcal{D}_{\mathbf{p},\lambda}^{s,\tau}$, Eq. (2.62), introduces a non-linear contribution to the density, which accounts for the fluctuation in density induced by the formation of excitons.

The central idea of these last calculations is that the interacting system formed by the electron gas in two-band approximation subjected to an external electromagnetic field leads to the formation of correlated pairs, which affects the optical properties, governed by the transition probability and the occupation density. Therefore, studying these correlated pairs of electron and holes (excitons) gives us a better understanding of the underlying structure of optical properties of the material. Before we move forward with the derivation of the equations that govern the formation of excitons and the polarization of the system, we need to deepen our discussion on the density equation.

When we have a interacting quantum many-body system subjected to a external perturbation, we push the system out of equilibrium, and depending on the intensity of the external perturbation, one can drive the system into a phase transition. Since we are concerned with properties described in thermodynamic equilibrium, we can consider an equilibrium distribution for the system. In the particular case where the non-linearity in the density is neglected, it becomes the Fermi-Dirac distribution,

$$\mathcal{N}_{\mathbf{p},\lambda}^{s,\tau} = \frac{1}{1 + e^{\beta(\lambda E_{\mathbf{p}}^{s,\tau} - E_F)}}. \quad (2.63)$$

2.5 The Wannier Equation

Having derived the equations of motion for the transition probabilities (and therefore, the polarization operator) we are ready to study the excitonic states. Starting with the equation that governs the transition probabilities, (2.55), neglecting the nonlinear terms, considering zero temperature in which all electrons occupy the valence band, we have a charge neutrality which reads $(\mathcal{N}_{\mathbf{p}\lambda}^{s,\tau} - \mathcal{N}_{\mathbf{p}-\lambda}^{s,\tau}) = -1$, so we write that:

$$\left(i\hbar \frac{\partial}{\partial t} + 2\lambda E_p^{s\tau} + \lambda \Sigma_{\mathbf{p},\lambda}^{s\tau} \right) \mathcal{P}_{\mathbf{p},\lambda}^{s,\tau} = \left(-e\mathcal{E}(t) \frac{i\mathcal{W}_{\mathbf{p},-\lambda}^{s,\tau}}{2\lambda E_{\mathbf{p}}^{s,\tau}} + \mathcal{B}_{\mathbf{p},\lambda}^{s,\tau} \right), \quad (2.64)$$

where we also consider that in the linear regime (where we can neglect the non-linear effects in both the density and transition probabilities), the electric field is a harmonic field with constant amplitude and the linear response of the system to this field (encapsulated by the transition probability) should also be harmonic,

$$\mathcal{E}(t) = \mathcal{E}_0 e^{i\omega t} \quad (2.65)$$

$$\mathcal{P}_{\mathbf{p},\lambda}^{s,\tau}(t) = \mathcal{P}_{\mathbf{p},\lambda}^{s,\tau}(\omega) e^{i\omega t}. \quad (2.66)$$

Taking the harmonic mode, we can write Eq. (2.64) in the time-independent form,

$$(\hbar\omega - (2\lambda E_p^{s\tau} + \lambda \Sigma_{\mathbf{p},\lambda}^{s\tau})) \mathcal{P}_{\mathbf{p},\lambda}^{s,\tau}(\omega) = \left(e\mathcal{E}_0 \frac{\nu_{\mathbf{p},-\lambda}^{s,\tau}}{2i\lambda E_{\mathbf{p}}^{s,\tau}} + \mathcal{B}_{\mathbf{p},\lambda}^{s,\tau}(\omega) \right), \quad (2.67)$$

which is an integral equation for the transition probability of the system in the linear regime subjected to an external field. The solution of the time independent equation yields the frequency mode of the polarization operator and consequently the optical conductivity and absorbance coefficient.

The other equation that we can also solve is the homogeneous one, which is equivalent to consider only resonant terms in Eq. (2.67):

$$(\hbar\omega - (2E_p^{s\tau} + \Sigma_{\mathbf{p},+}^{s\tau})) \mathcal{P}_{\mathbf{p},+}^{s,\tau}(\omega) = \frac{e}{A} \sum_q V(|\mathbf{p} - \mathbf{q}|) \mathcal{F}_{--++}^{s,\tau}(\mathbf{p}, \mathbf{q}) \mathcal{P}_{\mathbf{q},+}^{s,\tau}(\omega), \quad (2.68)$$

which is an eigenvalue equation that can be put into a more familiar form by considering a partial-wave expansion of the transition probability,

$$\mathcal{P}_{\mathbf{k},+}^{s,\tau}(\omega) = \sum_{n,\ell} \psi_{n,\ell}^{s,\tau}(k) e^{i\ell\theta}, \quad (2.69)$$

where ℓ is the angular momentum and n is the principal quantum number, $\psi_{n,\ell}^{s,\tau}(k)$ is the bound-state wave-function of an electron and a hole. By taking the continuum limit of

the homogeneous equation, (2.68), we arrive at (while also by renaming the kernel),

$$(\hbar\omega - (2E_p^{s\tau} + \Sigma_{\mathbf{p},+}^{s\tau})) \sum_{n,\ell} \psi_{n,\ell}^{s,\tau}(p) e^{i\ell\theta} = \sum_{n,\ell} \int \frac{d\mathbf{q}}{4\pi^2} K(\mathbf{p}, \mathbf{q}) \psi_{n,\ell}^{s,\tau}(q) e^{i\ell\theta}, \quad (2.70)$$

which is known as the Bethe-Salpeter Equation for the exciton, can be simplified using the orthogonality of the partial-wave expansion:

$$(E - \mathcal{E}_{\mathbf{p}}^{s,\tau}) \psi_{n,\ell}^{s,\tau}(p) = \int_0^\infty \frac{dq}{(2\pi)} \mathcal{K}_\ell^{s,\tau}(p, q) \psi_{n,\ell}^{s,\tau}(q), \quad (2.71)$$

where $\mathcal{E}_{\mathbf{p}}^{s,\tau}$ is the renormalized transition energy $\mathcal{E}_{\mathbf{p}}^{s,\tau} = 2E_p^{s\tau} + \Sigma_{\mathbf{p},+}^{s\tau}$ and E is the exciton energy and $\mathcal{K}_\ell^{s,\tau}(p, q)$ is the decomposed kernel,

$$\mathcal{K}_\ell^{s,\tau}(p, q) = \int \frac{d\theta}{2\pi} e^{i\ell\theta} K(\mathbf{p}, \mathbf{q}). \quad (2.72)$$

As we can see from the theoretical development, given a Hamiltonian that governs the carrier dynamics, we have a particular kernel due to the different form factors entering in $K(\mathbf{p}, \mathbf{q})$ that arise from the diagonalization of the free Hamiltonian, Eq. (2.1). In this case, the form factors come from the spinor solutions of the gapped Dirac equation.

Now, we will introduce approximations that leads to the celebrated Wannier equation, which is the focal point of this work. First, we approximate the transition energy as parabolic near the minimum, governed by an effective electron-hole reduced mass,

$$\mathcal{E}_{\mathbf{p}}^{s,\tau} \approx E_g + \frac{\hbar^2 p^2}{2\mu}, \quad (2.73)$$

where μ is the effective mass and E_g is the band gap of the system. For a parabolic dispersion relation, the structure factors (2.12) are reduced to unity and the quantity $E - E_g$ is the binding energy E_b of the exciton, therefore, the equation is,

$$E_b \psi_{n,\ell}^{s,\tau}(p) = \frac{\hbar^2 p^2}{2\mu} \psi_{n,\ell}^{s,\tau}(p) + \int_0^\infty \frac{dq}{(2\pi)} \mathcal{K}_\ell^{s,\tau}(p, q) \psi_{n,\ell}^{s,\tau}(q). \quad (2.74)$$

This is the Wannier equation for the binding energy and wave-function of the exciton in 2D. Both equations (2.71) and (2.74) can be used to calculate useful response functions, using Elliot's Formula, and express the details of the two-body bound state (CHAVES *et al.*, 2017). There are simpler constructions of the physical description of the exciton, treating the problem as a problem analogous to the hydrogen atom (YU; CARDONA, 2010) but one of the objectives of this chapter is to present the emerging few-body correlations from the many-body theory, reinforcing the interface with few-body physics, which at a first glance seems far apart.

3 Numerical Analysis of the Wannier Equation

As we saw in the last chapter, the equation governing the electron-hole bound state in momentum space is an integral equation. In general, given a differential equation, there are different ways to find an associated integral equation, such as using Fourier Transform or Green's functions methods.

In simple terms, an integral equation is a form of equation such that undetermined function appears under the integral (MASUJIMA, 2009). There are several types of integral equations, here we will focus on Fredholm type equations, such as,

$$\phi(x) = f(x) + \lambda \int_a^b \mathcal{K}(x, y)\phi(y)dy, \quad (3.1)$$

where $x \in [a, b]$. This is called a Fredholm equation of the second kind, while,

$$f(x) = \int_a^b \mathcal{K}(x, y)\phi(y)dy, \quad (3.2)$$

is of the first kind. The function \mathcal{K} is the *Kernel* of the integral equation, $\phi(x)$ is the function to be determined. We call the equation *homogeneous* if $f(x) = 0$, otherwise it is said to be *inhomogeneous*.

In our particular case, we have the Wannier equation,

$$E_{\mathbf{p}}\psi(\mathbf{p}) + \int \frac{d^2\mathbf{p}'}{(2\pi)^2} V(\mathbf{p} - \mathbf{p}')\psi(\mathbf{p}') = E\psi(\mathbf{p}), \quad (3.3)$$

which is an homogeneous Fredholm equation of the second kind. This is easier to see by recasting it in the following form,

$$\psi(\mathbf{p}) = \lambda \int \frac{d^2\mathbf{p}'}{(2\pi)^2} \frac{V(\mathbf{p} - \mathbf{p}')}{E - E_{\mathbf{p}'}} \psi(\mathbf{p}') = \lambda \int d\mathbf{p}' \mathcal{K}(\mathbf{p}, \mathbf{p}')\psi(\mathbf{p}'). \quad (3.4)$$

3.1 Partial-Wave Decomposition Approach

Integral equations are usually computationally demanding to solve and there are different schemes in order to reduce such difficulties.

Considering we are dealing with two particles interacting via a central potential, we can introduce the following partial-wave expansion for the potential and the wave function as a way to explore the symmetry of our problem(ADHIKARI, 1986),

$$V(\mathbf{p}, \mathbf{p}') = \sum_{\ell} \mathcal{V}_{\ell}(p, p') \cos(\ell\theta') \iff \mathcal{V}_{\ell}(p, p') = \frac{1}{2\pi} \int_0^{2\pi} \cos(\ell\theta') V(\mathbf{p}, \mathbf{p}') \quad (3.5)$$

$$\psi(\mathbf{p}) = \sum_{\ell} \phi_{\ell}(p) \cos(\ell\theta), \quad (3.6)$$

one can also notice that we are considering $\mathbf{p} \parallel x$ axis, therefore, θ' is the angle between \mathbf{p}' and \mathbf{p} . Substituting the expansion back into 3.3, we arrive at,

$$E_{\mathbf{p}} \sum_{\ell} \phi_{\ell}(p) \cos(\ell\theta) + \sum_{\ell', \ell''} \int \frac{d^2\mathbf{p}'}{(2\pi)^2} \mathcal{V}_{\ell''}(p, p') \cos(\ell''\theta') \phi'_{\ell}(p') \cos(\ell'\theta') = E \sum_{\ell} \phi_{\ell}(p) \cos(\ell\theta) \quad (3.7)$$

using the orthogonality of the cosine function, the angle variable in second term can be analytically integrated out, yielding,

$$E_{\mathbf{p}} \sum_{\ell} \phi_{\ell}(p) \cos(\ell\theta) + \sum_{\ell', \ell''} \int \frac{d^2\mathbf{p}'}{(2\pi)^2} \mathcal{V}_{\ell''}(p, p') \phi'_{\ell}(p') (2\pi) \delta_{\ell', \ell''} = E \sum_{\ell} \phi_{\ell}(p) \cos(\ell\theta), \quad (3.8)$$

we can multiply both sides by $\cos(\ell'\theta)/2\pi$ and integrate, arriving at,

$$E_{\mathbf{p}} \phi_{\ell}(p) + \frac{1}{(2\pi)} \int_0^{\infty} dp' p' \mathcal{V}_{\ell}(p, p') \phi_{\ell}(p') = E \phi_{\ell}(p). \quad (3.9)$$

Now, we are handling a much simpler problem, with only one dimension. There are multiple avenues to tackle this equation, and here, we will employ two different approaches, the first one being the Chebyshev-Chawla-Kumar(GOLBERG, 2013) method, which consists of a finite decomposition of the kernel and a infinite decomposition of the wave function in terms of the Chebyshev polynomials, the second one being a direct solution by a Gauss-Legendre quadrature(STOER; BULIRSCH, 1980).

3.1.1 Chebyshev-Chawla-Kumar Method

3.1.1.1 Revision of Chebyshev Polynomials

First let us introduce the Chebyshev Polynomials as an Sturm-Liouville problem. We call the following a Sturm-Liouville boundary value problem(MASUJIMA, 2009). Given an ordinary differential equation defined on a interval $a \leq x \leq b$ with the generic form,

$$\frac{d}{dx} \left(p(x) \frac{dy}{dx} \right) + (q(x) + \lambda r(x)) y(x) = 0, \quad (3.10)$$

and boundary conditions as,

$$\begin{cases} a_1 y(a) + a_2 y'(a) = 0 \\ b_1 y(b) + b_2 y'(b) = 0 \end{cases}, \quad (3.11)$$

with $p(x) > 0$, $q(x)$ and a weight function $r(x) > 0$ as given functions, a_1, a_2, b_1 and b_2 are real numbers, while λ is an undetermined parameter.

There are several important differential equations that satisfy these conditions, such as Bessel, Hermite and Laguerre equations(COURANT; HILBERT, 1989). Here we present the Chebyshev Polynomial as a solution for the following form of the Sturm-Liouville problem. Set $a = -1$ and $b = 1$. Let $p(x) = \sqrt{1-x^2}$, $q(x) = 0$ and $r(x) = \sqrt{1-x^2}^{-1}$ with the characteristic value as $\lambda = n^2$, that is,

$$\frac{d}{dx} \left(\sqrt{1-x^2} \frac{dy}{dx} \right) + \frac{n^2}{\sqrt{1-x^2}} y(x) = 0, \quad (3.12)$$

which is the Chebyshev differential equation. The functions,

$$T_n(x) = \cos(n \arccos x), \quad (3.13)$$

for $n \in \mathbb{N}$, are called the Chebyshev polynomials of the first kind and one of the solutions of the Chebyshev differential equation. A few of the nice properties of this polynomial set is that, one can derive the following recursive relations,

$$T_0(x) = 1 \quad (3.14)$$

$$T_1(x) = x \quad (3.15)$$

$$T_{n+1}(x) = 2xT_n(x) - T_{n-1}(x) \quad (3.16)$$

$$T_m(x)T_n(x) = \frac{1}{2} (T_{m+n}(x) + T_{|m-n|}), \quad (3.17)$$

by substituting $x = \cos(\theta)$ and using trigonometric relations for the sum and product of

angles. Also, they form a orthogonal set under the following weighted inner product,

$$\int_{-1}^1 dx \frac{T_n(x)T_m(x)}{\sqrt{1-x^2}} = \begin{cases} 0, & m \neq n \\ \pi, & m = n = 0 \\ \frac{\pi}{2}, & m = n = 1, 2, 3, \dots \end{cases} \quad (3.18)$$

3.1.1.2 Solution method

With the properties of Chebychev polynomials in mind, we will now develop the Chebychev-Chawla-Kumar method. Let us return to Eq. (3.9). The first step is to introduce a conformal map, taking the half-line to the unity interval,

$$u = \frac{\xi p - 1}{\xi p + 1}, \quad (3.19)$$

where ξ is a scaling parameter and $u \in [-1, 1]$. By calculating the Jacobian for the change of coordinates and substituting into the partial-wave Wannier equation (3.9),

$$E_{\mathbf{u}}\phi_{\ell}(u) + \frac{1}{\xi^2\pi} \int_{-1}^1 \frac{du' (1+u') \mathcal{V}_{\ell}(u, u') \phi_{\ell}(u')}{(1-u')^3} = E\phi_{\ell}(u). \quad (3.20)$$

Now we expand the wave function in terms of the Chebyshev Polynomials,

$$\phi_{\ell}(u) = f(u) \sum_n^N c_{n,\ell} T_n(u), \quad (3.21)$$

substituting in (3.20) yields,

$$\begin{aligned} E_{\mathbf{u}}f(u) \sum_n^N c_{n,\ell} T_n(u) + \frac{1}{\xi^2\pi} \sum_n^N c_{n,\ell} \int_{-1}^1 \frac{du' (1+u') \mathcal{V}_{\ell}(u, u') f(u') T_n(u') (u-u')}{(1-u')^3 (u-u')} = \\ = E_{\mathbf{u}}f(u) \sum_n^N c_{n,\ell} T_n(u) + \frac{1}{\xi^2} \sum_n^N c_{n,\ell} \int_{-1}^1 \frac{du' \mathcal{K}_{\ell}(u, u') T_n(u')}{u-u'} = Ef(u) \sum_n^N c_{n,\ell} T_n(u), \end{aligned} \quad (3.22)$$

where we introduced the kernel,

$$\mathcal{K}_{\ell}(u, u') = \frac{(1+u') \mathcal{V}_{\ell}(u, u') f(u') (u-u')}{(1-u')^3}. \quad (3.23)$$

By doing the preceding scheme, we have shown that the initial Fredholm problem can be converted into a Cauchy singular integral equation problem (GOLBERG, 2013), with the

singularity in $u = u'$. We will now analytically remove this singularity by considering the following Chawla-Kumar Finite Decomposition of the kernel,

$$\mathcal{K}_\ell(u, u') \approx \sum_{j=0}^M b_{j,\ell}(u) T_j(u'), \quad (3.24)$$

where we can use the orthonormality to obtain an expressions for the coefficients $b_{j,\ell}$,

$$\mathcal{K}_\ell(u, u') T_k(u') = \sum_{j=0}^M b_{j,\ell}(u) T_j(u') T_k(u'), \quad (3.25)$$

which we can use the orthogonality relations (3.18) to obtain,

$$\int_{-1}^1 \frac{\mathcal{K}_\ell(u, u') T_k(u')}{\sqrt{1-x^2}} = \sum_{j=0}^M b_{j,\ell}(u) \int_{-1}^1 \frac{T_j(u') T_k(u')}{\sqrt{1-x^2}} \quad (3.26)$$

$$= \sum_{j=0}^M b_{j,\ell}(u) \left(\frac{\pi}{2} \delta_{j,k} + \pi \delta_{j,0} \right) \quad (3.27)$$

$$\implies b_{k,\ell} = \frac{2}{\pi(1 + \delta_{k,0})} \int_{-1}^1 \frac{\mathcal{K}_\ell(u, u') T_k(u')}{\sqrt{1-x^2}}. \quad (3.28)$$

Therefore, we have:

$$E_{\mathbf{u}} f(u) \sum_n c_{n,\ell} T_n(u) + \frac{1}{\xi^2} \sum_{n,j} c_{n,\ell} b_{j,\ell}(u) \int_{-1}^1 \frac{du' T_j(u') T_n(u')}{u - u'} = E f(u) \sum_n c_{n,\ell} T_n(u), \quad (3.29)$$

now, we focus on the integral,

$$I_{j,n}(u) = \int_{-1}^1 du' \frac{T_j(u') T_n(u')}{u - u'}. \quad (3.30)$$

By applying the product formula for the Chebyshev polynomials, we get,

$$I_{j,n}(u) = \int_{-1}^1 du' \frac{T_j(u') T_n(u')}{u - u'} = \frac{1}{2} \left(\int_{-1}^1 du' \frac{T_{j+n}(u')}{u - u'} + \int_{-1}^1 du' \frac{T_{|j-n|}(u')}{u - u'} \right). \quad (3.31)$$

Since there is a recursive formula for the Chebyshev polynomials, we only need to calculate orders zero and one. We begin with order 0, which can have a value assigned using the Cauchy Principal Value,

$$\int_{-1}^1 du' \frac{T_0(u')}{u - u'} = \int_{-1}^1 du' \frac{1}{u - u'} = \lim_{\epsilon^+ \rightarrow 0} \left[\int_{-1}^{a-\epsilon} \frac{du'}{u - u'} + \int_{a+\epsilon}^1 \frac{du'}{u - u'} \right] = \ln \left| \frac{1+u}{1-u} \right|, \quad (3.32)$$

for order 1,

$$\int_{-1}^1 du' \frac{T_1(u')}{u - u'} = \int_{-1}^1 du' \frac{u'}{u - u'} \quad (3.33)$$

$$= \lim_{\epsilon^+ \rightarrow 0} \left[\int_{-1}^{a-\epsilon} du' \frac{u'}{u - u'} + \int_{a+\epsilon}^1 du' \frac{u'}{u - u'} \right] \quad (3.34)$$

$$= -2 + u \ln \left| \frac{1+u}{1-u} \right|, \quad (3.35)$$

and therefore, successive orders can be obtained in terms of the Cauchy's Principal Values generated using the recursive relations for Chebyshev Polynomials given in Eqs. (3.16) and (3.17). We are now able to write,

$$\lambda_i(u) = \int_{-1}^1 du' \frac{T_i(u')}{u - u'}, \quad (3.36)$$

that obeys the following relations,

$$\lambda_0(u) = \ln \left| \frac{1+u}{1-u} \right| \quad (3.37)$$

$$\lambda_1(u) = -2 + u\lambda_0(u) \quad (3.38)$$

$$\lambda_{k+1}(u) - 2u\lambda_k(u) + \lambda_{k-1}(u) = 2 \frac{(1 + \cos(k\pi))}{k^2 - 1} \quad (3.39)$$

where in the last expression, $k \geq 2$. Using Eqs (3.38), (3.39) and the product formula (3.17) in equation (3.30), one obtains:

$$I_{j,n}(u) = \int_{-1}^1 du' \frac{T_j(u')T_n(u')}{u - u'} = \frac{1}{2} (\lambda_{j+n}(u) + \lambda_{|j-n|}(u)), \quad (3.40)$$

which allows to write:

$$E_{\mathbf{u}} f(u) \sum_n c_{n,\ell} T_n(u) + \frac{1}{2\xi^2} \sum_{n,j} c_{n,\ell} b_{j,\ell}(u) (\lambda_{j+n}(u) + \lambda_{|j-n|}(u)) = E f(u) \sum_n c_{n,\ell} T_n(u), \quad (3.41)$$

that represents a generalized eigenvalue problem for which we choose for u_i , namely the zeros of the Chebyshev polynomial of order $n + 1$.

In figure 3.1, we can see the convergence of the Chebyshev-Chawla-Kumar method, where $N = M$ for different angular mesh points. There different avenues to improve convergence such as a more detailed investigation of the scaling parameter ξ and the

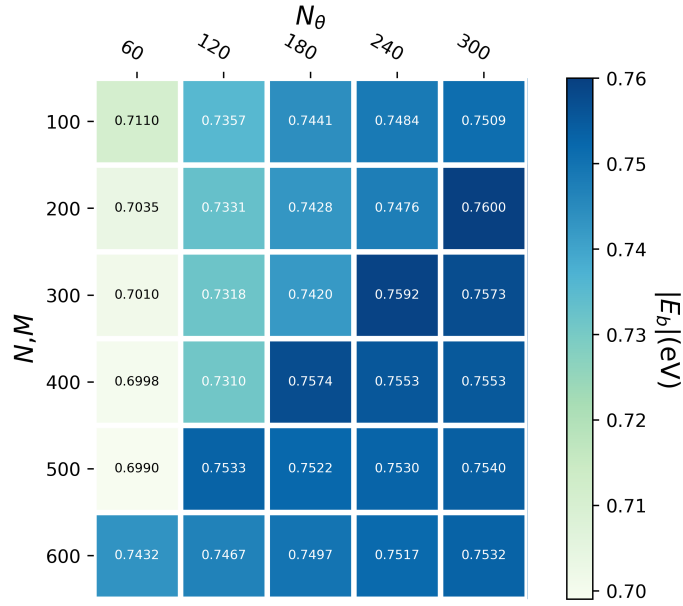


FIGURE 3.1 – (Color online) Graphical convergence table for the Chebyhev-Chawla-Kumar method using the Rytova-Keldysh potential (1.24).

weight function $f(u)$. In particular, we can use

$$f(u) = \frac{1 - u^3}{1 + u}, \quad (3.42)$$

which in our tests showed the better behavior. Suppose we have solved our integral equation for the exciton wave function. Now we can obtain the wave function in configuration space using the Fourier transform

$$\psi_{n,\ell}(\mathbf{r}) = \int d^2\mathbf{p} e^{i\mathbf{p}\cdot\mathbf{r}} \psi_\ell(p) e^{i\ell\phi'}. \quad (3.43)$$

By implementing the angular integration, we have that

$$\begin{aligned} \psi_{n,\ell}(r, \phi) &= \frac{2}{\xi^2} e^{i\ell\phi} \sum_n c_{n,\ell} \int_{-1}^1 du \frac{1+u}{(1-u)^3} \\ &\times J_\ell \left(\frac{r}{\xi} \frac{1+u}{1-u} \right) f(u) T_n(u), \end{aligned} \quad (3.44)$$

with J_ℓ being the Bessel function of order ℓ . To understand the assumed procedure, let us exemplify with the calculation of the following quantity $F(q)$ of interest

$$\langle F \rangle = \int dq q F(q) \psi_{n_1}(q) \dots \psi_{n_N}(q). \quad (3.45)$$

To do this, first, we write the above equation in terms of u

$$\begin{aligned} \langle F \rangle &= \int du F(q(u)) \left[\frac{1+u}{(1-u)^3} f(u) \right]^{n_N} \\ &\times \sum_{j_1 \dots j_{n_N}} c_{j_1}^{n_1} T_{j_1}(u) \dots c_{j_{n_N}}^{n_{n_N}} T_{j_{n_N}}(u). \end{aligned} \quad (3.46)$$

The next step is to write the integrand of Eq. (3.46) in terms of a single Chebyshev expansion

$$\begin{aligned} F(q(u)) &\left[\frac{(1-u)^3}{1+u} \right]^{n_N-1} \times \sum_{j_1 \dots j_{n_N}} c_{j_1}^{n_1} T_{j_1}(u) \dots c_{j_{n_N}}^{n_{n_N}} T_{j_{n_N}}(u) \\ &= \sum_k b_k T_k(u). \end{aligned} \quad (3.47)$$

Now use the orthogonality of the polynomials, similarly as we showed in equation (3.30). After that, we can use the Clenshaw-Curtis method to obtain

$$\langle F \rangle = \sum_{k=0}^{\infty} \frac{2b_{2k}}{1-(2k)^2}. \quad (3.48)$$

3.1.2 Quadrature Solution

Here we will present a different approach to the solution of the Wannier Equation with Partial-Wave decomposition. We can recast (3.9) with the hyperbolic conformal mapping as,

$$\phi_\ell(u) = \frac{1}{\xi^2 \pi} \int_{-1}^1 du' \frac{(1+u') \mathcal{V}_\ell(u, u') \phi_\ell(u')}{(1-u')^3 (E - E_{\mathbf{u}})}. \quad (3.49)$$

We can rewrite the integral in terms of the Gauss-Legendre quadrature (STOER; BURRISCH, 1980), that is,

$$\int_{-1}^1 f(x) dx \approx \sum_{i=1}^N \omega_i f(x_i), \quad (3.50)$$

where x_i are the roots of the n -th Legendre polynomial and ω_i are the quadrature weights,

$$\omega_i = \frac{2}{(1-x_i)^2 (P'_n(x_i))^2}. \quad (3.51)$$

Using this procedure we have,

$$\phi_\ell(u) = \frac{1}{\xi^2 \pi} \sum_{j=1}^N \omega_j \frac{(1 + u'_j) \mathcal{V}_\ell(u, u'_j) \phi_\ell(u'_j)}{(1 - u'_j)^3 (E - E_{\mathbf{u}})}, \quad (3.52)$$

where we have an equation for each $u \in [-1, 1]$,

$$\phi_\ell(u_i) = \frac{1}{\xi^2 \pi} \sum_{j=1}^N \omega_j \frac{(1 + u'_j) \mathcal{V}_\ell(u_i, u'_j) \phi_\ell(u'_j)}{(1 - u'_j)^3 (E - E_{u_i})}. \quad (3.53)$$

We can recast this problem as a matrix problem by introducing the vector quantity $\vec{\phi} = [\phi(u_1), \phi(u_2), \dots, \phi(u_n)]^T$,

$$\vec{\phi} = \mathcal{M}(E) \vec{\phi}, \quad (3.54)$$

where,

$$\mathcal{M}_{i,j}(E) = \frac{1}{\xi^2 \pi} \frac{(1 + u'_j) \mathcal{V}_\ell(u_i, u'_j) \phi_\ell(u'_j)}{(1 - u'_j)^3 (E - E_{u_i})}. \quad (3.55)$$

The procedure here is to search for an energy E that solves for the unit eigenvalue. The matrix equation (3.54) only admits non-trivial solutions when,

$$\det(I - M(E)) = 0. \quad (3.56)$$

3.1.3 Comparison

Here we will consider the system subject to the Rytova-Keldysh potential (1.24), rewritten here for convenience,

$$V_{RK}(q) = -\frac{1}{4\pi^2} \left(\frac{2\pi e^2}{4\pi\epsilon_0 q (1 + 2r_0 q)} \right), \quad (3.57)$$

as our testing potential, which is the monolayer limit (which is obtained by taking the interlayer separation to infinity, $d \rightarrow \infty$) of equation (??) derived in the first chapter. Here we will consider $r_0 = 26.87\text{\AA}$, and the exciton reduced mass as $\mu = 0.25m_0$ where m_0 is the free electron mass. These parameters simulate the exciton in a MoS₂ monolayer. In 3.1.3 we present a small but enlightening comparison. Notice that both values agrees very well. In fig 3.2 we compare the wave functions for the S -wave in different states, where we also see good agreement.

TABLE 3.1 – The convergence of exciton ground state binding energy as a function of the number of radial momenta mesh points N_p , obtained with RK potential for the MoS₂ from the Gauss-Legendre quadrature method. The number of angular mesh points is 61. The exciton binding energy of -753.1 meV for $N_p \rightarrow \infty$ is obtained with a quadratic extrapolation, while the Chebyshev Method yields a binding energy of -753.0 meV for $N = M = 600$ and $N_\theta = 320$, where N is the number of mesh points for the u variable, M is the number of terms in the finite decomposition and N_θ is the number of mesh points for the angular quadrature which stems from the partial-wave decomposition.

N_p	E_b (meV)
300	-788.3
400	-778.8
500	-773.3
600	-769.5
700	-768.2
800	-765.4
900	-764.1
1000	-762.9
$N_p \rightarrow \infty$	-753.1

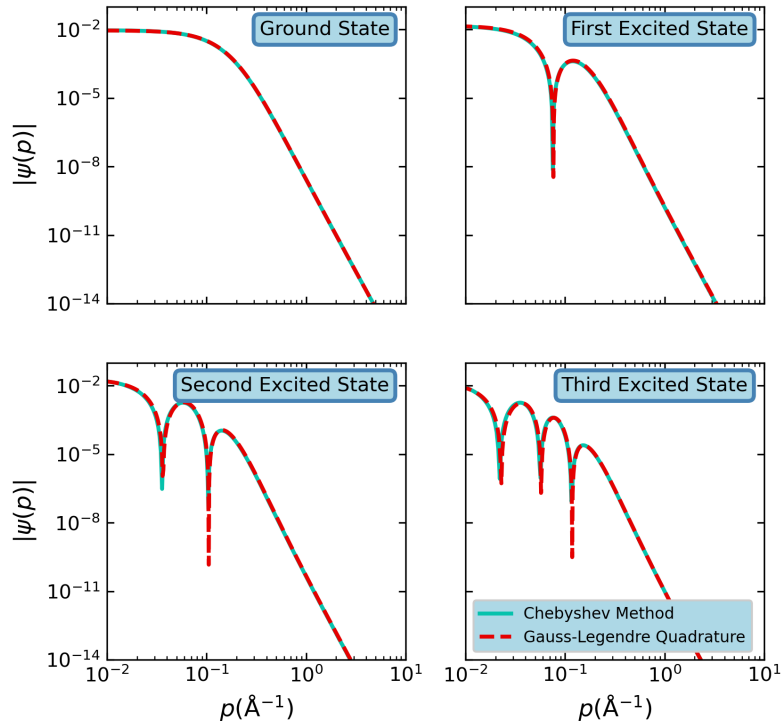


FIGURE 3.2 – (Color online) Comparison between the Gauss-Legendre quadrature method (with 1000 radial mesh points and 61 angular mesh points) and the Chebyshev method ($N = M = 600$ and $N_\theta = 320$) for different states of the MoS₂ exciton using the RK potential. $\psi_i(p)$ is the i -th excited state for the S -wave.

3.2 2D Gauss-Legendre Quadrature

In this short section we discuss the possibility of considering the full problem and writing down a two dimensional quadrature scheme. This is the method we will apply in the case of the phosphorene. We begin with,

$$\psi(\mathbf{p}) = \lambda \int \frac{d^2 \mathbf{p}'}{(2\pi)^2} \frac{V(\mathbf{p} - \mathbf{p}')}{E - E_{\mathbf{p}}} \psi(\mathbf{p}'). \quad (3.58)$$

We can write down a quadrature scheme for the 2D problem, with the hyperbolic conformal mapping for the radial part and a linear mapping for the angle variables, $\theta' = (1+x)\pi$, where x are Gauss-Legendre nodes,

$$\psi(p, \theta) = \lambda \sum_{i,j} \frac{\omega_i \omega_j}{(4\pi)} \frac{(1 + u'_i) V(p, u'_i, x_j)}{(1 - u'_i)^3 (E - E_p)} \psi(u'_i, \theta'_j). \quad (3.59)$$

This class of methods have a much higher computational complexity and generally much more computationally intensive compared to the other methods. However, when one tackles more complex problems, involving three particles or more, having a good grasp of such techniques is of great aid. We will leave further discussion of this method to later as it is the method we employed to solve systems with no rotational invariance.

3.3 Variational Methods

As a final topic in this chapter, we introduce one last method that we will use to corroborate our results: the Variational Methods.

This class of methods rest upon the foundations laid down by the Variational Principle of Quantum Mechanics, which states that, for a trial wave function $|\tilde{0}\rangle$ we can calculate the following expectation value of a given Hamiltonian $\hat{\mathcal{H}}$,

$$\tilde{E} = \frac{\langle \tilde{0} | \hat{\mathcal{H}} | \tilde{0} \rangle}{\langle \tilde{0} | \tilde{0} \rangle}, \quad (3.60)$$

which in turn can give an upper bound to the true value of the *de facto* ground state energy, E_0 , of the Hamiltonian $\hat{\mathcal{H}}$, that is,

$$\frac{\langle \tilde{0} | \hat{\mathcal{H}} | \tilde{0} \rangle}{\langle \tilde{0} | \tilde{0} \rangle} \geq E_0. \quad (3.61)$$

With the variational principle we can make reasonable estimates concerning the ground state properties of the Hamiltonian. In our case, the exciton problem can be thought as a

two-body problem, similar to the hydrogen atom, that for the relative coordinates reads in position representation as,

$$\hat{\mathcal{H}} = \frac{\hbar^2}{2\mu} \nabla^2 + V(r), \quad (3.62)$$

where μ is the reduced mass of the system, which in our case is formulated in the effective-mass approximation,

$$\frac{1}{\mu} = \frac{1}{m_e} + \frac{1}{m_h}, \quad (3.63)$$

such that m_e (m_h) is the electron (hole) effective mass.

There are a multitude of approaches for the construction of a basis that gives us good estimates of the ground-state energy, here we will present one approach, the *Generating Coordinate Method* (PIZA *et al.*, 1977; WONG, 1970; GRIFFIN; WHEELER, 1957), which was conceived in nuclear physics to describe collective modes.

3.3.1 Generating Coordinate Method

Here we consider the following wave function as a guess for the variational estimate,

$$\psi_\ell^\nu(r, \theta) = A_\nu e^{i\ell\theta} r^\ell \sum_{i=1}^N e^{-\alpha_i r}. \quad (3.64)$$

This estimate yields two fundamental properties of hydrogen-like systems, the angular momentum barrier for finite angular momenta, encapsulated in r^ℓ and the radial exponential decay for large distances, encapsulated by $e^{-\alpha r}$. The set of values $\{\alpha\}$ is distributed in a logarithm grid Ω dictated by the term Γ ,

$$\Omega = \frac{\ln \alpha}{\Gamma}. \quad (3.65)$$

Here, we see a couple of details. There are two distinct parameters that governs the basis set, Ω and Γ . The choice of parameters depends on the basis function (PIZA *et al.*, 1977). First, let us find an expression for A_ν by using the normalization condition,

$$\int d\mathbf{r} (\psi_\ell^\nu)^* \psi_\ell^\nu = 2\pi |A_\nu|^2 \int dr r^{2|\ell|+1} e^{-\alpha_i r} = \frac{2\pi |A_\nu|^2 \Gamma(2|\ell| + 2)}{\alpha_i^{2|\ell|+2}} = 1, \quad (3.66)$$

solving for $|A_\nu|$ yields,

$$|A_\nu| = \sqrt{\frac{\alpha_i^{2|\ell|+2}}{2\pi\Gamma(2|\ell|+2)}}. \quad (3.67)$$

Also, we need to calculate the overlap integral,

$$\int d\mathbf{r} (\psi_\ell^{\nu'})^* \psi_\ell^\nu = 2\pi A_\nu A_{\nu'} \int dr r^{2|\ell|+1} e^{-(\alpha_i+\alpha_j)r} = \frac{(\alpha_i\alpha_j)^{|\ell|+1}}{(\alpha_i+\alpha_j)^{2|\ell|+2}} \quad (3.68)$$

Now, we need to calculate the matrix elements in Eq. (3.60). First, we begin with the kinetic energy,

$$\langle \psi_\ell^\mu | T | \psi_\ell^\nu \rangle = \int d\mathbf{r} (\psi_\ell^{\nu'})^* \frac{-\hbar^2}{2\mu} \nabla^2 \psi_\ell^\nu = -\frac{\hbar^2}{2\mu} \int d\mathbf{r} (\psi_\ell^{\nu'})^* \left(\frac{\partial^2}{\partial r^2} + \frac{1}{r} \frac{\partial}{\partial r} + \frac{1}{r^2} \frac{\partial^2}{\partial \theta^2} \right) \psi_\ell^\nu, \quad (3.69)$$

this integral has an analytical expression,

$$\langle \psi_\ell^\mu | \mathbf{T} | \psi_\ell^\nu \rangle = \frac{\hbar^2 (\alpha_i\alpha_j)^{|\ell|+2}}{2\bar{\mu}(\alpha_i+\alpha_j)^{2|\ell|+2}}. \quad (3.70)$$

For a general potential $V(r)$, there is no analytical expression. In general, we can write down, for a spherically symmetric system, the matrix element:

$$\langle \psi_\ell^\mu | V | \psi_\ell^\nu \rangle = \frac{(\alpha_i\alpha_j)^{|\ell|+1}}{\Gamma(2|\ell|+2)} \int dr r^{2|\ell|+1} V(r) e^{-(\alpha_i+\alpha_j)r}, \quad (3.71)$$

and, in particular, for the Coulomb Potential $V(r) = -\hbar c \alpha r^{-1}$.

$$\langle \psi_\ell^\mu | V | \psi_\ell^\nu \rangle = -2\pi\alpha\hbar c A_\nu A_{\nu'} \int dr r^{2|\ell|} e^{-(\alpha_i+\alpha_j)r} = -\frac{\alpha\hbar c (\alpha_i\alpha_j)^{|\ell|+1}}{(\alpha_i+\alpha_j)^{2|\ell|+1}}. \quad (3.72)$$

Here, we take $\Gamma = 5$ and set the interval $[-2, 2]$. The number of points by which we subdivide the interval is obtained by trial and error, which some references agree on $N = 48$ (QUINTELA; PERES, 2020). By choosing this set of parameters and grid, we arrive at a binding energy of $E_b = 752$ meV, which shows a good agreement with our Chebyshev results.

3.4 Final Remarks

Here we have discussed some numerical methods in order to solve with the two-body problem. These methods can be extended to more complex systems through different

schemes, such as the Faddeev Equations (for an example of the Faddeev Equations applied to 2D materials, see (MOHSENI *et al.*, 2023)), or the Gaussian Expansion Method, championed by Hiyama (HIYAMA, 2012; KAMIMURA, 1988). Since we are aiming to study more complex few-body complexes in 2D materials in the future, having a good basis in integral and Variational methods proves to be a good platform to start with while also laying foundations for the derivation of the results in the following chapters.

4 Tunable Properties of Excitons in Double Monolayer Semiconductor Heterostructures

Given the variety of possible heterostructures, it is interesting to understand the engineering obtained by the formation stacked materials as well as the other tunable parameters (dielectric screening and layer separation). This combination of materials and environmental modifications leads to a large number of combinations of interlayer and intralayer excitons.

The first application of the formalism developed above is a systematic study of both intralayer and interlayer exciton and its mutability with respect to the changes in the interlayer distance and in the dielectric environment (TENÓRIO *et al.*, 2023). Here we solve the following Wannier equation,

$$E_p\psi(\mathbf{p}) + \int \frac{d\mathbf{p}'}{(2\pi)^2} V(\mathbf{p} - \mathbf{p}')\psi(\mathbf{p}') = E\psi(\mathbf{p}), \quad (4.1)$$

using the Chebyshev-Chawla-Kumar Method discussed in 3.1.1. This development is significantly computationally cheaper compared to other first-principle methods and monte-carlos approaches.

We investigate two semiconductor monolayers separated by a spacer with width d and dielectric constant ϵ_2 . The substrate ($z < -d$) and superstrate ($z > 0$) have dielectric constants ϵ_3 and ϵ_1 , respectively, as depicted in Fig. 4.1(a). Here, we consider different TMDs semiconductors represented by the symbol MX_2 , where M is a metal [molybdenum (Mo) or tungsten (W)] and X is a chalcogenide [selenium (Se) or sulfur (S)]. Homo and heterostructures are formed by taking the same or different TMDs in the double-layer system, respectively. In Fig. 4.1(b), we depict the energy gap values for the four investigated TMDs here. Note that the resulting heterobilayers lead to a type II band alignment (ZHANG *et al.*, 2016), that strongly favors the formation of interlayer excitons (LATINI *et al.*, 2017). To correctly predict the exciton energies, determined as the differ-

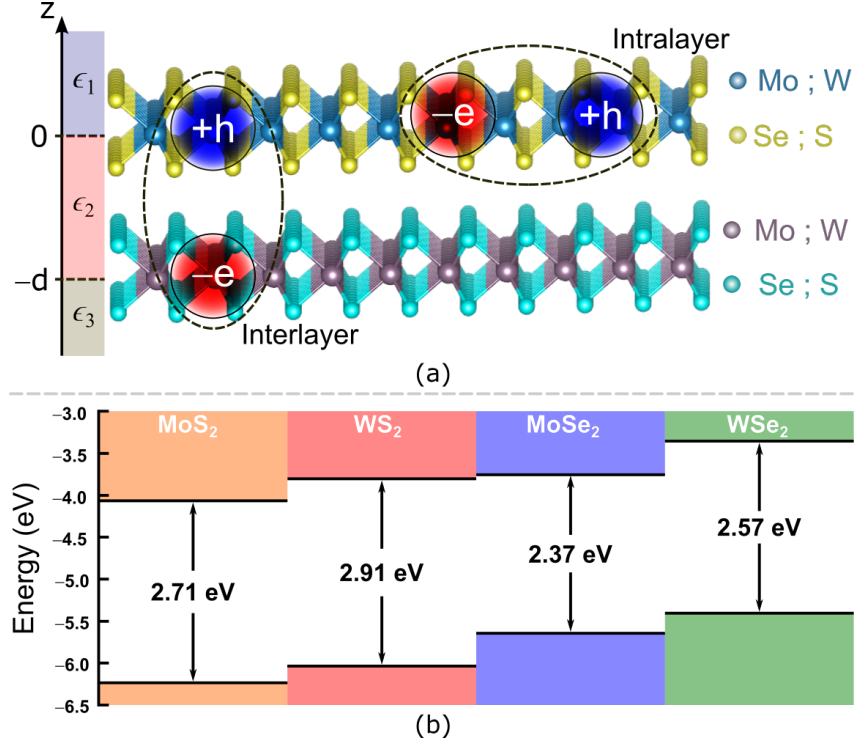


FIGURE 4.1 – (Color online) (a) Schematic illustration of the double layered TMDs, separated by a spacer of dielectric constant ϵ_2 ($-d \leq z \leq 0$) and width d , immersed in two materials of dielectric constants ϵ_1 ($z > 0$) and ϵ_3 ($z < -d$). This structure sustains both intralayer and interlayer excitons. (b) Band alignment as measured from the vacuum between the four TMDs considered in this work. The bandgap energies and their alignments were obtained from DFT calculations in Ref. (ZHANG *et al.*, 2016).

ence between the bandgap and the magnitude of the exciton binding energy, we consider the effects of the dielectric geometry on the carrier-carrier interaction as the solution of the corresponding Poisson equation derived in the first chapter. We use the Wannier equation in the effective mass approximation to calculate the exciton energy, which was proven to coincide with a microscopic model (HAVE *et al.*, 2019). For the bandgap, we use the exchange self-energy (CHAVES *et al.*, 2017) within the continuum model, which was developed in detail in chapter 2, equation (2.58).

4.1 Bandgap Engineering

The quasiparticle band structure of 2D materials depends on the dielectric environment (CHAVES *et al.*, 2020). To account for this dependence, we employ the Semiconductor Bloch Equations (SBE) developed in the chapter 2 for the heterostructure depicted in Fig. 4.1(a). We neglect the tunneling between the MX_2 layers due to the presence of a dielectric spacer between them. In order to take into account the corrections to the bandgap, we employed the procedure derived in Ref. (CHAVES *et al.*, 2017) and discussed in chapter 2, by considering the aforementioned gapped Dirac equation (2.1), the electron-electron interaction (2.4), and a dipole coupling with light (2.46). It is well-known

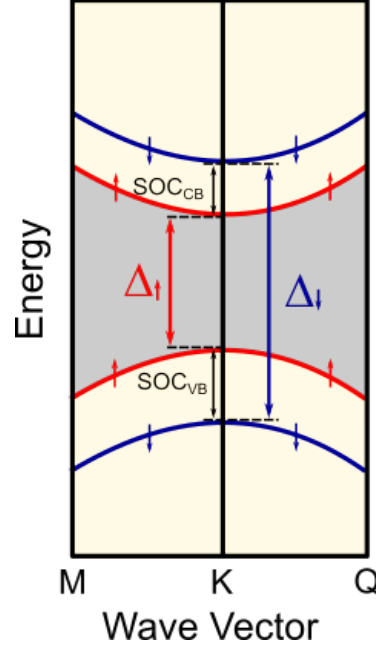


FIGURE 4.2 – (Color online) Schematic illustration of the lowest conduction (CB) and valence (VB) bands of monolayer TMDs in the vicinity of the K (red curves) and K' (blue curves) points, emphasizing the band splitting due to SOC and spin flipping for each band in the opposite valley due to the inversion symmetry. The up (red) and down (blue) arrows stand for spin-up and spin-down states. SOC_{CB} (SOC_{VB}) corresponds to the energetic split of the conduction (valence) band.

that TMDs have a strong spin-orbit coupling (SOC) originating from the d orbitals of the metal atoms and, consequently, it induces a spin splitting of bands in monolayer, (LIU *et al.*, 2015) as illustrated in Fig. 4.2. In the continuum limit, (2.58) is written as,

$$\Sigma_{s\tau}^j(\mathbf{k}) = \int \frac{d\mathbf{q}}{4\pi^2} V_{jj}(q) n_{s\tau}(\mathbf{k} - \mathbf{q}) \frac{4\hbar^2 v_F^2 \mathbf{k} \cdot \mathbf{q} + (\Delta_{s,\tau}^0)^2}{4E_{jk}^{s\tau} E_{jq}^{s\tau}}, \quad (4.2)$$

from which we can calculate the dressed bandgap as

$$\Delta_{s\tau}^j = \Delta_{s\tau,0}^j + \Sigma_{s\tau}^j(k=0), \quad (4.3)$$

where $\Delta_{s,\tau}^j$ denotes the energy difference between the conduction and valence bands with the same s and τ indexes for each layer j at the K point, the intralayer potential V_{jj} is given by Eq. (1.21), $n_{s\tau}$ is the valence electronic density, and $E_{jk}^{s\tau}$ is the eigenvalue of the massive 2D Dirac Hamiltonian. The intralayer interaction depends on the dielectric environment through the spacer width d , the dielectric constants ϵ_i , and the monolayer screening lengths r_i . As our goal is to study the dependence of the exciton properties on the system geometry, we fit the monolayers screening length r_0 to reproduce the experimental exciton energy of the suspended monolayer for each MX_2 .

The fitting procedure is we take the experimental values for the exciton energy in suspended samples (KLOTS *et al.*, 2014; XIE *et al.*, 2021; HARATS *et al.*, 2020; ASLAN *et al.*,

TABLE 4.1 – Effective masses, screening factor r_0 , and the bandgap (ZHANG *et al.*, 2016) of each material. The masses are obtained from Ref. (KORMÁNYOS *et al.*, 2015) and the screening factors are obtained via a fitting procedure. The screening factors in the fifth column are from ref. (PEDERSEN, 2016), while the experimentally obtained binding energies for each row are, respectively (KLOTS *et al.*, 2014; XIE *et al.*, 2021; HARATS *et al.*, 2020; ASLAN *et al.*, 2021)

Materials	m_e	m_h	r_0	r_0	Δ_K (eV)	E_b (meV)
MoS ₂	0.47	0.54	27.04 Å	23.45 Å	2.71	−753.0
MoSe ₂	0.58	0.6	35.34 Å	26.13 Å	2.37	−711.7
WS ₂	0.27	0.36	20.85 Å	16.59 Å	2.91	−900.0
WSe ₂	0.29	0.36	21.80 Å	20.09 Å	2.57	−890.0

2021), the band gap calculated in ref. (ZHANG *et al.*, 2016) and the spin-orbit coupling splitting from (KORMÁNYOS *et al.*, 2015), and solve the Wannier equation for each monolayer TMDC with the rytova-keldysh potential, fitting the screening length r_0 . After obtaining the r_0 , we use it as a input for the dressed bandgap and solve for the bare band gap which gives the transition energy calculated in ref. (ZHANG *et al.*, 2016). With the r_0 and $\Delta_{st,0}^j$ we can evaluate the change in the band gap for each layer configuration and dielectric environment, which the exchange self-energy takes in account. The obtained values are presented in Table 4.2.

With the fitted values of r_0 and Δ_{st}^0 , we can solve Eq. (4.2) for different geometric setups and study the dependence of the Δ_{st}^j , *i.e.* the spin/valley dependent transition energy at the K point. In Fig. 4.3(a), we show that the mutual electrostatic screening between two monolayers can decrease the value of Δ_{st}^j by 50 meV as the interlayer separation decreases to 7.15 Å. In Fig. 4.3(b), we show the dependence of Δ_{st}^j on the spacer dielectric constant. The huge renormalization of the bandgap due to the electron-electron interaction (UGEDA *et al.*, 2014) is weakened by the spacer dielectric screening, and as the dielectric constant is increased, the transition energy approaches the bare value $\Delta_{st,0}$. In Figs. 4.3(a) and 4.3(b) it was assumed the MoS₂/MoSe₂ heterostructure, however qualitatively similar results are expected for the other different TMD layer compound combinations.

With the formalism and procedures established, we can dive into the results and see how the excitonic spectra and wave function is tunable.

4.2 Results

Figures 4.4(a) and 4.4(b) show the binding energy of the intralayer A excitons, which are formed when the electron-hole pair lies on the MoS₂ layer, as a function of the separation distance (spacer width) d and the dielectric constant of the spacer ϵ_m , respectively.

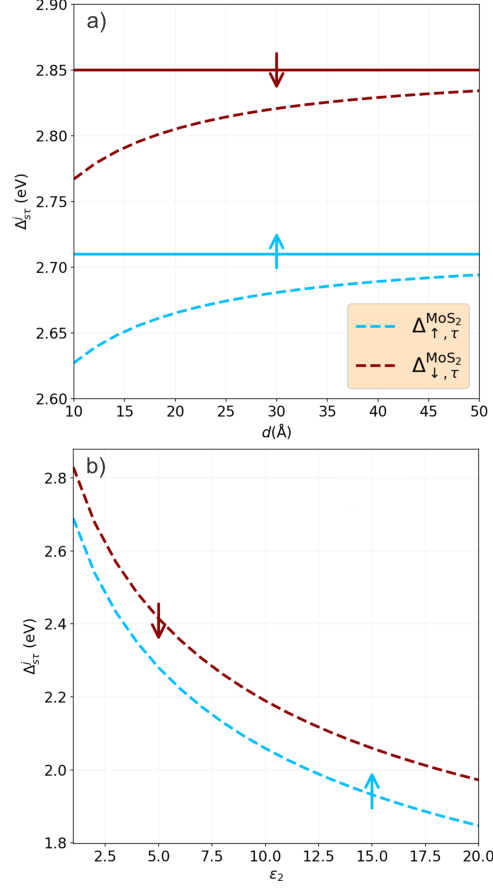


FIGURE 4.3 – (Color online) $K - K$ transition energies of both spins for MoS₂ at the MoS₂/MoSe₂ heterostructure with respect to the changes (a) in the interlayer separation d in a suspended sample with $\epsilon_1 = \epsilon_2 = \epsilon_3 = 1$, and (b) in the spacer dielectric constant ϵ_2 with a fixed interlayer distance $d = 7.15$ Å and external dielectric constants $\epsilon_1 = \epsilon_3 = 1$. Cyan and red curves correspond to up ($\Delta_{\uparrow, \tau}^{\text{MoS}_2}$) and down ($\Delta_{\downarrow, \tau}^{\text{MoS}_2}$) spin results, respectively. The solid lines in (a) represent a monolayer limit ($d \rightarrow \infty$) of the MoS₂.

TABLE 4.2 – *Ab initio* bandgaps (ZHANG *et al.*, 2016), Fermi velocity (KORMÁNYOS *et al.*, 2015) and calculated bare bandgaps using Eq. (4.3) and the fit r_0 's given in Table 4.1 for the four investigated TMDs and different combinations of spin and valley indexes.

Materials	Δ_{\uparrow} (eV)	Δ_{\downarrow} (eV)	v_F (eV · Å)	Δ_{\uparrow}^0 (eV)	Δ_{\downarrow}^0 (eV)
MoS ₂	2.71	2.85	2.76	1.29	1.39
MoSe ₂	2.37	2.55	2.53	1.18	1.32
WS ₂	2.96	3.30	3.34	1.35	1.61
WSe ₂	2.63	3.01	3.17	1.14	1.40

Results for three different layer compounds in the heterostructure formation are shown: (red solid curve) MoS₂ – MoSe₂, (green dashed curve) MoS₂ – WSe₂, and (blue dotted curve) MoS₂ – WS₂. As a consequence of the fact that MoSe₂ has the larger r_0 value (see Table 4.1) of the four investigated TMD layers, it was already expected that it would screen more effectively the electron-hole interaction by the charge-image effect. As verified

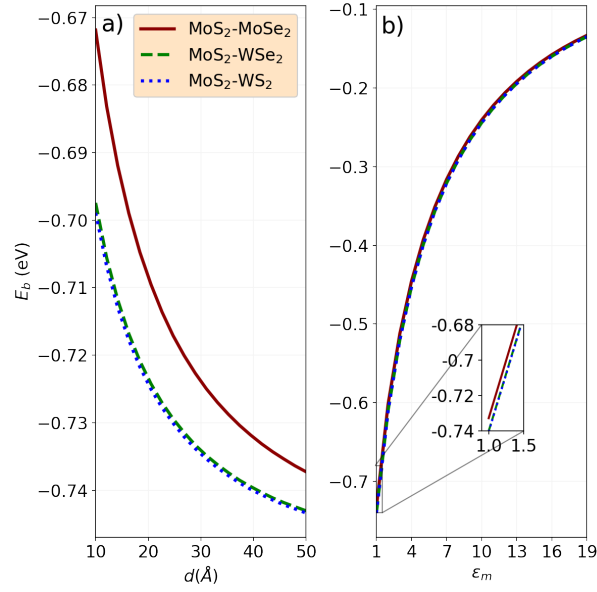


FIGURE 4.4 – (Color online) Binding energies (E_B) of the intralayer A excitons, referred to as an electron-hole pair lying in the MoS₂ layer, by taking different layer compounds in the TMD heterostructure formation. Red solid, green dashed, and blue dotted curves correspond to MoS₂ – MoSe₂, MoS₂ – WSe₂, and MoS₂ – WS₂ double-layers, respectively. Panels (a) and (b) show the dependence of E_B on the separation distance of the layers d , by assuming $\epsilon_1 = \epsilon_2 = \epsilon_m = 1$, and on the dielectric constant ϵ_m , by assuming a fixed interlayer distance of $d = 41$ Å and dielectric constants of the substrate and superstrate as $\epsilon_1 = \epsilon_2 = 1$, respectively. An enlargement as an inset in panel (b) emphasizes the small energetic difference between the binding energies for the MoS₂ – MoSe₂ heterojunction and the other two, MoS₂ – WSe₂ and MoS₂ – WS₂, double-layers.

in Fig. 4.4(a), it lowers the exciton binding energy by almost 20 meV, whereas the WSe₂ and WS₂ cases present almost identical binding energies due to their very similar r_0 values. From Fig. 4.4(b), one notices that the intralayer A exciton binding energies are strongly affected by the spacer’s dielectric constant ϵ_m changes, exhibiting an energetic variation on the order of 300 meV when ϵ_m varies from 1 to 4. Qualitatively similar results were reported in the TMD monolayer case in Refs. (KYLÄNPÄÄ; KOMSA, 2015; CHAVES *et al.*, 2020), being physically understood by the spatial localization of the interlayer A exciton depicted in Fig. 4.4 that lies only in one of the layers of the double-layer TMD system. Moreover, a small energetic difference of the order of a few meV is noted in Fig. 4.4(b) for the binding energies of the intralayer A excitons in the MoS₂ when one compares the different investigated heterostructures. It is emphasized by the enlargement shown as an inset of Fig. 4.4(b). It reveals structural independence in the heterostructure formation on the binding energy as a function of the dielectric constant, *i.e.* ϵ_m changes similarly affect the binding energies regardless of the adjacent TMD layer of the MoS₂-formed heterostructure.

Let us now focus on the interlayer exciton. When stacking different TMD monolayers, the corresponding Dirac K points in the reciprocal space of each TMD monolayer will not coincide, and the distance between the respective K points of each layer depends both

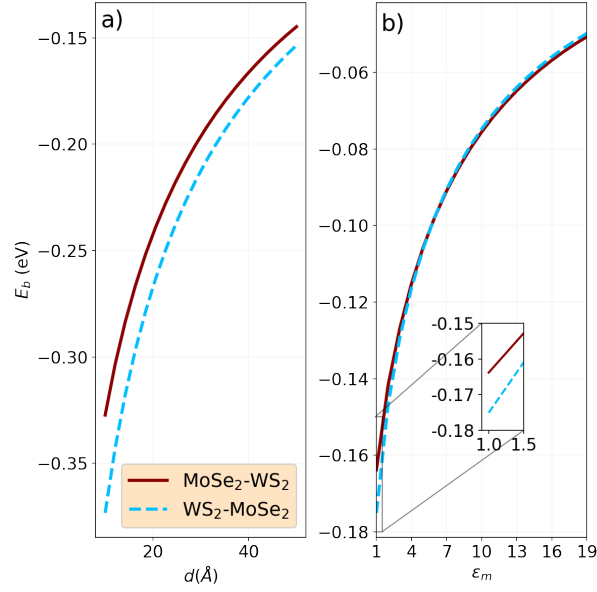


FIGURE 4.5 – (Color online) Binding energies (E_B) of the interlayer excitons in the MoSe₂ layer by taking different layer compounds in the TMD heterostructure formation. Red solid and cyan dashed curves correspond to MoSe₂ – WS₂ and WS₂ – MoSe₂, respectively, with the interlayer exciton being formed by the electron (hole) of the first (second) referred compound. Panels (a) and (b) show the dependence of E_B on the separation distance of the layers d , by assuming $\epsilon_1 = \epsilon_2 = \epsilon_m = 1$, and on the dielectric constant ϵ_m , by assuming a fixed interlayer distance of $d = 41$ Å and dielectric constants of the substrate and superstrate as $\epsilon_1 = \epsilon_2 = 1$, respectively. An enlargement of an inset in panel (b) emphasizes the energetic difference between the binding energies for the MoSe₂ – WS₂ and WS₂ – MoSe₂ double-layers.

on the relative rotation of the crystallography orientation and the mismatch of the lattice parameters of each layer. Here, within the effective mass approximation, we are ignoring both effects. Considering only the uppermost valence band and the lowest conduction band of each layer, there are two different kinds of interlayer excitons for the type II band alignment case (see Fig. 4.1): (i) the lowest conduction band between the two 2D materials hosting the electron, whereas the hole is hosted in the valence band of the adjacent layer that possesses the highest energy, and (ii) the opposite formation, *i.e.* the highest conduction band between the TMD monolayers hosting the electron, whereas the hole is hosted in the valence band of the adjacent layer that possesses the lowest energy. If the corresponding exciton binding energy has a magnitude smaller than the conduction band offset, this will result in an excitonic resonance, as the exciton energy lies inside the conduction band.

Results for these two mentioned kinds of interlayer excitons in double-layer heterostructures composed by MoSe₂ and WS₂ compounds are shown in Fig. 4.5. The solid red (dashed cyan) curve corresponds to the interlayer exciton formed by an electron (hole) from the MoSe₂ (WS₂) and a hole from the WS₂ (MoSe₂). Both interlayer exciton configurations show a binding energy increase when the layer separation d decreases, attaining values of almost 400 meV for shorter distances of the order of 10 Å [see Fig. 4.5(a)]. Such

behavior is easily understood by the electrostatic interaction nature of the electron-hole attraction, which is enhanced the shorter the interlayer distance. One also observes in Fig. 4.5(a) that the energetic difference of the binding energies for the two configurations of interlayer excitons, *i.e.* $|E_b^{\text{MoSe}_2\text{-WS}_2} - E_b^{\text{WS}_2\text{-MoSe}_2}|$, increases when the interlayer distance decreases. Knowing that the interlayer interaction depends on the layer separation and the screening parameters r_0 of heterostructures' compounds, and in addition to that, here we are switching the layers where the electron and hole are positioned, one can link this energetic difference $|E_b^{\text{MoSe}_2\text{-WS}_2} - E_b^{\text{WS}_2\text{-MoSe}_2}|$ in view of the interlayer exciton formation and the consequent overall strength switching of the role of the electrostatic interaction at each layer. Note that the electrostatic interaction of an electron-hole pair separated by a dielectric media has its amplitude modulated by the electrostatic screening of the layers damped by the separation between them. Thus, by exchanging the configuration of the electron-hole layer location, one leads to dampening/enhancing the screening of the adjacent layer owing to the layer separation and consequently to an energetic difference in the binding energy of the exciton. A similar feature is observed in the case that we fixed the layer separation and vary the dielectric constants of the environment. This is present in Fig. 4.5(b). Note that the interlayer exciton binding energy exhibits the same tendency as the intralayer one [see Fig. 4.4(b)] as a function of the spacer dielectric constant ϵ_m , except for the increased energetic distancing between the two $\text{MoSe}_2 - \text{WS}_2$ and $\text{WS}_2 - \text{MoSe}_2$ cases when ϵ_m assumes high values, as emphasized in the inset of Fig. 4.5(b).

In what follows, we study the exciton energy, which is defined by

$$E_{\text{exc}} = E_c - E_v - |E_b|, \quad (4.4)$$

where $|E_b|$ is the magnitude of the exciton binding energy, E_c the bottom of the conduction band, and E_v the top of the valence band associated with the electron and hole, respectively, that contributes to the exciton formation. For a bright exciton, this value also corresponds to the energy of the photon that creates the electron-hole bound-state.

From now on, for an $\text{MX}_2\text{-M}'\text{X}'_2$ heterostructure, we define the interlayer exciton IX_1 as the bound-state of the electron from the lowest conduction band of the first material and the hole from the highest valence band of the second material and IX_2 , as the opposite. In Fig. 4.7, we show the evolution of the exciton energies, both intralayer and interlayer, and the bottom value of the conduction band as a function of [Fig. 4.7(a)] the interlayer spacing and [Fig. 4.7(b)] the dielectric constant of the spacer. It is worth mentioning that we use as a reference energy level the top of the valence band, considering the band alignment of Ref. (ZHANG *et al.*, 2016). One can see in Fig. 4.7(a) that the intralayer exciton energies (solid blue and yellow curves for WSe_2 and MoSe_2 , respectively) are very robust with respect to the layer separation due to the simultaneous changes of the bandgap and the

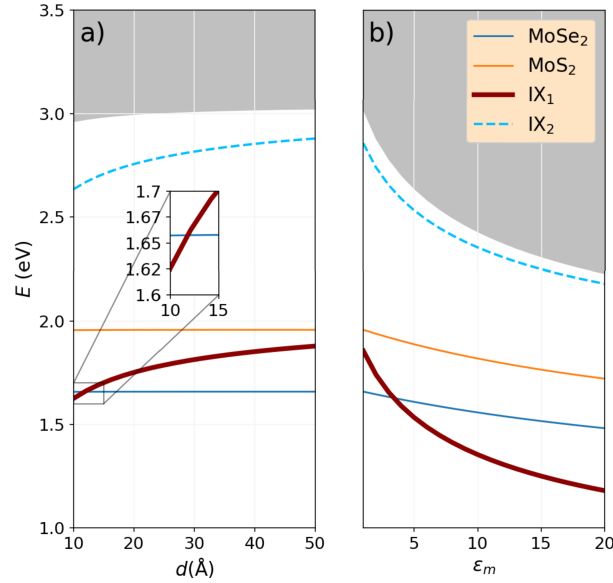


FIGURE 4.6 – (Color online) Exciton energy dependency on (a) the layer separation and (b) the dielectric media ϵ_m for the MoS₂-MoSe₂ heterostructure. IX_{*i*} denotes the *i*-th interlayer exciton, such that IX₁ (IX₂) is formed by the electron from the lowest conduction band of the first (second) material and the hole from the highest valence band of the second (first) material with result represented by the solid red (dashed cyan) curve. Solid blue and yellow curves correspond to the intralayer excitons for MoSe₂ and MoS₂ cases, respectively. (a) All dielectric constants are held fixed with the value of 1, and (b) the layer separation is fixed to $d = 41$ Å. The shaded gray region corresponds to the continuum. An enlargement around small layer separation is shown as an inset of panel (a).

exciton binding energy, which cancel each other out, keeping the energies of the intralayer exciton unaltered. As the interlayer separation d increases, the value of each intralayer exciton energy converges to the suspended monolayer value minus the band alignment energy. For the interlayer exciton (see solid red and dashed cyan curves for IX₁ and IX₂, respectively), we have that the exciton energy increases due to the weakening of the binding energy, which arises from the sensitivity of the interlayer interaction with respect to the layer separation. For instance, notice in Fig. 4.7(a) that the interlayer exciton IX₁ energy (dashed cyan curve) increases 0.15 eV for $d = 50$ Å. By Fig. 4.7(b), one observes that the intralayer exciton energy is more sensitive to changes in the dielectric media. By increasing the dielectric constant of the space ϵ_m , the screening is enhanced and, therefore, weakening the Coulomb interaction. Although the interlayer exciton binding energy varies less with respect to the dielectric screening, the gap correction is more acute, leading to a larger fluctuation of the interlayer exciton energy.

Similarly to Fig. 4.7, in Fig. 4.6 we present results for the exciton energy for (a) different layer separations and (b) dielectric media of the spacer, but now for the MoS₂-MoSe₂ heterostructure. By comparing Figs. 4.7 and 4.6, one observes a similar overall behavior for the interlayer and intralayer excitons, owing to the screened interaction and the geometrical disposition of the heterostructure, showing qualitative physical trends that are independent of the TMD layers composition. Unlike the MoSe₂-WSe₂ case [see

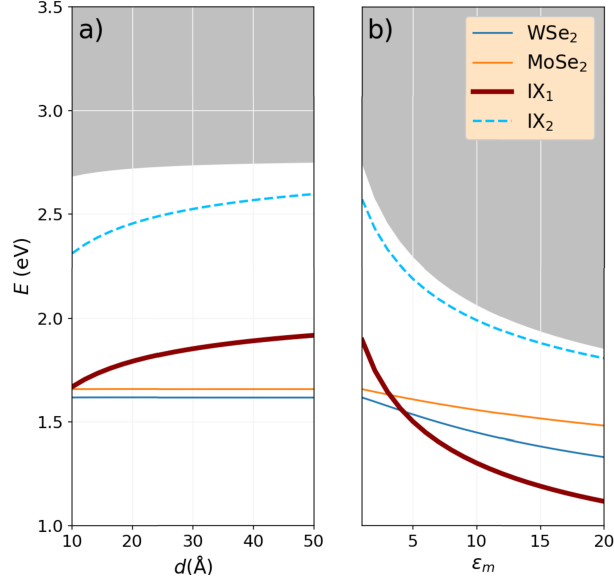


FIGURE 4.7 – (Color online) Exciton energy dependency on (a) the layer separation and (b) the dielectric media ϵ_m for the MoSe_2 - WSe_2 heterostructure. IX_i denotes the i -th interlayer exciton, such that IX_1 (IX_2) is formed by the electron from the lowest conduction band of the first (second) material and the hole from the highest valence band of the second (first) material with result represented by the solid red (dashed cyan) curve. Solid blue and yellow curves correspond to the intralayer excitons for WSe_2 and MoSe_2 cases, respectively. (a) All dielectric constants are held fixed with the value of 1, and (b) the layer separation is fixed to $d = 41$ Å. The shaded gray region corresponds to the continuum.

Fig. 4.7(a)], for the MoS_2 - MoSe_2 case, the lowest exciton energy for small layer separation is the interlayer IX_1 , as emphasized in the inset of Fig. 4.6(a). As seen in Fig. 4.6(b), the dielectric media allows tuning both interlayer and intralayer exciton states, lowering their frequencies as larger the dielectric constant, exhibiting a more pronounced effect on the interlayer case.

Finally, we explore the spatial distribution of the exciton wave function. In Figures 4.8(a,b) and 4.8(c,d) show color maps of the intralayer and interlayer exciton wave functions by varying (a,c) the interlayer distance d and (b,d) the dielectric constant ϵ_m of the spacer. Figure 4.8(a) depicts no pronounced change in the spatial distribution of the intralayer exciton wave function when changing the interlayer distance. This can be linked to the energetic negligible changes in the binding energy as shown by the very small energetic scale variation in Fig. 4.4(a). On the other hand, as already expected, since by changing the dielectric constant the electron-hole interaction should vary, Fig. 4.8(b) shows different spatial distributions of the intralayer exciton wave function when varying the dielectric constant of the spacer. The higher ϵ_m value the lower the electron-hole interaction and consequently the binding energy value becomes smaller [see Fig. 4.4(b)] and thus the exciton wave function spreads more, *i.e.* increasing the exciton size. Figures 4.8(c,d) demonstrate that the interlayer exciton wave function is much more sensitive to changes in the layer separation Fig. 4.8(c) than the intralayer case Fig. 4.8(a). This is to be expected because the Coulomb interaction for interlayer exciton gets weaker with

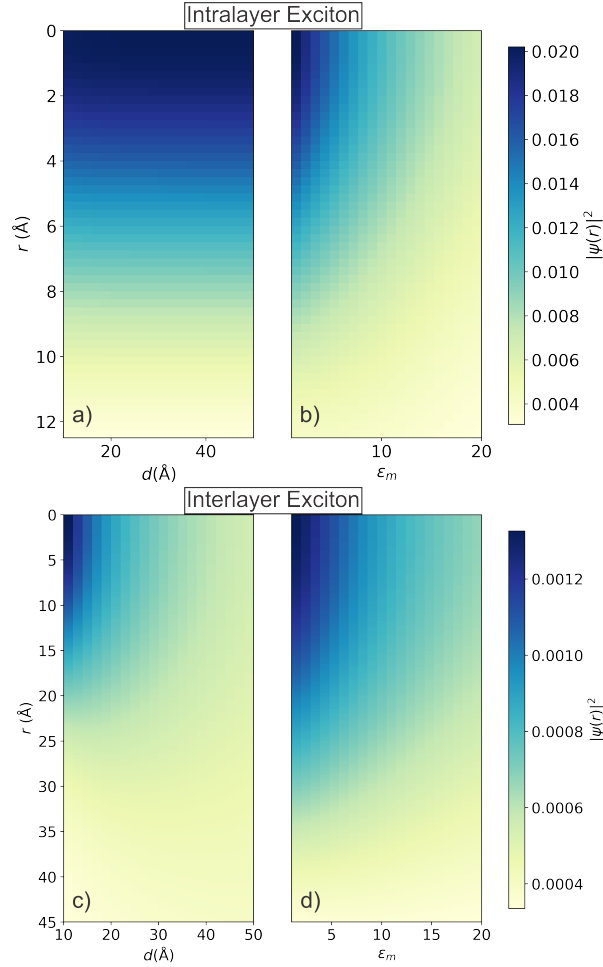


FIGURE 4.8 – (Color online) (a,b) Intralayer and (c,d) interlayer exciton wave function for the MoS₂-MoSe₂ heterostructure as a function of (a,c) the layer separation and (b,d) the dielectric constant. The dielectric constants are held fixed at 1 for panels (a) and (c), whereas the value for the interlayer distance is fixed of $d = 41$ Å in panels (b) and (d).

the increase of the layer separation, leading to spreading out the in-plane wave function. From Figs. 4.8(c,d), one notices that the wave function covers a larger spatial region for the interlayer case compared to the intralayer case Figs. 4.8(a,b), for both cases of changing the layer separation (being up to 35 Å in panel (c)) and the interlayer dielectric constant (being up to 50 Å in panel (d)).

4.2.1 Excitonic-Based Insulating Phase in Bilayer MoS₂-WTe₂

The idea of a excitonic insulator dates back to the late 60s (KOHN, 1967; JÉROME *et al.*, 1967), which was found following an analogy to the BCS theory. Although, one central difference with the ordinary BCS theory is the absence of off-diagonal long-range order while still maintaining a diagonal long-range order (JÉROME *et al.*, 1967), which stems from the crystalline structure and the Coulomb interaction, which affects the behavior of the two-particle density matrix. Although the excitonic insulator was a theoretical

curiosity from the late sixties, recently, the theme drew a large attention due to the rise of two-dimensional materials which have shown evidence for such phase (JIA *et al.*, 2022; ROSSNAGEL *et al.*, 2002; BOK *et al.*, 2021). This phase of matter is particularly interesting, it happens that the formation of excitons is more natural with respect to free electrons in the conduction band, leading to an exciton condensation and, therefore, to an insulating phase.

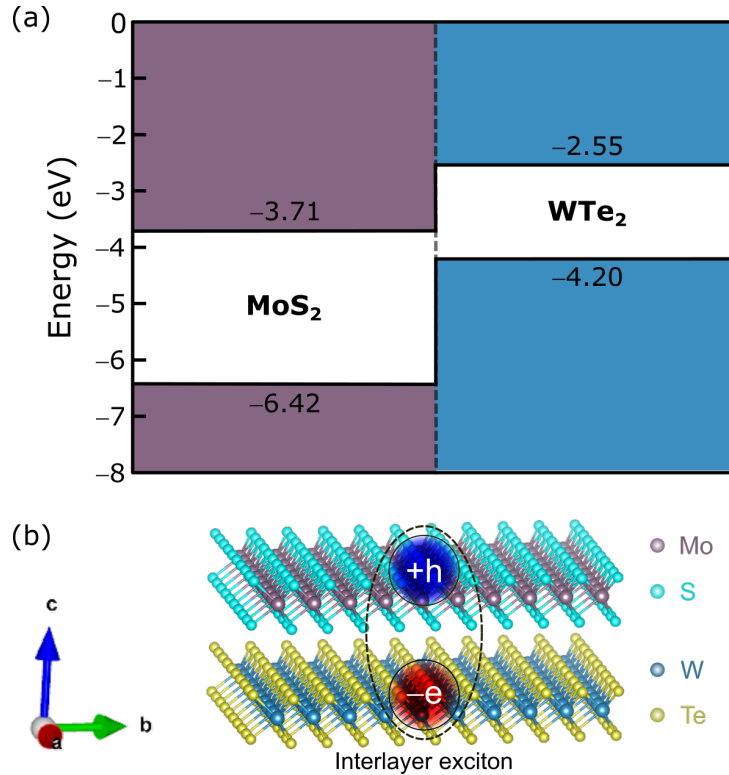


FIGURE 4.9 – (Color online) Band alignment of MoS₂-WTe₂ bilayer. Here, the interlayer quasiparticle bandgap is the difference of the conduction band energy of MoS₂ and the valence band energy of WTe₂, $E_g = 0.49\text{eV}$. The values were taken from (ZHANG *et al.*, 2016).

The formation of heterostructures bound by van der Waals interaction leads to a additional degree of freedom for the engineering of excitonic states (GEIM; GRIGORIEVA, 2013; LI *et al.*, 2016; TENÓRIO *et al.*, 2023), which can be used as a platform to study this novel quantum phase of matter. In particular, by analyzing the band alignment of such structures, as we can see in Fig. 4.9, the quasiparticle bandgap for the interlayer exciton, that is, one electron in MoS₂ and a hole in WSe₂, has the quasiparticle bandgap of $E_g = 0.49\text{eV}$, which raises the question: is there a possible hetero-bilayer configuration, for a given environment and dielectric medium, in which the binding energy of the interlayer exciton is of the order or greater than the quasiparticle bandgap?

We aim to answer this question by using the general methodology discussed so far. First, we need the screening parameter in order to calculate the binding energies. The screening parameter for WTe₂ can be estimated using the same fitting procedure for the bare bandgap, but reverse engineering to fit the screening length. Doing so, we found the

TABLE 4.3 – Effective masses, screening factor r_0 , and the band gap of each material. The masses are from (KORMÁNYOS *et al.*, 2015) and Δ_K from (ZHANG *et al.*, 2016). The screening factors, r_0 , for WTe₂ are obtained from Eq. (4.2).

Materials	m_e	m_h	$r_0(\text{\AA})$	$\Delta_K(\text{eV})$
MoS ₂	0.47	0.54	27.04	2.71
WTe ₂	0.25	0.32	51.12	1.93

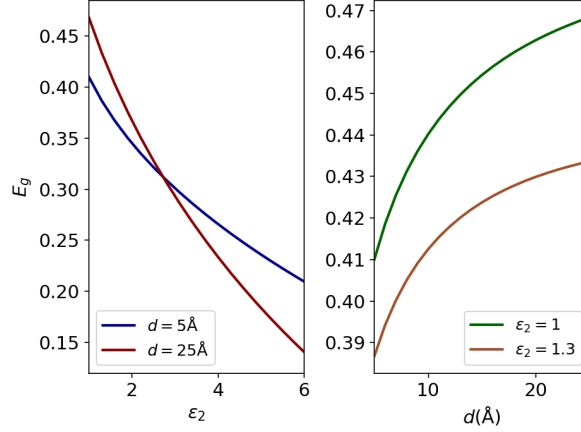


FIGURE 4.10 – (Color online) Band gap evolution with respect to the dielectric media and layer separation.

results presented in Table 4.3. Our values of r_0 agree quite well with the universal scaling relations derived in Ref. (JIANG *et al.*, 2017). Once we have determined the parameters of the potential, we can calculate the exciton energy and check the layer separation and dielectric media for which the exciton binding energy is larger than the band gap.

First, we present the gap evolution with respect to the dielectric media and layer separation in Fig. 4.10. As we can see, the interlayer transition gap ($E_g = E_c^{\text{MoS}_2} - E_v^{\text{WTe}_2}$) is fairly narrow and of the order of the excitonic spectra we have already reported for the interlayer case. Now we present in Fig. 4.11 the exciton energy, $E_X = E_g - |E_b|$, for the system under investigation. As it can be seen from the figure, we can fine tune the exciton energy, allowing for excitonic insulating phases for several configurations. The zero energy of the exciton implies that the binding energy is equal to the band gap of the system. In this case, the formation of correlated electron-hole pairs is energetically favored with respect to the creation of conducting electrons, leading to an insulating state which is driven by the excitonic formation.

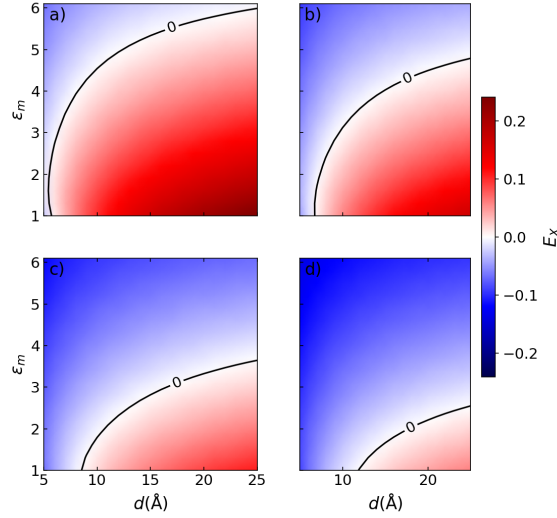


FIGURE 4.11 – (Color Online) The exciton energy for each interlayer separation and dielectric media. The blue region is where the binding energy is greater than the band gap while the red region is where the binding energy is smaller than the band gap. The solid black line is the phase boundary, where the binding energy and bandgap are equal. In each panel, we set a particular dielectric substrate, a) $\epsilon_1 = 1$, b) $\epsilon_1 = 2$, c) $\epsilon_1 = 3$ and d) $\epsilon_1 = 4$.

4.3 Conclusions

In summary, we have presented a theoretical framework based on an appropriate expansion of the excitonic wave function in terms of Chebyshev polynomials to solve the excitonic Wannier equation for double-layer heterostructures. These double-layers are formed by different TMDs separated by a dielectric spacer. The employed method showed a fast convergence and numerical reliability with a computationally cheap scheme, owing to the recursive relations of the Chebyshev polynomials and the Chawla-Kumar decomposition that allowed us to integrate out the infrared divergence of the electron-hole interaction.

Based on the mentioned theoretical approach, we explored the excitonic spectrum for intralayer and interlayer exciton configurations and its tunability through dielectric engineering, which arises from the screened Coulomb interaction. We found a robustness of the intralayer state with respect to the layer separation, while the interlayer exciton energy increases due to the binding energy sensitivity to layer separation. By changing the dielectric media, the intralayer exciton energy decreases, although not as sharply as the interlayer exciton one, which has the weakest binding for a large dielectric constant. Moreover, we have also obtained corrections to the bandgap using the semiconductor Bloch equations formalism, which enabled us to understand how to layer separation and dielectric media affect the exciton energy. Our findings showed that even the energetic ordering relative to the intralayer and interlayer excitons can be modified by changes in the layer separation and in the dielectric constant of the spacer. Therefore, by dielectric

engineering of the surrounding environment, we showed that the excitonic properties in double-layer van der Waals materials can be driven, enabling a bandgap control that suits different technological applications.

Also, as discussed in Figs. 4.10 and 4.11, we can engineer a configuration in which the exciton binding energy is larger than the gap, leading to a phase where it is more energetically favorable to form correlated electron-hole pairs than free electrons in the conduction band, leading to an insulating state.

We hope that our theoretical approach and results based on Chebyshev's polynomial expansion for Wannier excitonic complexes will prove useful for the exploration of optoelectronics properties in different van der Waals materials with a layer-by-layer stacking and surrounding environment controlling, and moreover being a simple and efficient tool for explaining cutting edge experiments in double layer 2D semiconductors, such as non-linear optical susceptibilities.

5 Excitons in Black Phosphorous

While transition metal dichalcogenides form a large class of materials with interesting excitonic properties, there are other candidates for optoelectronic applications, such as the monolayer black phosphorous (AKHTAR *et al.*, 2017). Here we will solve the Wannier Equation for this system, taking in account the anisotropy in the carrier dispersion relation and discuss its effects on the exciton structure.

5.1 The Hamiltonian

In order to tackle the problem, we will consider an effective mass theory. In the case of the black phosphorous, as we can see from geometrical point of view, two orthogonal directions have different atomic placements. In one direction, we have atoms in a zigzag form, and in other direction, we have atoms in a armchair form. This leads to formulate the effective mass as direction dependent, with the Hamiltonian of the following form:

$$H = -\frac{\hbar^2}{2m_e^x} \frac{\partial^2}{\partial x_e} - \frac{\hbar^2}{2m_e^y} \frac{\partial^2}{\partial y_e} - \frac{\hbar^2}{2m_h^x} \frac{\partial^2}{\partial x_h} - \frac{\hbar^2}{2m_h^y} \frac{\partial^2}{\partial y_h} + V(\mathbf{r}_e, \mathbf{r}_h). \quad (5.1)$$

The common prescription is to solve the energy eigenvalue equation with Jacobi coordinates, which separates out the center of mass coordinate. Let $\vec{r}_e = (x_e, y_e)$ and $\vec{R}_h = (x_h, y_h)$ be the positions of the electron and the hole, respectively. Consider the following center of mass coordinate,

$$\bar{x} = \frac{m_e^x x_e + m_h^x x_h}{m_e^x + m_h^x} \quad (5.2)$$

$$\bar{y} = \frac{m_e^y y_e + m_h^y y_h}{m_e^y + m_h^y}. \quad (5.3)$$

Let $\vec{r}_{rel} = \vec{r}_e - \vec{R}_h$ be the relative position vector, then,

$$x_{rel} = x_e - x_h \implies x_e = x_{rel} + x_h ; x_h = x_e - x_{rel} \quad (5.4)$$

$$y_{rel} = y_e - y_h \implies y_e = y_{rel} + y_h ; y_h = y_e - y_{rel}, \quad (5.5)$$

now we can write down the electron and hole coordinates in terms of both the center of mass and a mass-deformed relative position. For the electron we have,

$$\bar{x} = \frac{1}{m_e^x + m_h^x} (m_e^x x_e + m_h^x (x_e - x_{rel})) \implies x_e = \bar{x} + \frac{m_h^x}{m_e^x + m_h^x} x_{rel}, \quad (5.6)$$

$$\bar{y} = \frac{1}{m_e^y + m_h^y} (m_e^y y_e + m_h^y (y_e - y_{rel})) \implies y_e = \bar{y} + \frac{m_h^y}{m_e^y + m_h^y} y_{rel}, \quad (5.7)$$

and for the hole,

$$\bar{x} = \frac{1}{m_e^x + m_h^x} (m_e^x (x_{rel} + x_h) + m_h^x x_h) \implies x_h = \bar{x} - \frac{m_e^x}{m_e^x + m_h^x} x_{rel}, \quad (5.8)$$

$$\bar{y} = \frac{1}{m_e^y + m_h^y} (m_e^y (y_{rel} + y_h) + m_h^y y_h) \implies y_h = \bar{y} - \frac{m_e^y}{m_e^y + m_h^y} y_{rel}. \quad (5.9)$$

Now we will apply the chain rule. Starting with the x direction, we redefine $M^x = m_e^x + m_h^x$ and $M^y = m_e^y + m_h^y$,

$$\frac{\partial}{\partial x_e} = \frac{\partial x_{rel}}{\partial x_e} \frac{\partial}{\partial x_{rel}} + \frac{\partial \bar{x}}{\partial x_e} \frac{\partial}{\partial \bar{x}} = \frac{\partial}{\partial x_{rel}} + \frac{m_e^x}{M^x} \frac{\partial}{\partial \bar{x}} \quad (5.10)$$

$$\frac{\partial}{\partial x_h} = \frac{\partial x_{rel}}{\partial x_h} \frac{\partial}{\partial x_{rel}} + \frac{\partial \bar{x}}{\partial x_h} \frac{\partial}{\partial \bar{x}} = -\frac{\partial}{\partial x_{rel}} + \frac{m_h^x}{M^x} \frac{\partial}{\partial \bar{x}}, \quad (5.11)$$

for the second order derivative,

$$\begin{aligned} \frac{\partial^2}{\partial x_e^2} &= \frac{\partial}{\partial x_e} \left(\frac{\partial x_{rel}}{\partial x_e} \frac{\partial}{\partial x_{rel}} \right) + \frac{\partial}{\partial x_e} \left(\frac{\partial \bar{x}}{\partial x_e} \frac{\partial}{\partial \bar{x}} \right) \\ &= \left(\frac{\partial x_{rel}}{\partial x_e} \frac{\partial}{\partial x_{rel}} + \frac{\partial \bar{x}}{\partial x_e} \frac{\partial}{\partial \bar{x}} \right) \left(\frac{\partial x_{rel}}{\partial x_e} \frac{\partial}{\partial x_{rel}} \right) + \left(\frac{\partial x_{rel}}{\partial x_e} \frac{\partial}{\partial x_{rel}} + \frac{\partial \bar{x}}{\partial x_e} \frac{\partial}{\partial \bar{x}} \right) \left(\frac{\partial \bar{x}}{\partial x_e} \frac{\partial}{\partial \bar{x}} \right) \\ &= \frac{\partial^2}{\partial x_{rel}^2} + 2 \frac{m_e^x}{M^x} \frac{\partial^2}{\partial x_{rel} \partial \bar{x}} + \left(\frac{m_e^x}{M^x} \right)^2 \frac{\partial^2}{\partial \bar{x}^2}, \end{aligned} \quad (5.12)$$

now for the hole,

$$\begin{aligned} \frac{\partial^2}{\partial x_h^2} &= \frac{\partial}{\partial x_h} \left(\frac{\partial x_{rel}}{\partial x_h} \frac{\partial}{\partial x_{rel}} \right) + \frac{\partial}{\partial x_h} \left(\frac{\partial \bar{x}}{\partial x_h} \frac{\partial}{\partial \bar{x}} \right) \\ &= \left(\frac{\partial x_{rel}}{\partial x_h} \frac{\partial}{\partial x_{rel}} + \frac{\partial \bar{x}}{\partial x_h} \frac{\partial}{\partial \bar{x}} \right) \left(\frac{\partial x_{rel}}{\partial x_h} \frac{\partial}{\partial x_{rel}} \right) + \left(\frac{\partial x_{rel}}{\partial x_h} \frac{\partial}{\partial x_{rel}} + \frac{\partial \bar{x}}{\partial x_h} \frac{\partial}{\partial \bar{x}} \right) \left(\frac{\partial \bar{x}}{\partial x_h} \frac{\partial}{\partial \bar{x}} \right) \\ &= \frac{\partial^2}{\partial x_{rel}^2} - 2 \frac{m_h^x}{M^x} \frac{\partial^2}{\partial x_{rel} \partial \bar{x}} + \left(\frac{m_h^x}{M^x} \right)^2 \frac{\partial^2}{\partial \bar{x}^2}, \end{aligned} \quad (5.13)$$

analogously for the y coordinate,

$$\begin{aligned}
\frac{\partial^2}{\partial y_e^2} &= \frac{\partial}{\partial y_e} \left(\frac{\partial y_{rel}}{\partial y_e} \frac{\partial}{\partial y_{rel}} \right) + \frac{\partial}{\partial y_e} \left(\frac{\partial \bar{y}}{\partial y_e} \frac{\partial}{\partial \bar{y}} \right) \\
&= \left(\frac{\partial y_{rel}}{\partial y_e} \frac{\partial}{\partial y_{rel}} + \frac{\partial \bar{y}}{\partial y_e} \frac{\partial}{\partial \bar{y}} \right) \left(\frac{\partial y_{rel}}{\partial y_e} \frac{\partial}{\partial y_{rel}} \right) + \left(\frac{\partial y_{rel}}{\partial y_e} \frac{\partial}{\partial y_{rel}} + \frac{\partial \bar{y}}{\partial y_e} \frac{\partial}{\partial \bar{y}} \right) \left(\frac{\partial \bar{y}}{\partial y_e} \frac{\partial}{\partial \bar{y}} \right) \\
&= \frac{\partial^2}{\partial y_{rel}^2} + 2 \frac{m_y^e}{M^y} \frac{\partial^2}{\partial y_{rel} \partial \bar{y}} + \left(\frac{m_y^e}{M^y} \right)^2 \frac{\partial^2}{\partial \bar{y}^2},
\end{aligned} \tag{5.14}$$

for the y hole coordinate

$$\begin{aligned}
\frac{\partial^2}{\partial y_h^2} &= \frac{\partial}{\partial y_h} \left(\frac{\partial y_{rel}}{\partial y_h} \frac{\partial}{\partial y_{rel}} \right) + \frac{\partial}{\partial y_h} \left(\frac{\partial \bar{y}}{\partial y_h} \frac{\partial}{\partial \bar{y}} \right) \\
&= \left(\frac{\partial y_{rel}}{\partial y_h} \frac{\partial}{\partial y_{rel}} + \frac{\partial \bar{y}}{\partial y_h} \frac{\partial}{\partial \bar{y}} \right) \left(\frac{\partial y_{rel}}{\partial y_h} \frac{\partial}{\partial y_{rel}} \right) + \left(\frac{\partial y_{rel}}{\partial y_h} \frac{\partial}{\partial y_{rel}} + \frac{\partial \bar{y}}{\partial y_h} \frac{\partial}{\partial \bar{y}} \right) \left(\frac{\partial \bar{y}}{\partial y_h} \frac{\partial}{\partial \bar{y}} \right) \\
&= \frac{\partial^2}{\partial y_{rel}^2} - 2 \frac{m_h^y}{M^y} + \left(\frac{m_h^x}{M^y} \right)^2 \frac{\partial^2}{\partial \bar{y}^2}.
\end{aligned} \tag{5.15}$$

Finally, we can write down the kinetic energy for each coordinate, for x ,

$$\begin{aligned}
T_x &= -\frac{\hbar^2}{2m_e^x} \left(\frac{\partial^2}{\partial x_e} \right) - \frac{\hbar^2}{2m_h^x} \left(\frac{\partial^2}{\partial x_h} \right) \\
&= -\frac{\hbar^2}{2m_e^x} \left(\frac{\partial^2}{\partial x_{rel}^2} + 2 \frac{m_x^e}{M^x} \frac{\partial^2}{\partial x_{rel} \partial \bar{x}} + \left(\frac{m_x^e}{M^x} \right)^2 \frac{\partial^2}{\partial \bar{x}^2} \right) - \frac{\hbar^2}{2m_h^x} \left(\frac{\partial^2}{\partial x_{rel}^2} - 2 \frac{m_h^x}{M^x} + \left(\frac{m_h^x}{M^x} \right)^2 \frac{\partial^2}{\partial \bar{x}^2} \right) \\
&= -\frac{\hbar^2}{2m_e^x m_h^x} \left[M^x \frac{\partial^2}{\partial x_{rel}^2} + 2 \frac{1}{M^x} \left(m_e^x m_h^x \frac{\partial^2}{\partial x_{rel} \partial \bar{x}} - m_e^x m_h^x \frac{\partial^2}{\partial x_{rel} \partial \bar{x}} \right) + \frac{M^x}{(M^x)^2} \frac{\partial^2}{\partial \bar{x}^2} \right] \\
T_x &= -\frac{\hbar^2}{\mu_x} \frac{\partial^2}{\partial x_{rel}^2} - \frac{\hbar^2}{M^x} \frac{\partial^2}{\partial \bar{x}^2}
\end{aligned} \tag{5.16}$$

Now, for the y direction,

$$\begin{aligned}
T_y &= -\frac{\hbar^2}{2m_e^y} \frac{\partial^2}{\partial y_e^2} - \frac{\hbar^2}{2m_h^y} \frac{\partial^2}{\partial y_h^2} \\
&= -\frac{\hbar^2}{2m_e^y} \left(\frac{\partial^2}{\partial y_{rel}^2} + 2 \frac{m_y^e}{M^y} \frac{\partial^2}{\partial y_{rel} \partial \bar{y}} + \left(\frac{m_y^e}{M^y} \right)^2 \frac{\partial^2}{\partial \bar{y}^2} \right) - \frac{\hbar^2}{2m_h^y} \left(\frac{\partial^2}{\partial y_{rel}^2} - 2 \frac{m_h^y}{M^y} + \left(\frac{m_h^y}{M^y} \right)^2 \frac{\partial^2}{\partial \bar{y}^2} \right) \\
&= -\frac{\hbar^2}{2m_e^y m_h^y} \left[(m_e^y + m_h^y) \frac{\partial^2}{\partial y_{rel}^2} + 2 \frac{1}{M^y} \left(m_e^y m_h^y \frac{\partial^2}{\partial y_{rel} \partial \bar{y}} - m_e^y m_h^y \frac{\partial^2}{\partial y_{rel} \partial \bar{y}} \right) + \frac{M^y}{(M^y)^2} \frac{\partial^2}{\partial \bar{y}^2} \right] \\
T_y &= -\frac{\hbar^2}{\mu_y} \frac{\partial^2}{\partial y_{rel}^2} - \frac{\hbar^2}{M^y} \frac{\partial^2}{\partial \bar{y}^2}
\end{aligned} \tag{5.17}$$

where we defined an anisotropic mass for each direction, $\mu_x = \frac{m_e^x + m_h^x}{m_h^x m_e^x}$ and, $\mu_y = \frac{m_e^y + m_h^y}{m_h^y m_e^y}$, leading to the following Hamiltonian, in which we discard the center of mass coordinate since it is a trivial part,

$$H = \frac{p_x^2}{2\mu_x} + \frac{p_y^2}{2\mu_y} + V(r_{rel}). \quad (5.18)$$

Having the Hamiltonian, we can proceed to write down the Wannier equation in integral form for the problem.

5.2 Wannier Equation

As it is visible from (5.18), the introduction of the anisotropy breaks the rotational symmetry of the Hamiltonian. Let us first take the Fourier Transform of the Schrodinger eigenvalue problem,

$$\mathcal{F} \left\{ \left[\frac{p_x^2}{2\mu_x} + \frac{p_y^2}{2\mu_y} + V(\vec{r}_{rel}) \right] \psi(\vec{r}) \right\} = E \mathcal{F}\{\psi(\vec{r})\} \implies \quad (5.19)$$

$$\left[\frac{\hbar^2 q_x^2}{2\mu_x} + \frac{\hbar^2 q_y^2}{2\mu_y} \right] \tilde{\psi}(\vec{q}) + \tilde{V}(\vec{q}) * \tilde{\psi}(\vec{q}) = E \tilde{\psi}(\vec{q}), \quad (5.20)$$

where the $*$ symbol is the convolution operator. We will move the anisotropy into the interaction potential to preserve the form of the free-particle Green's function by introducing the following change of coordinates,

$$\begin{cases} q_x(\bar{q}, \theta) = \bar{q} \sqrt{\frac{\mu_x}{2\bar{\mu}m_e}} \cos(\theta) \\ q_y(\bar{q}, \theta) = \bar{q} \sqrt{\frac{\mu_y}{2\bar{\mu}m_e}} \sin(\theta) \end{cases}, \quad (5.21)$$

This coordinate system can be related to the usual polar coordinates (q, ϕ) by,

$$q^2 = q_x^2 + q_y^2 = \frac{\bar{q}^2}{2\bar{\mu}m_e} [\mu_x \cos^2(\theta) + \mu_y \sin^2(\theta)], \quad (5.22)$$

$$\frac{q_y}{q_x} = \tan \phi = \sqrt{\frac{\mu_y}{\mu_x}} \tan \theta \implies \theta = \arctan \left(\sqrt{\frac{\mu_x}{\mu_y}} \tan \phi \right). \quad (5.23)$$

With these new coordinates we can write down,

$$\frac{\hbar^2 \bar{q}^2}{4\bar{\mu}m_e} \tilde{\psi}(\bar{q}, \theta) + \tilde{V}(\bar{q}, \theta) * \tilde{\psi}(\bar{q}, \theta) = E \tilde{\psi}(\bar{q}, \theta). \quad (5.24)$$

The convolution integral can also be written in terms of the new set of coordinates by considering the Jacobian of the new system of coordinates with respect to a change from

the usual polar coordinates, $(q, \phi) \rightarrow (\bar{q}, \theta)$,

$$\frac{\partial(q_x, q_y)}{\partial(\bar{q}, \theta)} = \begin{bmatrix} \sqrt{\frac{\mu_x}{2\bar{\mu}m_e}} \cos(\theta) & -q \sqrt{\frac{\mu_x}{2\bar{\mu}m_e}} \sin(\theta) \\ \sqrt{\frac{\mu_y}{2\bar{\mu}m_e}} \sin(\theta) & q \sqrt{\frac{\mu_y}{2\bar{\mu}m_e}} \cos(\theta) \end{bmatrix}, \quad (5.25)$$

which the determinant yields the following integration measure,

$$d\vec{q} = \frac{\sqrt{\mu_x \mu_y}}{2\bar{\mu}m_e} \bar{q} d\bar{q} d\theta. \quad (5.26)$$

Finally, the problem can be explicitly written as,

$$\frac{\hbar^2 \bar{q}_1^2}{4\bar{\mu}m_e} \psi(\bar{q}_1, \theta_1) + \frac{1}{(2\pi)^2} \frac{\sqrt{\mu_x \mu_y}}{2\bar{\mu}m_e} \int_{\bar{\mathcal{R}}^2} \bar{q}_2 d\bar{q}_2 d\theta_2 V(\bar{q}_1, \theta_1, \bar{q}_2, \theta_2) \psi(\bar{q}_2, \theta_2) = E \psi(\bar{q}_1, \theta_1). \quad (5.27)$$

In order to solve this integral equation, there are a multitude of ways. One can do a partial-wave expansion of the potential into two quantum numbers and the wave-function into one quantum number which will lead into a infinitely coupled set of integral equations, where the coupling comes from the angular momentum channels and one can introduce a angular momentum cutoff to obtain binding energy estimates. The other form of solution, which we will use here, is to consider a 2-D Gauss-Legendre quadrature using a conformal mapping.

First, let us write down the integral equation for the wave function,

$$\psi(\bar{q}_1, \theta_1) = \frac{\sqrt{\mu_x \mu_y}}{8\pi^2 \bar{\mu}m_e} \int_{\bar{\mathcal{R}}^2} d\bar{q}_2 d\theta_2 \frac{\bar{q}_2 V(\bar{q}_1, \theta_1, \bar{q}_2, \theta_2) \psi(\bar{q}_2, \theta_2)}{E - \frac{\hbar^2 \bar{q}_1^2}{4\bar{\mu}m_e}}. \quad (5.28)$$

Now, introduce a conformal mapping for the radial momentum coordinate and a linear mapping for the angular coordinate,

$$\bar{q}_2 = \sqrt{\frac{2\bar{\mu}m_e}{(\mu_x - \mu_y) \cos^2(\theta_2) + \mu_y}} q_2 = \sqrt{\frac{2\bar{\mu}m_e}{(\mu_x - \mu_y) \cos^2(\theta_2) + \mu_y}} \left(\frac{1+x}{1-x} \right) \quad (5.29)$$

$$\theta_2 = \arctan \left(\frac{\mu_x}{\mu_y} \tan(\phi_2) \right) = \arctan \left(\frac{\mu_x}{\mu_y} \tan(\pi(1+x^\theta)) \right) \quad (5.30)$$

which leads to the following measures,

$$d\bar{q}_2 = \sqrt{\frac{2\bar{\mu}m_e}{(\mu_x - \mu_y) \cos^2(\theta_2) + \mu_y}} \left(\frac{2}{(1-x)^2} \right) dx \quad (5.31)$$

$$d\theta_2 = \frac{\pi \sec^2(\pi(1+x^\theta))}{\frac{\mu_y}{\mu_x} + \tan^2(\pi(1+x^\theta))} dx^\theta. \quad (5.32)$$

Parameter	Value
m_x^e	$0.18m_0$
m_y^e	$1.23m_0$
m_x^h	$0.13m_0$
m_y^h	$\approx 1000m_0$
r_0	25.76 \AA
μ_x	$0.075m_0$
μ_y	$1.23m_0$

TABLE 5.1 – Table of parameters used in this Chapter for the black phosphorous from Ref. (RODIN *et al.*, 2014). m_0 is the free electron mass. Notice the large value of m_y^h , which the it is reference claimed to be due to the flatness of the band in which the effective mass was calculated.

N	E_{bind} (eV)
20	-0.694 eV
40	-0.731 eV
60	-0.787 eV
80	-0.745 eV
100	-0.744 eV
120	-0.747 eV

TABLE 5.2 – Converge check. Results for the exciton binding energy in a single layer of black phosphorous (parameters from Table 5.1) as a function of the number of mesh points, N , for both angular and radial variables. The grid is non-uniform, having $N/2$ for $[-1, -0.9]$, $N/4$ for $[-0.9, -0.8]$ and $N/4$ for $[-0.8, 1]$.

With these set of changes, the integral problem becomes,

$$\psi(\bar{q}_1, \bar{\theta}_1) = \frac{\sqrt{\mu_x \mu_y}}{2\pi} \int dx dx^\theta \frac{(1+x) \sec^2(\pi(1+x^\theta)) G_0(E) V \psi(x, x^\theta)}{((\mu_x - \mu_y) \cos^2(\theta(x^\theta)) + \mu_y) \left(\frac{\mu_y}{\mu_x} + \tan^2(\pi(1+x^\theta)) \right) (1-x)^3}, \quad (5.33)$$

where $G_0(E) = \left(E - \frac{\hbar^2 \bar{q}_1^2}{4\bar{\mu} m_e} \right)^{-1}$ is the free-particle Green's Function. This is the equation we have to solve and the methodological steps in order to solve this equation has already been presented in chapter 3.

5.3 Binding Energy and Wave-Functions

Here we present our results for the exciton in the monolayer phosphorene. First, in Table 5.2 we show the convergence of the method developed above for the Rytova-Keldysh potential. For large number of mesh points we see a small fluctuation around -0.747 eV, which agrees very well with the literature (RODIN *et al.*, 2014; CHAVES *et al.*, 2017). The parameters used for the calculations were taken from (RODIN *et al.*, 2014) and presented in Table 5.1. In Fig. 5.1, we show the ground state exciton binding energy for different layer and dielectric media configurations. We see the general trend reported in Chapter

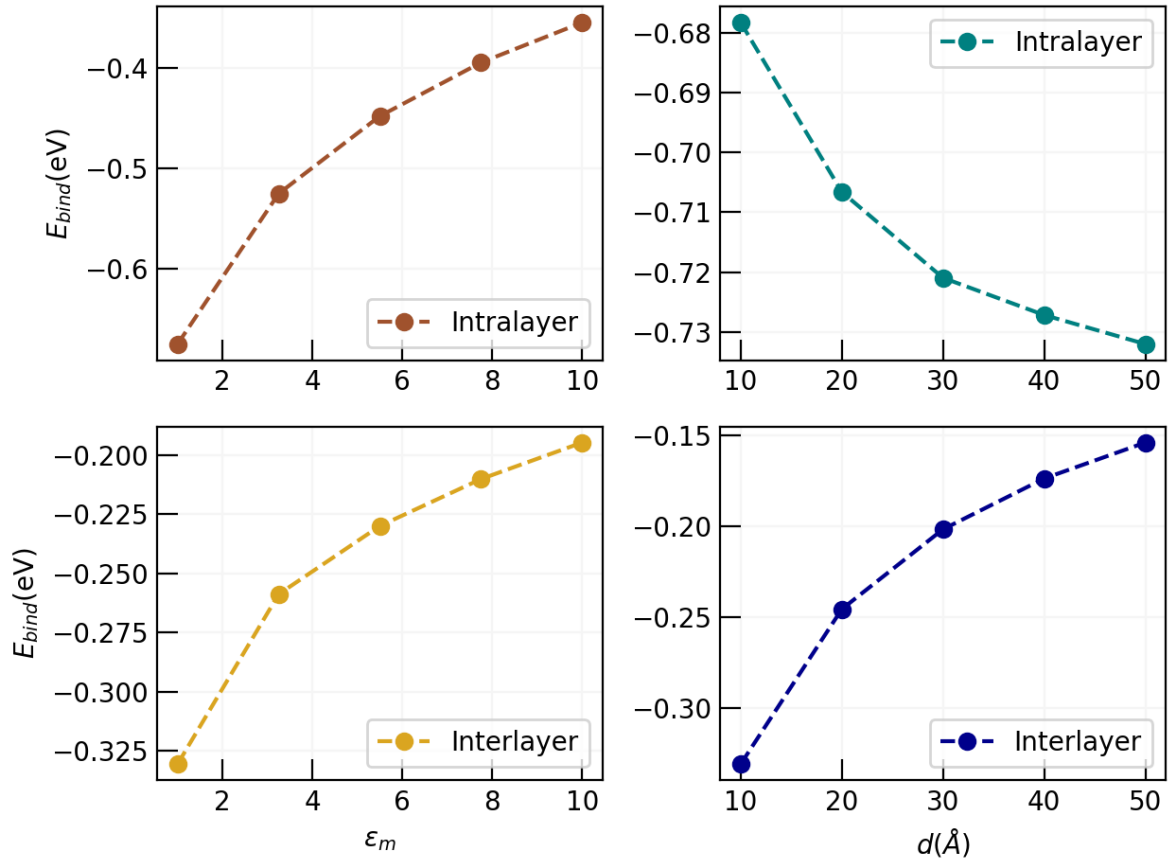


FIGURE 5.1 – (Color Online) Binding energy of the intralayer and interlayer exciton for different dielectric media (ϵ_m in ϵ_0 units) and separation distance (d in Å units) in the black phosphorous homo-bilayer. In the right panels, we have the substrate and upper dielectric media with $\epsilon_m = 1$ and in the left panels the interlayer distance is fixed at $d = 10$ Å. The parameters are given in Table 5.1.

4, in which the separation increase tends the intralayer binding energy to the monolayer limit, given by the Rytova-Keldysh potential, while bringing the interlayer exciton binding energy to zero. In the case of the dielectric screening, we see a similar effect, which weakens the potential and, therefore, also the exciton binding.

One of the most interesting properties of the system is the anisotropy, which can be explicitly seen by considering the root mean square value of the radius in each direction, and can be interpreted as a "directional" Bohr Radius,

$$R_x = \sqrt{\langle x^2 \rangle}, \quad (5.34)$$

$$R_y = \sqrt{\langle y^2 \rangle}, \quad (5.35)$$

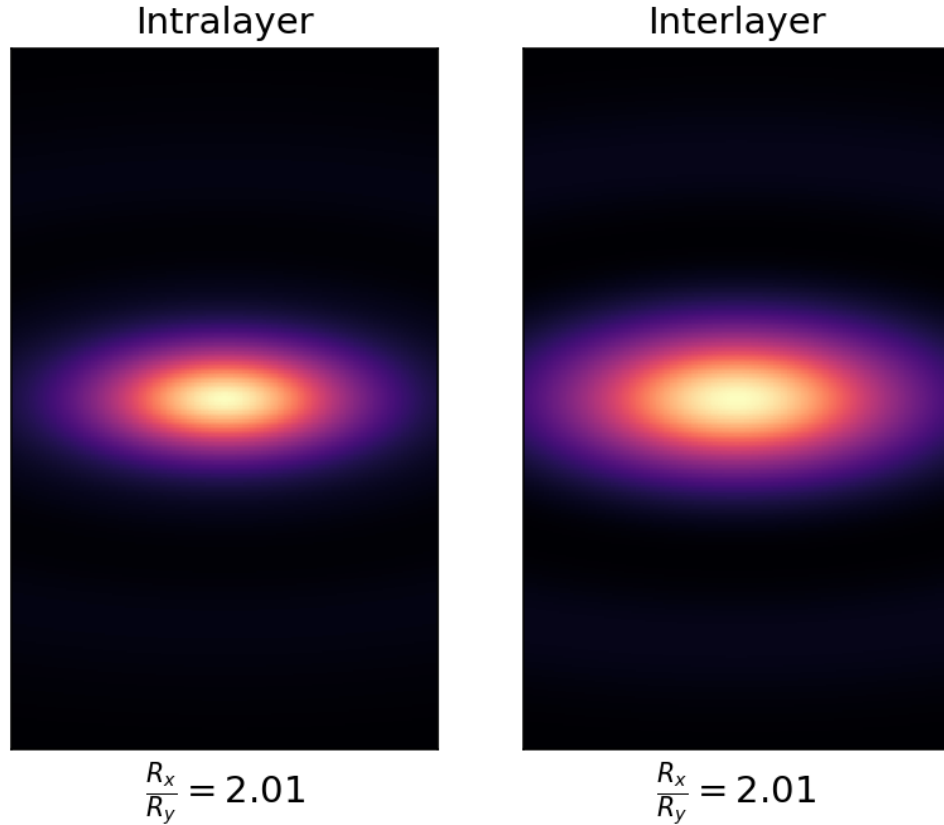


FIGURE 5.2 – (Color Online) Probability density of the ground state of the exciton for both intralayer and interlayer potential. In this case, the parameters are $d = 10 \text{ \AA}$, $\epsilon_1 = \epsilon_m = \epsilon_3 = 1$. The mass and screening parameters are given in table 5.1. The ratio of the directional radii, R_x/R_y , is practically constant independent of the system configuration, as one can see in table 5.3.

where,

$$\langle x^2 \rangle = \int d\mathbf{r} x^2 |\psi(\mathbf{r})|, \quad (5.36)$$

$$\langle y^2 \rangle = \int d\mathbf{r} y^2 |\psi(\mathbf{r})|. \quad (5.37)$$

What we found in terms of the ratio R_x/R_y is a very robust quantity with respect to the change in the dielectric environment. The interesting part is that, independent of the potential, if one changes the intermediate dielectric media and interlayer distance, the ratio is a practically constant, being 2.01, independent of the layer configuration.

In Fig. 5.2, we show the probability density of the intralayer and interlayer exciton state. The intralayer state is more compact with respect to the interlayer one, which is not surprising, as the reduced masses are such that $\mu_y/\mu_x = 16.4$ (see table 5.1), which tends to squeeze the state along y -axis with respect to the x -axis. Furthermore, the interlayer exciton probability density distribution is more extended owing to the smaller binding

	Intralayer	Interlayer
R_x	8.701 Å	10.870 Å
R_y	4.324 Å	5.401 Å
$\frac{R_x}{R_y}$	2.012	2.012

TABLE 5.3 – Direction Bohr radius, given in Eqs. (5.34). Here we consider an interlayer distance of $d = 10\text{Å}$, and dielectric media composed of $\epsilon_1 = \epsilon_m = \epsilon_3 = 1$. The interlayer, and intralayer potentials are given in Eqs. (1.21) (1.22)

with respect to the interlayer one (cf. Fig. 5.1).

5.4 Conclusion

In this chapter, we have developed a generic momentum space formalism to deal with two particles with constant anisotropic mass distributions. As we could see in the preceding discussion, we were able to derive an integral equation for the description of the exciton, leading to well convergent calculation. We explored a number of different configurations of the aligned double layer of black phosphorous by changing the interlayer dielectric, as well as the separation distance and study the response of the exciton binding energy. Some general features found in the exciton binding in the phosphorene bilayer qualitatively follows the findings obtained for the double layer dichalcogenides heterostructure studied in Chapter 4, with separation and interlayer dielectric constant. The asymmetry in the exciton probability density is kept for both interlayer and intralayer cases and the ratio of the radii along the x and y axis is $R_x/R_y = 2.01$ practically independent on the interlayer dielectric and separation distance and determined by the imbalance of the reduced masses $\mu_y/\mu_x = 16.4$ in the y and x directions.

6 Conclusion and Perspectives

6.1 A Short Summary

In this dissertation we have presented the interplay between many-body and few-body systems through an analysis of the electron gas in a two-band approximation, and focus of the exciton properties on double layers of semiconductor heterostructures of dicalchogenides and black phosphorous. We have prepared, in Chapter 2, the formalism for the Semiconductor Bloch equations equations in order to probe the important linear response to light of the systems to be used in future applications. We have also discussed physically the dynamical content of each term entering in these time-dependent equations. Then, in Chapter 3 we have developed the tools to solve numerically the central equation for the excitons, namely the Wannier equation. These numerical tools were described details in the chapter, namely, the quadrature scheme using Gauss-Legendre points, the Chebyshev Chawla-Kumar method, and a variational approach based on the Generating Coordinate Method, which was briefly discussed.

In Chapter 4, we have shown how the configuration of a bilayer heterostructure, that is, two distinct layers stacked on top of each other, built in a dielectric environment, renormalizes the band gap and affects the wave function and binding energy of the system in question. Also, we have introduced a fitting procedure to capture parameters by self-consistently solving for bare band gap and calculate the exchange self-energy correction, with this procedure, allied with the an analysis of the band alignment of MoS_2 - WTe_2 , we have proposed a possible candidate for a excitonically driven insulating state, in which the binding energy of the exciton is larger than the gap.

In Chapter 5, we have presented a solution to the Wannier exciton equation in the case of the phosphorene homobilayer by introducing a change of coordinates in momentum space to account for the rotational anisotropy in the dispersion relation of the charge carriers. We have explored the effects of variation of the interlayer dielectric and separation in the binding and structure of the intra- and interlayer excitons, exposing the anisotropy of the exciton probability density and aspect ratio.

6.2 Future Perspectives

We intend to develop a scheme to treat Moiré systems with anisotropy, considering a relative rotation between the layers, which due to the non-separability of the relative and center of mass coordinates may lead to the appearance of possible confining modes of excitons or trions, even for non-interacting particles. Following the study done in Chapter 5, we intend to solve the Moiré problem considering all coordinates, namely the relative and center of mass ones, which should lead, due to the mixing of these coordinates to coupled integral equations. Then, we will start to investigate trions and higher correlations in the phosphorene and TMDCs. As we add more particles to the few-body correlations, the computational challenge increases. One approach is to consider separable potentials. The construction of such potentials is a fundamental step so we can have a cost effective method in order to explore each possibility with respect to the materials and carrier arrangements. For the trion problem in anisotropic materials, some preliminary work in the analytical form of the kinetic energy operator has been made, such as deriving the effective Hamiltonian for three-body problem (an interested reader can read the Appendix A). On the many-body theory front, we plan to investigate the effects of trions in optical properties deriving a similar scheme to the Semiconductor Bloch equations but for a trion polarization operator.

The derivation of the effective Hamiltonian for the trion in the phosphorene is rather similar the exciton case, in particular, a good physical image is an interaction of an exciton with a electron. We hope to treat this problem using two distinct approaches. First, we will apply the Gaussian Expansion Method (KAMIMURA, 1988; HIYAMA, 2012) in real space. Then, we will study using the Faddeev equations, similarly to the reference (MOHSENI *et al.*, 2023). With this final construction, we end the current work with our future challenges. We wish also to study higher correlations like the biexcitons and understand its effects on many properties of 2D materials.

Our main future direction is to establish a bridge between two seemingly distant areas, namely condensed matter problems with its intrinsically many-body nature and few-body correlations, making use of the different numerical approaches to the problems mentioned in this dissertation. In retrospect, theoretical tools should not lie in boxes placed in distant shelves and efforts have to be done in building connections between disciplines, as well as also reinforcing cooperation. Scientific advance is necessarily a worldwide enterprise and profit from crossing the borders of different fields to push the knowledge even further.

Bibliography

ADHIKARI, S. K. Quantum scattering in two dimensions. **American Journal of Physics**, v. 54, p. 362–367, 1986.

AKHTAR, M.; ANDERSON, G.; ZHAO, R.; ALRUQI, A.; MROCZKOWSKA, J. E.; SUMANASEKERA, G.; JASINSKI, J. B. Recent advances in synthesis, properties, and applications of phosphorene. **npj 2D Materials and Applications**, v. 1, n. 1, p. 5, Apr 2017. ISSN 2397-7132. Available at: <https://doi.org/10.1038/s41699-017-0007-5>.

ANDERSON, P. W. More is different. **Science**, American Association for the Advancement of Science, v. 177, n. 4047, p. 393–396, Aug 1972. Available at: <https://doi.org/10.1126/science.177.4047.393>.

ASLAN, B.; YULE, C.; YU, Y.; LEE, Y. J.; HEINZ, T. F.; CAO, L.; BRONGERSMA, M. L. Excitons in strained and suspended monolayer wse₂. **2D Materials**, IOP Publishing, v. 9, n. 1, p. 015002, oct 2021. Available at: <https://dx.doi.org/10.1088/2053-1583/ac2d15>.

BERKELBACH, T. C.; HYBERTSEN, M. S.; REICHMAN, D. R. Theory of neutral and charged excitons in monolayer transition metal dichalcogenides. **Physical Review B**, APS, v. 88, n. 4, p. 045318, 2013.

BLOCH, F. Über die quantenmechanik der elektronen in kristallgittern. **Zeitschrift für Physik**, v. 52, n. 7, p. 555–600, Jul 1929. ISSN 0044-3328. Available at: <https://doi.org/10.1007/BF01339455>.

BOK, J. M.; HWANG, J.; CHOI, H.-Y. Excitonic insulator emerging from semiconducting normal state in $1t$ -tise₂. **Phys. Rev. B**, American Physical Society, v. 103, p. 205108, May 2021. Available at: <https://link.aps.org/doi/10.1103/PhysRevB.103.205108>.

CHAVES, A.; AZADANI, J.; ALSALMAN, H.; COSTA, D. R. da; FRISENDA, R.; CHAVES, A.; SONG, S. H.; KIM, Y.; HE, D.; ZHOU, J. *et al.* Bandgap engineering of two-dimensional semiconductor materials. **npj 2D Materials and Applications**, Nature Publishing Group, v. 4, n. 1, p. 1–21, 2020.

CHAVES, A.; JI, W.; MAASSEN, J.; DUMITRICĂ, T.; LOW, T. Theoretical overview of black phosphorus. *In*: _____. Cambridge: Cambridge University Press, 2017. p. 381–412. (2D Materials: Properties and Devices). ISBN 9781107163713. Available at: <https://www.cambridge.org/core/books/2d-materials/theoretical-overview-of-black-phosphorus/7EF6C5C667B2450B31407A0C49940F8D>.

- CHAVES, A.; SOUSA, G. O.; KHALIJI, K.; COSTA, D. R. da; FARIAS, G. A.; LOW, T. Signatures of subband excitons in few-layer black phosphorus. **Physical Review B**, APS, v. 103, n. 16, p. 165428, 2021.
- CHAVES, A. J.; RIBEIRO, R. M.; FREDERICO, T.; PERES, N. M. R. Excitonic effects in the optical properties of 2d materials: an equation of motion approach. **2D Materials**, IOP Publishing, v. 4, n. 2, p. 025086, apr 2017. Available at: <https://doi.org/10.1088/2053-1583/aa6b72>.
- CHOI, C.; HUANG, J.; CHENG, H.-C.; KIM, H.; VINOD, A. K.; BAE, S.-H.; ÖZÇELİK, V. O.; GRASSI, R.; CHAE, J.; HUANG, S.-W.; DUAN, X.; KAASBJERG, K.; LOW, T.; WONG, C. W. Enhanced interlayer neutral excitons and trions in trilayer van der waals heterostructures. **npj 2D Materials and Applications**, v. 2, n. 1, p. 30, Sep 2018. ISSN 2397-7132. Available at: <https://doi.org/10.1038/s41699-018-0075-1>.
- COMBESCOT, M.; BETBEDER-MATIBET, O.; DUBIN, F. The many-body physics of composite bosons. **Physics Reports**, v. 463, n. 5, p. 215–320, Jul 2008. ISSN 0370-1573. Available at: <https://www.sciencedirect.com/science/article/pii/S0370157308000975>.
- COMBESCOT, M.; SHIAU, S.-Y. **Excitons and Cooper Pairs: Two Composite Bosons in Many-Body Physics**. Oxford University Press, Dec 2015. Available at: <https://doi.org/10.1093/acprof:oso/9780198753735.001.0001>.
- COURANT, R.; HILBERT, D. **Methods of mathematical physics**. Nashville, TN: John Wiley & Sons, 1989. (Wiley Classics Library).
- DHANABALAN, S. C.; DHANABALAN, B.; PONRAJ, J. S.; BAO, Q.; ZHANG, H. 2d-materials-based quantum dots: Gateway towards next-generation optical devices. **Advanced Optical Materials**, John Wiley & Sons, Ltd, v. 5, n. 19, p. 1700257, Oct 2017. ISSN 2195-1071. Available at: <https://doi.org/10.1002/adom.201700257>.
- GEIM, A. K.; GRIGORIEVA, I. V. Van der waals heterostructures. **Nature**, Nature Publishing Group, v. 499, n. 7459, p. 419–425, 2013.
- GEIM, A. K.; NOVOSELOV, K. S. The rise of graphene. **"Nature Mat."**, Nature Publishing Group, v. 6, p. 183, 2007. Available at: <http://dx.doi.org/10.1038/nmat1849><http://dx.doi.org/10.1038/nmat1849>.
- GOLBERG, M. A. **Numerical solution of integral equations**. [S.l.]: Springer Science & Business Media, 2013.
- GRIFFIN, J. J.; WHEELER, J. A. Collective motions in nuclei by the method of generator coordinates. **Phys. Rev.**, American Physical Society, v. 108, p. 311–327, Oct 1957. Available at: <https://link.aps.org/doi/10.1103/PhysRev.108.311>.
- HARATS, M. G.; KIRCHHOF, J. N.; QIAO, M.; GREBEN, K.; BOLOTIN, K. I. Dynamics and efficient conversion of excitons to trions in non-uniformly strained monolayer ws2. **Nature Photonics**, v. 14, n. 5, p. 324–329, May 2020. Available at: <https://doi.org/10.1038/s41566-019-0581-5>.
- HAUG, H.; KOCH, S. W. **Quantum Theory of the Optical and Electronic Properties of Semiconductors**. WORLD SCIENTIFIC, 2004. 468 p. ISBN 978-981-238-609-0. Available at: <https://doi.org/10.1142/5394>.

HAVE, J.; CATARINA, G.; PEDERSEN, T. G.; PERES, N. M. R. Monolayer transition metal dichalcogenides in strong magnetic fields: Validating the wannier model using a microscopic calculation. **Phys. Rev. B**, American Physical Society, v. 99, p. 035416, Jan 2019. Available at: <https://link.aps.org/doi/10.1103/PhysRevB.99.035416>.

HE, K.; KUMAR, N.; ZHAO, L.; WANG, Z.; MAK, K. F.; ZHAO, H.; SHAN, J. Tightly bound excitons in monolayer wse 2. **Physical review letters**, APS, v. 113, n. 2, p. 026803, 2014.

HIYAMA, E. Gaussian expansion method for few-body systems and its applications to atomic and nuclear physics. **Progress of Theoretical and Experimental Physics**, v. 2012, n. 1, p. 01A204, Jan 2012. ISSN 2050-3911. Available at: <https://doi.org/10.1093/ptep/pts015>.

HOHENBERG, P.; KOHN, W. Inhomogeneous electron gas. **Phys. Rev.**, American Physical Society, v. 136, p. B864–B871, Nov 1964. Available at: <https://link.aps.org/doi/10.1103/PhysRev.136.B864>.

JÉROME, D.; RICE, T. M.; KOHN, W. Excitonic insulator. **Phys. Rev.**, American Physical Society, v. 158, p. 462–475, Jun 1967. Available at: <https://link.aps.org/doi/10.1103/PhysRev.158.462>.

JIA, Y.; WANG, P.; CHIU, C.-L.; SONG, Z.; YU, G.; JÄCK, B.; LEI, S.; KLEMENZ, S.; CEVALLOS, F. A.; ONYSZCZAK, M.; FISHCHENKO, N.; LIU, X.; FARAHI, G.; XIE, F.; XU, Y.; WATANABE, K.; TANIGUCHI, T.; BERNEVIG, B. A.; CAVA, R. J.; SCHOOP, L. M.; YAZDANI, A.; WU, S. Evidence for a monolayer excitonic insulator. **Nature Physics**, v. 18, n. 1, p. 87–93, Jan 2022. ISSN 1745-2481. Available at: <https://doi.org/10.1038/s41567-021-01422-w>.

JIANG, Z.; LIU, Z.; LI, Y.; DUAN, W. Scaling universality between band gap and exciton binding energy of two-dimensional semiconductors. **Phys. Rev. Lett.**, American Physical Society, v. 118, p. 266401, Jun 2017. Available at: <https://link.aps.org/doi/10.1103/PhysRevLett.118.266401>.

KAMIMURA, M. Nonadiabatic coupled-rearrangement-channel approach to muonic molecules. **Phys. Rev. A**, American Physical Society, v. 38, p. 621–624, Jul 1988. Available at: <https://link.aps.org/doi/10.1103/PhysRevA.38.621>.

Keldysh, L. V. Coulomb interaction in thin semiconductor and semimetal films. **Soviet Journal of Experimental and Theoretical Physics Letters**, v. 29, p. 658, jun. 1979.

KIM, S. All-2d material photonic devices. **Nanoscale Advances**, RSC, v. 5, n. 2, p. 323–328, 2023. Available at: <https://doi.org/10.1039/D2NA00732K>.

KIRA, M.; KOCH, S. W. Many-body correlations and excitonic effects in semiconductor spectroscopy. **Progress in Quantum Electronics**, v. 30, n. 5, p. 155–296, Jan 2006. ISSN 0079-6727. Available at: <https://www.sciencedirect.com/science/article/pii/S0079672706000280>.

KIRA, M.; KOCH, S. W. **Semiconductor Quantum Optics**. Cambridge: Cambridge University Press, 2011. ISBN 9780521875097. Available at: <https://www.cambridge.org/core/books/semiconductor-quantum-optics/51D98D5024669175874BAC9552FFF338>.

- KLOTS, A. R.; NEWAZ, A. K. M.; WANG, B.; PRASAI, D.; KRZYZANOWSKA, H.; LIN, J.; CAUDEL, D.; GHIMIRE, N. J.; YAN, J.; IVANOV, B. L.; VELIZHANIN, K. A.; BURGER, A.; MANDRUS, D. G.; TOLK, N. H.; PANTELIDES, S. T.; BOLOTIN, K. I. Probing excitonic states in suspended two-dimensional semiconductors by photocurrent spectroscopy. **Scientific Reports**, v. 4, n. 1, p. 6608, Oct 2014. ISSN 2045-2322. Available at: <https://doi.org/10.1038/srep06608>.
- KOHN, W. Excitonic phases. **Phys. Rev. Lett.**, American Physical Society, v. 19, p. 439–442, Aug 1967. Available at: <https://link.aps.org/doi/10.1103/PhysRevLett.19.439>.
- KOHN, W.; SHAM, L. J. Self-consistent equations including exchange and correlation effects. **Phys. Rev.**, American Physical Society, v. 140, p. A1133–A1138, Nov 1965. Available at: <https://link.aps.org/doi/10.1103/PhysRev.140.A1133>.
- KOKSAL, O.; JUNG, M.; MANOLATOU, C.; VAMIVAKAS, A. N.; SHVETS, G.; RANA, F. Structure and dispersion of exciton-trion-polaritons in two-dimensional materials: Experiments and theory. **Phys. Rev. Res.**, American Physical Society, v. 3, p. 033064, Jul 2021. Available at: <https://link.aps.org/doi/10.1103/PhysRevResearch.3.033064>.
- KORMÁNYOS, A.; BURKARD, G.; GMITRA, M.; FABIAN, J.; ZÓLYOMI, V.; DRUMMOND, N. D.; FAL'KO, V. K · p theory for two-dimensional transition metal dichalcogenide semiconductors. **2d Mater.**, IOP Publishing, v. 2, n. 2, p. 022001, abr. 2015.
- KORMÁNYOS, A.; BURKARD, G.; GMITRA, M.; FABIAN, J.; ZÓLYOMI, V.; DRUMMOND, N. D.; FAL'KO, V. k · p theory for two-dimensional transition metal dichalcogenide semiconductors. **2D Materials**, IOP Publishing, v. 2, n. 2, p. 022001, apr 2015. Available at: <https://doi.org/10.1088/2053-1583/2/2/022001>.
- KORMÁNYOS, A.; ZÓLYOMI, V.; DRUMMOND, N. D.; RAKYTA, P.; BURKARD, G.; FAL'KO, V. I. Monolayer mos₂: Trigonal warping, the Γ valley, and spin-orbit coupling effects. **Phys. Rev. B**, American Physical Society, v. 88, p. 045416, Jul 2013. Available at: <https://link.aps.org/doi/10.1103/PhysRevB.88.045416>.
- KORMÁNYOS, A.; ZÓLYOMI, V.; DRUMMOND, N. D.; BURKARD, G. Spin-orbit coupling, quantum dots, and qubits in monolayer transition metal dichalcogenides. **Phys. Rev. X**, American Physical Society, v. 4, p. 011034, Mar 2014. Available at: <https://link.aps.org/doi/10.1103/PhysRevX.4.011034>.
- KYLÄNPÄÄ, I.; KOMSA, H.-P. Binding energies of exciton complexes in transition metal dichalcogenide monolayers and effect of dielectric environment. **Physical Review B**, APS, v. 92, n. 20, p. 205418, 2015.
- KYLÄNPÄÄ, I.; KOMSA, H.-P. Binding energies of exciton complexes in transition metal dichalcogenide monolayers and effect of dielectric environment. **Phys. Rev. B**, American Physical Society, v. 92, p. 205418, Nov 2015. Available at: <https://link.aps.org/doi/10.1103/PhysRevB.92.205418>.
- LAMOUNTAIN, T.; LENFERINK, E. J.; CHEN, Y.-J.; STANEV, T. K.; STERN, N. P. Environmental engineering of transition metal dichalcogenide optoelectronics. **Frontiers of Physics**, Springer, v. 13, n. 4, p. 1–32, 2018.

LATINI, S.; WINTHER, K. T.; OLSEN, T.; THYGESEN, K. S. Interlayer excitons and band alignment in mos₂/hbn/wse₂ van der waals heterostructures. **Nano letters**, ACS Publications, v. 17, n. 2, p. 938–945, 2017.

LI, M.-Y.; CHEN, C.-H.; SHI, Y.; LI, L.-J. Heterostructures based on two-dimensional layered materials and their potential applications. **Materials Today**, Elsevier, v. 19, n. 6, p. 322–335, 2016.

LI, Y.; CHERNIKOV, A.; ZHANG, X.; RIGOSI, A.; HILL, H. M.; ZANDE, A. M. van der; CHENET, D. A.; SHIH, E.-M.; HONE, J.; HEINZ, T. F. Measurement of the optical dielectric function of monolayer transition-metal dichalcogenides: mos₂, MoSe₂, ws₂, and WSe₂. **Phys. Rev. B**, American Physical Society, v. 90, p. 205422, Nov 2014. Available at: <https://link.aps.org/doi/10.1103/PhysRevB.90.205422>.

LIU, G.-B.; XIAO, D.; YAO, Y.; XU, X.; YAO, W. Electronic structures and theoretical modelling of two-dimensional group-vib transition metal dichalcogenides. **Chemical Society Reviews**, Royal Society of Chemistry, v. 44, n. 9, p. 2643–2663, 2015.

MAK, K. F.; HE, K.; LEE, C.; LEE, G. H.; HONE, J.; HEINZ, T. F.; SHAN, J. Tightly bound trions in monolayer mos₂. **Nature Materials**, v. 12, n. 3, p. 207–211, Mar 2013. ISSN 1476-4660. Available at: <https://doi.org/10.1038/nmat3505>.

MAK, K. F.; LEE, C.; HONE, J.; SHAN, J.; HEINZ, T. F. Atomically thin mos 2: a new direct-gap semiconductor. **Physical review letters**, APS, v. 105, n. 13, p. 136805, 2010.

MAK, K. F.; SHAN, J. Photonics and Optoelectronics of 2D Semiconductor Transition Metal Dichalcogenides. **NatPhoto**, Springer Nature, v. 10, n. 4, p. 216–226, apr 2016. Available at: <https://doi.org/10.1038/nphoton.2015.282>.

MASUJIMA, M. **Applied mathematical methods in theoretical physics**. 2. ed. Weinheim, Germany: Wiley-VCH Verlag, 2009.

MATSUDA, K. Optical properties of atomically thin layered transition metal dichalcogenide. **Journal of the Physical Society of Japan**, Physical Society of Japan, v. 84, n. 12, p. 121009, dez. 2015. Available at: <https://doi.org/10.7566/jpsj.84.121009>.

MATTHEISS, L. F. Band structures of transition-metal-dichalcogenide layer compounds. **Phys. Rev. B**, American Physical Society, v. 8, p. 3719–3740, Oct 1973. Available at: <https://link.aps.org/doi/10.1103/PhysRevB.8.3719>.

MOHSENI, K.; HADIZADEH, M. R.; FREDERICO, T.; COSTA, D. R. da; CHAVES, A. J. Trion clustering structure and binding energy in two-dimensional semiconductor materials: Faddeev equations approach. **Phys. Rev. B**, American Physical Society, v. 107, p. 165427, Apr 2023. Available at: <https://link.aps.org/doi/10.1103/PhysRevB.107.165427>.

MOLAS, M. R.; MACEWICZ, Ł.; WIELOSZYŃSKA, A.; JAKÓBCZYK, P.; WYSMOLEK, A.; BOGDANOWICZ, R.; JASINSKI, J. B. Photoluminescence as a probe of phosphorene properties. **npj 2D Materials and Applications**, v. 5, n. 1, p. 83, Sep 2021. ISSN 2397-7132. Available at: <https://doi.org/10.1038/s41699-021-00263-8>.

NOVOSELOV, K. S.; GEIM, A. K.; MOROZOV, S. V.; JIANG, D.; ZHANG, Y.; DUBONOS, S. V.; GRIGORIEVA, I. V.; FIRSOV, A. A. Electric field effect in atomically thin carbon films. **Science**, American Association for the Advancement of Science, v. 306, n. 5696, p. 666–669, 2004. ISSN 0036-8075.

NOVOSELOV, K. S.; MISHCHENKO, A.; CARVALHO, A.; NETO, A. H. C. 2d materials and van der waals heterostructures. **Science**, American Association for the Advancement of Science, v. 353, n. 6298, p. aac9439, Jul 2016. Available at: <https://doi.org/10.1126/science.aac9439>.

PEDERSEN, T. G. Exciton stark shift and electroabsorption in monolayer transition-metal dichalcogenides. **Phys. Rev. B**, American Physical Society, v. 94, p. 125424, Sep 2016. Available at: <https://link.aps.org/doi/10.1103/PhysRevB.94.125424>.

PIZA, A. F. R. de T.; PASSOS, E. J. V. de; GALETTI, D.; NEMES, M. C.; WATANABE, M. M. Properties of griffin-hill-wheeler spaces. **Phys. Rev. C**, American Physical Society, v. 15, p. 1477–1482, Apr 1977. Available at: <https://link.aps.org/doi/10.1103/PhysRevC.15.1477>.

PLANCK, M.; MASIUS, M. **The Theory of Heat Radiation**. [*S.l.*]: Blakiston, 1914.

QUINTELA, M. F. C. M.; HENRIQUES, J. C. G.; TENÓRIO, L. G. M.; PERES, N. M. R. Theoretical methods for excitonic physics in 2d materials. **Physica Status Solidi (B)**, Wiley, v. 259, n. 7, p. 2200097, abr. 2022. Available at: <https://doi.org/10.1002/pssb.202200097>.

QUINTELA, M. F. M.; PERES, N. M. A colloquium on the variational method applied to excitons in 2d materials. **The European Physical Journal B**, v. 93, n. 12, 2020.

RODIN, A. S.; CARVALHO, A.; NETO, A. H. C. Excitons in anisotropic two-dimensional semiconducting crystals. **Phys. Rev. B**, American Physical Society, v. 90, p. 075429, Aug 2014. Available at: <https://link.aps.org/doi/10.1103/PhysRevB.90.075429>.

RÖSSLER, U. **Solid State Theory**. Springer Berlin Heidelberg, 2009. Available at: <https://doi.org/10.1007/978-3-540-92762-4>.

ROSSNAGEL, K.; KIPP, L.; SKIBOWSKI, M. Charge-density-wave phase transition in $1t - t_{2g}$: excitonic insulator versus band-type jahn-teller mechanism. **Phys. Rev. B**, American Physical Society, v. 65, p. 235101, May 2002. Available at: <https://link.aps.org/doi/10.1103/PhysRevB.65.235101>.

RYTOVA, N. S. Coulomb interaction of electrons in a thin film. v. 163, n. 5, p. 1118–1120, 1965.

RYTOVA, N. S. The screened potential of a point charge in a thin film. **Moscow University Physics Bulletin**, v. 3, n. 3, p. 18, 1967.

SHANKAR, R. **Effective Field Theory in Condensed Matter Physics**. 1997.

STOER, J.; BULIRSCH, R. **Introduction to Numerical Analysis**. Springer New York, 1980. Available at: <https://doi.org/10.1007/978-1-4757-5592-3>.

TENÓRIO, L. G. M.; PEREIRA, T. A. S.; MOHSENI, K.; FREDERICO, T.; HADIZADEH, M. R.; COSTA, D. R. da; CHAVES, A. J. **Tunable properties of excitons in double monolayer semiconductor heterostructures**. 2023.

TUAN, D. V.; SHI, S.-F.; XU, X.; CROOKER, S. A.; DERY, H. Six-body and eight-body exciton states in monolayer wse_2 . **Phys. Rev. Lett.**, American Physical Society, v. 129, p. 076801, Aug 2022. Available at: <https://link.aps.org/doi/10.1103/PhysRevLett.129.076801>.

UGEDA, M. M.; BRADLEY, A. J.; SHI, S.-F.; FELIPE, H.; ZHANG, Y.; QIU, D. Y.; RUAN, W.; MO, S.-K.; HUSSAIN, Z.; SHEN, Z.-X. *et al.* Giant bandgap renormalization and excitonic effects in a monolayer transition metal dichalcogenide semiconductor. **Nature materials**, Nature Publishing Group, v. 13, n. 12, p. 1091–1095, 2014.

WANG, Z.; ZHAO, L.; MAK, K. F.; SHAN, J. Probing the Spin-Polarized Electronic Band Structure in Monolayer Transition Metal Dichalcogenides by Optical Spectroscopy. **NanoLett**, American Chemical Society (ACS), v. 17, n. 2, p. 740–746, Jan 2017. Available at: <https://doi.org/10.1021/acs.nanolett.6b03855>.

WHITTOCK, A. L.; ABIOLA, T. T.; STAVROS, V. G. A perspective on femtosecond pump–probe spectroscopy in the development of future sunscreens. **The Journal of Physical Chemistry A**, American Chemical Society, v. 126, n. 15, p. 2299–2308, Apr 2022. ISSN 1089-5639. Available at: <https://doi.org/10.1021/acs.jpca.2c01000>.

WONG, C. W. Generator-coordinate theory as a flexible formulation of the many-body schrodinger equation. **Nucl. Phys. A147: 545-62(1970)**, 1 1970. Available at: <https://www.osti.gov/biblio/4102402>.

XIAO, D.; LIU, G.-B.; FENG, W.; XU, X.; YAO, W. Coupled spin and valley physics in monolayers of mos_2 and other group-vi dichalcogenides. **Phys. Rev. Lett.**, American Physical Society, v. 108, p. 196802, May 2012. Available at: <https://link.aps.org/doi/10.1103/PhysRevLett.108.196802>.

XIE, H.; JIANG, S.; RHODES, D. A.; HONE, J. C.; SHAN, J.; MAK, K. F. Tunable exciton-optomechanical coupling in suspended monolayer mose_2 . **Nano Letters**, American Chemical Society, v. 21, n. 6, p. 2538–2543, Mar 2021. ISSN 1530-6984. Available at: <https://doi.org/10.1021/acs.nanolett.0c05089>.

YE, Z.; CAO, T.; O'BRIEN, K.; ZHU, H.; YIN, X.; WANG, Y.; LOUIE, S. G.; ZHANG, X. Probing excitonic dark states in single-layer tungsten disulphide. **Nature**, Nature Publishing Group, v. 513, n. 7517, p. 214–218, 2014.

YOU, Y.; ZHANG, X.-X.; BERKELBACH, T. C.; HYBERTSEN, M. S.; REICHMAN, D. R.; HEINZ, T. F. Observation of biexcitons in monolayer wse_2 . **Nature Physics**, v. 11, n. 6, p. 477–481, Jun 2015. ISSN 1745-2481. Available at: <https://doi.org/10.1038/nphys3324>.

YU, P. Y.; CARDONA, M. **Fundamentals of Semiconductors**. Springer Berlin Heidelberg, 2010. Available at: <https://doi.org/10.1007/978-3-642-00710-1>.

ZHANG, C.; GONG, C.; NIE, Y.; MIN, K.-A.; LIANG, C.; OH, Y. J.; ZHANG, H.; WANG, W.; HONG, S.; COLOMBO, L.; WALLACE, R. M.; CHO, K. Systematic study of electronic structure and band alignment of monolayer transition metal dichalcogenides in van der waals heterostructures. **2D Materials**, IOP Publishing, v. 4, n. 1, p. 015026, nov 2016. Available at: <https://doi.org/10.1088/2053-1583/4/1/015026>.

ZHANG, C.; JOHNSON, A.; HSU, C.-L.; LI, L.-J.; SHIH, C.-K. Direct imaging of band profile in single layer mos2 on graphite: quasiparticle energy gap, metallic edge states, and edge band bending. **Nano letters**, ACS Publications, v. 14, n. 5, p. 2443–2447, 2014.

Appendix A - Three-Body Hamiltonian for the phosphorene

We present, in what follows, the derivation of the kinetic part of the three-body Hamiltonian that is the key construction to study the trion in anisotropic systems, such as the phosphorene. Let \vec{r}_e , \vec{r}_h and $\vec{r}_{e'}$ be the position of the electron, hole and the second electron. We choose to work in the center of mass system, and the relevant coordinates are the relative e - h distances and the relative coordinate of the e' with respect to the center of mass of the e - h pair.

Now, let us write down the coordinates of the center of mass,

$$\bar{x} = \frac{m_e^x x_e + m_e^x x_{e'} + m_h^x x_h}{\bar{M}^x} \quad (\text{A.1})$$

$$\bar{y} = \frac{m_e^y y_e + m_e^y y_{e'} + m_h^y y_h}{\bar{M}^y} \quad (\text{A.2})$$

$$x_{rel} = x_e - x_h \quad (\text{A.3})$$

$$y_{rel} = y_e - y_h \quad (\text{A.4})$$

$$x' = x_{e'} - \frac{m_e^x x_e + m_h^x x_h}{M^x} \quad (\text{A.5})$$

$$y' = y_{e'} - \frac{m_e^y y_e + m_h^y y_h}{M^y} \quad (\text{A.6})$$

where $\bar{M}^i = 2m_e^i + m_h^i$ and $M^i = m_e^i + m_h^i$. The procedure is analogous but more laborious. In short, we note that, for each coordinate ξ for the particle i ,

$$\frac{\partial}{\partial \xi_i} = \frac{\partial \bar{\xi}}{\partial \xi_i} \frac{\partial}{\partial \bar{\xi}} + \frac{\partial \xi_{rel}}{\partial \xi_i} \frac{\partial}{\partial \xi_{rel}} + \frac{\partial \xi'}{\partial \xi_i} \frac{\partial}{\partial \xi'} \quad (\text{A.7})$$

$$\frac{\partial^2}{\partial \xi_i^2} = \left(\frac{\partial \bar{\xi}}{\partial \xi_i} \frac{\partial}{\partial \bar{\xi}} + \frac{\partial \xi_{rel}}{\partial \xi_i} \frac{\partial}{\partial \xi_{rel}} + \frac{\partial \xi'}{\partial \xi_i} \frac{\partial}{\partial \xi'} \right) \left(\frac{\partial \bar{\xi}}{\partial \xi_i} \frac{\partial}{\partial \bar{\xi}} + \frac{\partial \xi_{rel}}{\partial \xi_i} \frac{\partial}{\partial \xi_{rel}} + \frac{\partial \xi'}{\partial \xi_i} \frac{\partial}{\partial \xi'} \right) = \quad (\text{A.8})$$

$$= \left(\frac{\partial \bar{\xi}}{\partial \xi_i} \right)^2 \frac{\partial^2}{\partial \bar{\xi}^2} + \left(\frac{\partial \xi_{rel}}{\partial \xi_i} \right)^2 \frac{\partial^2}{\partial \xi_{rel}^2} + \left(\frac{\partial \xi'}{\partial \xi_i} \right)^2 \frac{\partial^2}{\partial \xi'^2} + 2 \frac{\partial \bar{\xi}}{\partial \xi_i} \frac{\partial \xi_{rel}}{\partial \xi_i} \frac{\partial^2}{\partial \bar{\xi} \partial \xi_{rel}} +$$

$$+ 2 \frac{\partial \xi_{rel}}{\partial \xi_i} \frac{\partial \xi'}{\partial \xi_i} \frac{\partial^2}{\partial \xi_{rel} \partial \xi'} + 2 \frac{\partial \bar{\xi}}{\partial \xi_i} \frac{\partial \xi'}{\partial \xi_i} \frac{\partial^2}{\partial \bar{\xi} \partial \xi'} \quad (\text{A.9})$$

using this expression we can work out all the components of the kinetic energy,

$$\begin{aligned}
\frac{\partial^2}{\partial x_e^2} &= \left(\frac{m_e^x}{\bar{M}^x}\right)^2 \frac{\partial^2}{\partial \bar{x}} + \frac{\partial^2}{\partial x_{rel}^2} + \left(-\frac{m_e^x}{M^x}\right)^2 \frac{\partial^2}{\partial x'} + 2\frac{m_e^x}{\bar{M}^x} \frac{\partial^2}{\partial \bar{x} \partial x_{rel}} - 2\frac{m_e^x}{M^x} \frac{\partial^2}{\partial x_{rel} \partial x'} - 2\frac{(m_e^x)^2}{M^x \bar{M}^x} \frac{\partial^2}{\partial \bar{x} \partial x'} \\
\frac{\partial^2}{\partial y_e^2} &= \left(\frac{m_e^y}{\bar{M}^y}\right)^2 \frac{\partial^2}{\partial \bar{y}} + \frac{\partial^2}{\partial y_{rel}^2} + \left(-\frac{m_e^y}{M^y}\right)^2 \frac{\partial^2}{\partial y'} + 2\frac{m_e^y}{\bar{M}^y} \frac{\partial^2}{\partial \bar{y} \partial y_{rel}} - 2\frac{m_e^y}{M^y} \frac{\partial^2}{\partial y_{rel} \partial y'} - 2\frac{(m_e^y)^2}{M^y \bar{M}^y} \frac{\partial^2}{\partial \bar{y} \partial y'} \\
\frac{\partial^2}{\partial x_e'^2} &= \left(\frac{m_e^x}{\bar{M}^x}\right)^2 \frac{\partial^2}{\partial \bar{x}} + \frac{\partial^2}{\partial x'^2} + 2\frac{m_e^x}{\bar{M}^x} \frac{\partial^2}{\partial x' \partial \bar{x}} \\
\frac{\partial^2}{\partial y_e'^2} &= \left(\frac{m_e^y}{\bar{M}^y}\right)^2 \frac{\partial^2}{\partial \bar{y}} + \frac{\partial^2}{\partial y'^2} + 2\frac{m_e^y}{\bar{M}^y} \frac{\partial^2}{\partial y' \partial \bar{y}} \\
\frac{\partial^2}{\partial x_h^2} &= \left(\frac{m_h^x}{\bar{M}^x}\right)^2 \frac{\partial^2}{\partial \bar{x}} + \frac{\partial^2}{\partial x_{rel}^2} + \left(-\frac{m_h^x}{M^x}\right)^2 \frac{\partial^2}{\partial x'} - 2\frac{m_h^x}{\bar{M}^x} \frac{\partial^2}{\partial \bar{x} \partial x_{rel}} + 2\frac{m_h^x}{M^x} \frac{\partial^2}{\partial x_{rel} \partial x'} - 2\frac{(m_h^x)^2}{M^x \bar{M}^x} \frac{\partial^2}{\partial \bar{x} \partial x'} \\
\frac{\partial^2}{\partial y_h^2} &= \left(\frac{m_h^y}{\bar{M}^y}\right)^2 \frac{\partial^2}{\partial \bar{y}} + \frac{\partial^2}{\partial y_{rel}^2} + \left(-\frac{m_h^y}{M^y}\right)^2 \frac{\partial^2}{\partial y'} - 2\frac{m_h^y}{\bar{M}^y} \frac{\partial^2}{\partial \bar{y} \partial y_{rel}} + 2\frac{m_h^y}{M^y} \frac{\partial^2}{\partial y_{rel} \partial y'} - 2\frac{(m_h^y)^2}{M^y \bar{M}^y} \frac{\partial^2}{\partial \bar{y} \partial y'}
\end{aligned}$$

for now, I will make $\hbar = 1$. Now, lets group them up in directions. Starting with x ,

$$\begin{aligned}
-2T_x &= \frac{1}{m_e^x} \frac{\partial^2}{\partial x_e^2} + \frac{1}{m_h^x} \frac{\partial^2}{\partial x_h^2} + \frac{1}{m_e^x} \frac{\partial^2}{\partial x_e'^2} = \\
&= \frac{1}{\mu_x} \frac{\partial^2}{\partial x_{rel}^2} + \frac{1}{\bar{M}^x} \frac{\partial^2}{\partial \bar{x}^2} + \left(1 + \frac{1}{M^x}\right) \frac{\partial^2}{\partial x'}
\end{aligned} \tag{A.10}$$

for the y component,

$$\begin{aligned}
-2T_y &= \frac{1}{m_e^y} \frac{\partial^2}{\partial y_e^2} + \frac{1}{m_h^y} \frac{\partial^2}{\partial y_h^2} + \frac{1}{m_e^y} \frac{\partial^2}{\partial y_e'^2} = \\
&= \frac{1}{\mu_y} \frac{\partial^2}{\partial x_{rel}^2} + \frac{1}{\bar{M}^y} \frac{\partial^2}{\partial \bar{y}^2} + \left(1 + \frac{1}{M^y}\right) \frac{\partial^2}{\partial y'}.
\end{aligned} \tag{A.11}$$

Finally, the kinetic energy term in momentum space is,

$$H^0 = \frac{p_x^2}{2\mu_x} + \frac{\bar{P}_x^2}{2\bar{M}^x} + \left(1 + \frac{1}{M^x}\right) \frac{q_x^2}{2} + \frac{p_y^2}{2\mu_y} + \frac{\bar{P}_y^2}{2\bar{M}^y} + \left(1 + \frac{1}{M^y}\right) \frac{q_y^2}{2} \tag{A.12}$$

where,

$$\mu_i = \left(\frac{1}{m_e^i} + \frac{1}{m_h^i}\right) \tag{A.13}$$

$$\bar{M}^i = 2m_e^i + m_h^i \tag{A.14}$$

$$M^i = m_e^i + m_h^i. \tag{A.15}$$

FOLHA DE REGISTRO DO DOCUMENTO

1. CLASSIFICAÇÃO/TIPO DM	2. DATA 16 de agosto de 2023	3. DOCUMENTO Nº DCTA/ITA/DM-073/2023	4. Nº DE PÁGINAS 92
5. TÍTULO E SUBTÍTULO: Two-Body Correlations in Van der Waals Heterostructures			
6. AUTOR(ES): Luiz Gustavo Mendonça Tenório			
7. INSTITUIÇÃO(ÕES)/ÓRGÃO(S) INTERNO(S)/DIVISÃO(ÕES): Instituto Tecnológico de Aeronáutica – ITA			
8. PALAVRAS-CHAVE SUGERIDAS PELO AUTOR: Excitons; 2D Materials; Van der Waals Heterostructures			
9. PALAVRAS-CHAVE RESULTANTES DE INDEXAÇÃO: Problema de poucos corpos; Heteroestruturas de van der Waals; Estruturas bidimensionais; Física de partículas; Baixa temperatura; Física nuclear; Física.			
10. APRESENTAÇÃO: (X) Nacional () Internacional ITA, São José dos Campos. Curso de Mestrado. Programa de Pós-Graduação em Física. Área de Física Nuclear. Orientador: Prof. Dr. Tobias Frederico; coorientador: Prof. Dr. Teldo Anderson da Silva Pereira. Defesa em 28/07/2023. Publicada em 2023.			
11. RESUMO: A central paradigm of the many-body theory is that the underlying symmetries alongside the interactions that governs the many-particle system gives rise to emerging unique behavior. On the other side of the physical theory coverage, we have the few-body physics, where the number of interacting particles is low and universality lies in the independence of the very details regarding interactions. These two seemingly distant paths have already crossed in the context of ultracold gases and, more recently, also in condensed matter theory. In the case of condensed matter, the formation of composite structures by electrons and holes yields an interesting background to apply few-body techniques, even more so with the discovery of two dimensional materials and how their physical properties are tunable by environmental and geometric modifications. In this work we aim to study the physics of one composite structure, the exciton, in the context of 2D Van der Waals hetero and homostructures. Also, we will discuss about the rise of the excitonic insulators due to band alignment and strongly bound interlayer excitons in bilayer materials. Finally, we will discuss the excitonic physics of the Black Phosphorous, which has an anisotropic dispersion relation.			
12. GRAU DE SIGILO: <input checked="" type="checkbox"/> OSTENSIVO <input type="checkbox"/> RESERVADO <input type="checkbox"/> SECRETO			